Dark matter search with liquid argon in DarkSide: results with scientific and technological prototypes.

Bianca Bottino

Supervisor: **Prof. M. Pallavicini**
Prof. G. Fiorillo

Department of Physics
University of Genoa

This dissertation is submitted for the degree of
Doctor of Philosophy in Physics - XXXI PhD. cycle

University of Genoa March 2019

Un cuore coraggioso ed una lingua cortese
ti porteranno lontano nella giunga fratellino.

Il libro della giungla - R. Kipling

Che la nobiltà dell'Uomo, acquisita in cento secoli di prove e di errori, era consistita nel farsi signore della materia [...]. Che vincere la materia è comprenderla, e comprendere a materia è necessario per comprendere l'universo e noi stessi [...].

Il sistema periodico - P. Levi

Table of contents

List of figures

List of tables

Introduction

By observing our Universe we realize that we do not understand what we are seeing. An endless number of astrophysical evidences, accumulated since the 30s, puts us in front of the fact that something must be wrong, that we are not able to explain the data with our models of reality. Faced with these strong inconsistencies between how we think the Universe is and what we can see of this Universe, there are two possible explanations. Either we are making a mistake in thinking, which means that our models are wrong, or we are doing wrong looking at the Universe, which means that there is something that we can not see.

These are the two different approaches with which we faced, and still face today, the so-called *problem of dark matter* . The first fundamental question to ask ourselves is: *should we interpret the anomalies that we see as a refutation of the laws of gravitation or as an indication of the existence of unseen objects?* Today, after years of experimental efforts, the answer is that there is something we do not see, what we call dark matter. At this point the key questions become two more: *what is this dark matter and how do we reveal it?* This is one of the most important, as well as intriguing, problems of today's physics. Perhaps we could venture to say that it is the problem par excellence at this moment. Precisely because it is a crucial problem has been addressed from different points of view in the last century. Numerous and compelling evidences of the existence of non-luminous matter have been found at different scales, but always and only indirect effects, due to the gravitational interaction of this mass distributions.

For now we have not yet found the dark matter. Proofs of the existence of the most famous dark matter candidates are still absent and this causes a growing sense of crisis in the dark matter particle community. Probably we should open the horizon and look for dark matter everywhere, diversifying the experiments and trying to put the pieces together.

In this rich and stimulating panorama we find DarkSide, an articulated project aimed at dark matter direct research. During my graduate school I had the opportunity to work in DarkSide, taking care of very different aspects. I contributed to the data analysis of the DarkSide-50 detector, I worked on the simulations and tests for the DarkSide-20k future detector, but above all I dedicated myself to the ReD-Recoil Directionality R&D project. ReD has the aim to investigate the directionality sensitivity in liquid argon, in the energy range of interest for the dark matter search. The basic idea is to irradiate a small dual-phase argon TPC with neutrons produced at the Tandem accelerator at the Laboratori Nazionali del Sud, in Catania. The scattered neutrons are then tagged by a neutron spectrometer that allows to reconstruct the scattering angle with respect to the TPC dirft field direction.

In this thesis I try, in the first chapter, to summarize the state of the art in the research of dark matter, starting from the experimental evidences and describing the possible candidates and the best revelation techniques.

In this regard, in the second chapter, I dwell on the properties of liquid argon and how these can be exploited to use a dual-phase argon Time Projection Chamber (TPC) as a detector of dark matter.

The third chapter is entirely dedicated to the DarkSide project. I describe the different components of the DarkSide-50 detector, currently installed at the Laboratori Nazionali del Gran Sasso and their working principle. One section is devoted to present the latest results obtained with DarkSide-50. I also illustrate the project for the next-generation detector, which is DarkSide-20k, giving special attention to the announcements with respect to the present setup.

Then, in chapter 4, I analyze the ReD project focusing on the scientific motivation behind the study of directional sensitivity and how this can be performed in a liquid argon detector exploiting the columnar recombination phenomenon. I describe in detail the idea behind ReD and the design of the experiment, in particular I explain the geometry of the setup with respect to the physics requirements.

Chapter 5 contains an in-depth description of all the components of the ReD experiment. Although it is a small project, it is a complex apparatus with three types of different detectors and an articulated system of ancillary infrastructures. Having personally dealt with the design, assembly, testing and operating of almost all the parts that compose ReD, I give ample space to their description.

Finally, in the sixth chapter I present the ReD preliminary results. The first part of the chapter is dedicated to the characterization measurements on the TPC, still underway at present; the second part instead contains the results obtained during the three data-taking campaigns carried out at LNS during 2018.

Chapter 1

Dark matter

Nowadays it is widely accepted that there is some form of dark matter, which constitutes about 25% of the energy density of our Universe. Discovering the nature of this non-luminous matter is a crucial challenge in particle physics. In fact, although there are solid astrophysical and cosmological evidences of its existence at different scales, very little is known of dark matter. We know that dark matter is 5 times more abundant with respect to standard baryonic matter and also that has a key role in the comprehension of the evolution of the Universe after the Big Bang.

Over the last thirty years, due to the fact that dark matter existence is established, countless efforts have been made from a theoretical point of view, to find convincing models and from an experimental point of view, to reveal it but so far without success. Currently, the dark matter research field is trying to evolve: collaborations are trying to build more sensitive detectors and are also diversifying the approaches [5].

In this chapter I briefly describe the most significant evidences of the existence of dark matter: starting from Vera Rubin's observations made on a galactic scale, up to the cosmological tests related to the study of the anisotropies of the cosmic microwave background. In section 1.2 I present some of the possible dark matter candidates, focusing in particular on the Weakly Interactive Massive Particles, the so-called WIMPs. Section 1.3 summarizes the main features of the direct detection method and gives an overview of the present status of the experiments.

1.1 How do we know it exists?

In the last hundred years a great deal of experimental evidence has emerged that proves the existence of non-luminous matter, that can not emit or absorb electromagnetic waves. These

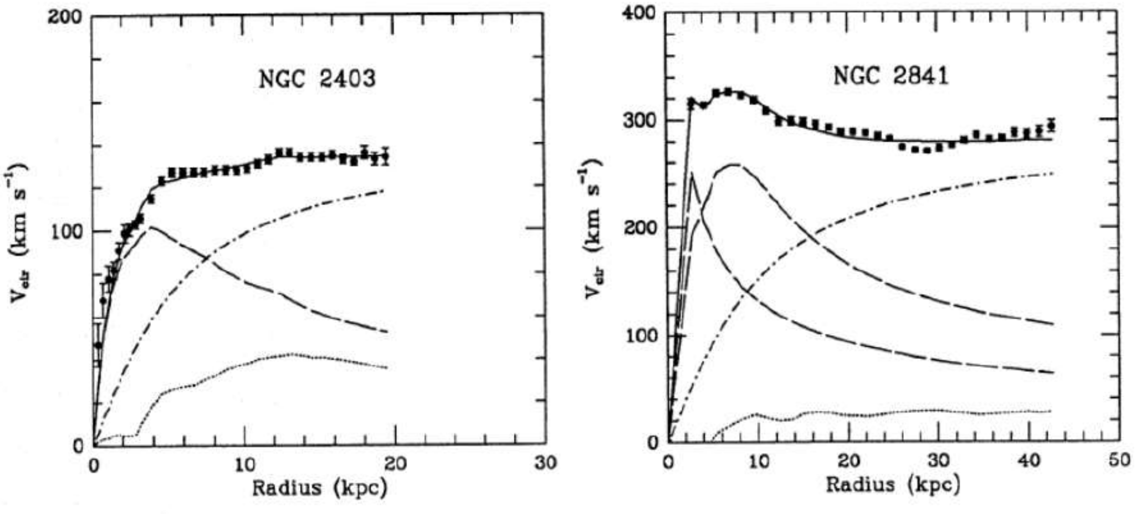

Fig. 1.1 Example of rotation curves for two sample galaxies: NGC 2403 and NGC 2841. The fit performed on the data takes into account the visible components (dashed line), the gas (dotted line), and the dark halo (dash-dotted line). It is evident that going further from the center of the galaxy the velocity becomes flat, contrary to what one would expect [1].

evidences, all of a gravitational nature, manifest themselves - as we shall see in this section - at all scales: galactic, inter-galactic and cosmological [16].

1.1.1 Stars rotation curves

On the galactic scale, the evidence of the existence of dark matter is given by the anomalous trend of the rotation curves of many spiral galaxies. The rotation curve of a galaxy is the graph of the rotation speed of the stars around the galactic center, as a function of their distance from it. Observing a spiral galaxy one can see that it typically consists of a dense central hub, surrounded by much lower density spiral arms extending outwards [17]. So, according to Newtonian dynamics, the circular velocity of stars should follow:

$$v(r) = \sqrt{\frac{GM(r)}{r}} \tag{1.1}$$

where $M(r) \equiv 4\pi \int \rho(r) r^2 dr$ is the mass included from the galactic center to the radius r and $\rho(r)$ is the mass density profile. This suggests that beyond the bulk of luminous matter, when $M(r)$ becomes approximatively constant, the velocity should decrease like $r^{-1/2}$.

On the contrary, already in the early 1970s, the astronomer Vera Rubin found that the observed rotation curves were almost flat at large r, *i.e.* most of the outer stars orbit with the same velocity [18]. The measurements of the redshift of the hydrogen spectral line - performed with a spectrograph - did not agree with the predictions. Even taking into account the mass in the arms of the galaxies to correct the speed of the outer stars, did not not eliminate the discrepancies. The possible options to explain the data were either to accept the failure of Newtonian gravity law, or to postulate the existence of a spherical non-luminous dark matter halo, with a mass density $\rho(r) \propto 1/r^2$.

A few years after the discovery of dark matter by Rubin, physicists such as Jeremiah Ostriker and James Peebles provided the theoretical framework to support her work and the mysterious substance settled into its celebrated place in science [19].

1.1.2 Galaxies clusters

From a chronological point of view the first clear indication of the existence of some form of non-luminous mass dates back to the thirties, when the Swiss astronomer Fritz Zwicky found a strong anomaly in the velocity dispersion of galaxies in the Coma cluster [20].

In particular, using the redshift he measured the velocity dispersion of eight galaxies and applied the Virial theorem to obtain an estimation of the mass of each of them. Then he found that the mean density of the cluster seemed to be 400 times greater than what was expected comparing the mass values with luminosity measurements [21]. Zwicky hypothesized that this large discrepancy could be due to a non-luminous mass and he referred to it with the term *"dunkle materie"*, literally *dark matter*.

Today it is possible to make a more accurate estimate of the M/L ratio, thanks to a better knowledge of the Hubble parameter at the present time, denoted as H_0. This parameter, that takes into account the expansion rate of the Universe nowadays, enters the calculation to determine the redshift following the Hubble law $z = H_0 d/c$ and was overestimated at the time of Zwicky's studies [22, 23]. Moreover, in the latest calculations the contribution due to the presence of intergalactic hot gas is subtracted from the missing mass, estimating it through a measurement of the X-ray emission [24]. Despite these corrections, a strong discrepancy of about two orders of magnitude remains and also shows up when the overall cluster mass is determined considering a cluster as a system in hydrostatic equilibrium [25].

1.1.3 Gravitational lensing

According to Einstein's theory of general relativity, a massive object changes the geometry of space-time around itself. This implies that light rays passing close to the body are affected by its gravitational field and are deflected, that is, they follow the geodesics in the curved space. The greater is the mass of the object, the stronger is the gravitational potential and

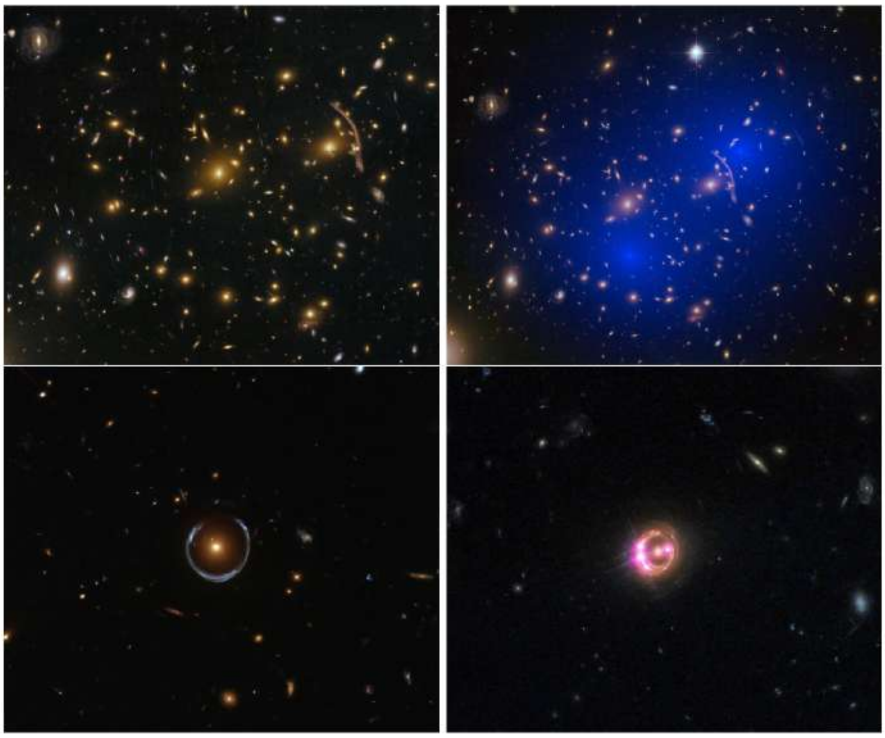

Fig. 1.2 Examples of strong gravitational lensing. The two top pictures show the Abell 370 cluster of galaxies. On the left there are giant arcs of the background objects, while on the right there is superimposed a blue halo that represents the DM distribution calculated with lensing. The bottom row shows a very neat Einstein ring on the left and a so-called Einstein cross - four multiple images of the same object - on the right obtained superimposing an optical picture with an image by the Chandra X-ray Observatory [2, 3].

consequently the more marked will be the deflection. This property of the space-time causes the light from distant astrophysical objects to be diverted when it passes close to the mass distributions of clusters or galaxies, because they actually bend the space nearby. As a consequence, the image of the object we see on Earth is distorted, amplified or multiplied. This effect is referred to as gravitational lensing and it is extremely useful for establishing the existence of dark matter [26].

Observing a far source and studying the distortions of its image due to gravity, allows to estimate the mass of the astrophysical objects in between. It is important to underline that the lensing effects depends on the total mass of a system, like a cluster, so it takes into account both luminous and dark matter. Indeed comparing the gravitational lensing results with optical observations indicates a missing mass. The luminous matter of objects between a far source and the Earth is often found to be significantly less with respect to the total mass derived from lensing. [27].

Usually we distinguish two different regimes of gravitational lensing, depending on the extent of the effect. When the light of distant sources is deflected at large angles, allowing to easily observe and measure the effect, we are in the so-called strong lensing regime (See Fig.1.2). In this case astrophysical systems can give rise to spectacular optical phenomena such as multiple images, giant arcs and Einstein's rings at extremely high magnifications. In this regime the technique is extremely powerful, but it can be applied quite rarely because there are not many objects in sky which are so massive that they can cause such a sizeable effect. On the other hand, for the most of the galaxies visible from Earth the deflection angle is small so their shape is altered only by 1% and consequently they are studied in the so-called weak lensing regime. Therefore, as the appreciable effects are weak, it is necessary to use a statistical approach studying the average effect on a set of galaxies. In particular, roughly approximating the shape of galaxies to an ellipse and assuming they are randomly oriented in the sky, any orientation in a privileged direction indicates a distortion of their shape, due precisely to the weak lensing. So any deviation from a random distribution of the galaxies orientations can be used to estimate the gravitational lensing and, accordingly, the amount of mass which causes the distortion [28].

Mass measurements - obtained with the gravitational lensing in both regimes - do not agree with the mass values obtained from luminosity measurements. The M/L values obtained are between 10 and 20 for the galaxies and between 100 and 300 for clusters, so these are very strong indications of the existence of dark matter.

Famous example: Bullet cluster

A significant example of measuring the mass of an astrophysical system using different techniques is that of the so-called Bullet Cluster shown in Fig.1.3. The Bullet Cluster consists of two clusters of galaxies which have collided with each other. Assuming that each cluster is composed mainly of stars, intergalactic hot gas and dark matter, it is possible to study these three ingredients separately and show that they exhibit different behaviour during the collision. In particular, by making an optical measurement it is observed that the stars of the galaxies did not undergo strong effects due to the clash between the two clusters. By observing instead the emission of X-rays due to the presence of hot gas, which makes up most of the clusters' baryonic mass, we can see how the electromagnetic interactions have slowed down the gas. Finally, through measures of gravitational lensing we obtain the overall mass distributions of the two clusters which appears to be located on both sides of the luminous matter. These observations suggest that the most of the mass content has passed through interacting perhaps only weakly as well as gravitationally. This is one of the most compelling hints in favor of the existence of a non baryonic dark matter.

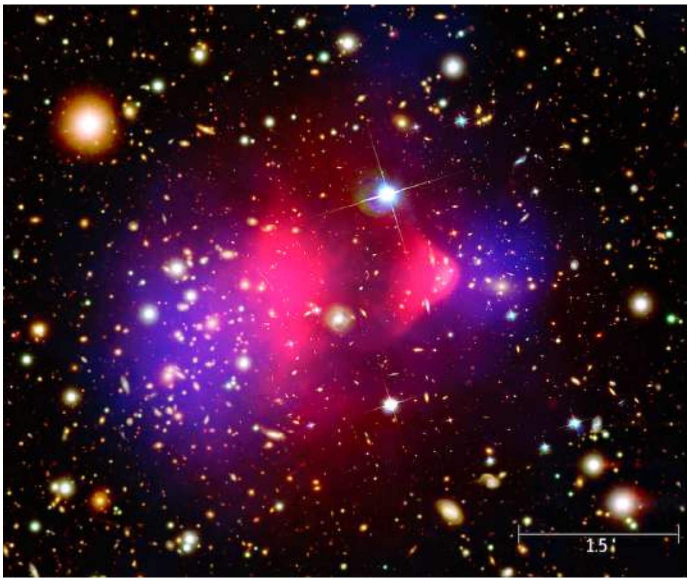

Fig. 1.3 The image, which is a composite of optical data, X-ray data in pink and a mass map deduced from gravitational lensing, shows the collision of two galaxies clusters, the so-called Bullet Cluster. The hot gas distribution, seen as the pink clumps, contains the most of the baryonic matter, while the blue areas show where the most of the mass is. The separation between pink and blue areas gives evidence that a great amount of matter is non-baryonic, *i.e.* dark. Image Credit: X-ray: NASA/CXC/CfA/ M. Markevitch et al.

1.1.4 CMB

Nowadays the most widely accepted cosmological model is the Big Bang cosmological model and, in particular, its simplest parametrization, the so-called ΛCDM (Lambda Cold Dark Matter) paradigm [29, 30]. As the name indicates, the two basic ingredients are cold dark matter and dark energy, the last associated to the cosmological constant Λ. The adjective *cold* means that the thermal distribution of dark matter had to be cold, that is, not relativistic, at the time of its decoupling. This property is linked to the formation of large-scale structures, as we will see later.

The reliability of this model is based on four fundamental pillars which highlight the agreement between predictions and observations:

- the properties of the cosmic microwave background (CMB);
- the distribution of large-scale structures;
- the abundance of hydrogen and helium;
- the accelerated expansion of the Universe.

To understand the strength of these evidences it is necessary to take a step back and to briefly describe the cornerstones of the model we use to give the most realistic picture of our Universe. We can consider the Einstein equation as a starting point, which shows how the geometry of the Universe is determined by the distribution of energy and momentum within it. This equation, if resolved under the hypothesis of a homogeneous and isotropic Universe, *i.e.* assuming the metric of Robertson and Walker,

$$ds^2 = -c^2dt^2 + a(t)^2\left(\frac{dr^2}{1-kr^2} + r^2d\Omega^2\right) \tag{1.2}$$

where $a(t)$ is the scale factor and k is a constant that describes the space curvature, leads to the Friedmann equation

$$\left(\frac{\dot{a}}{a}\right)^2 + \frac{k}{a^2} = \frac{8\pi G}{3}\rho_{tot} \tag{1.3}$$

with G Newton's gravitational constant and ρ_{tot} the total energy density of the Universe. If $k = 0$ that corresponds to a flat space, the density is called critical density and can be written as

$$\rho_c \equiv \frac{3H^2}{8\pi G} \tag{1.4}$$

having introduced the Hubble parameter $H(t) = \dot{a}(t)/a(t)$. It is possible to express the abundance of a species in the Universe, denoted as ρ_i, with respect to the critical density ρ_c:

$$\Omega_i \equiv \frac{\rho_i}{\rho_c} \tag{1.5}$$

The contributions to the total energy density of the Universe ρ_{tot} are: the radiation density ρ_r, which accounts for all relativistic particles, the matter density ρ_m, which can be separated in baryonic mass density ρ_b and dark matter density ρ_{CDM}, and the dark energy density ρ_Λ. To be more precise the ρ_m should take into account both baryons and leptons, but, since the electron mass is ~2000 times smaller than the proton's one, the leptons are neglected and we usually refer to baryonic mass density. During the expansion of the Universe different species diluted at different rates: ρ_r scaled like a^{-4}, while ρ_m like a^{-3}. First there was the so-called radiation-dominated phase when energy density in radiation exceeded that in matter and $a \sim t^{1/2}$. Later, when temperature was such for which $k_BT \sim 3$ eV, the Universe became matter dominated and $a \sim t^{2/3}$ [22, 31]

Now let's see how in this framework the study of the CMB, and in particular of its temperature anisotropies, allows to show the need of dark matter and also to estimate ρ_{CDM}.

After the period of inflation the Universe was a hot and dense plasma made of baryons

(nuclei) and electrons in thermal equilibrium. Photons and charged particles were coupled, making the plasma opaque to light. In this plasma the contrast between gravitational force and pressure has generated density variations, which have propagated acoustic waves. These periodic waves go under the name of baryonic acoustic oscillations (BAO). About 380,000 years after the Big Bang, due the Universe expansion, as we said, the temperature decreased, so particles energy fell below ionization threshold. From this moment began an epoch called recombination during which baryons and electrons started to form neutral atoms; after this period the Universe became transparent and photons were able to freely travel in space. Photons that have free streamed until today are what we call cosmic microwave background (CMB), which has now a black-body temperature of 2.725 K. The density fluctuations occurred during recombination depend on the particle physics that was happening at that time, so they carry significant information about two crucial aspects of our Universe: the growth of structures and the total amount of dark matter present [32]. The BAO caused small temperature inhomogeneities at the photon decoupling time and these are mapped into the CMB temperature anisotropies.
After many experiments, in 2013 the Planck collaboration measured with great precision the CMB anisotropies at the 10^{-5} level [4]. It is possible to relate these temperature fluctuations to the matter density fluctuations, but the baryon density alone is too small to grow into the structures we populate our Universe today. The growth of the structures can be quantitatively explained with the assumption that the process started before the recombination, with the formation of dark matter aggregates. During the matter dominated era, the baryonic matter would have collapsed in the gravitational potential wells of these aggregates, forming structures. Without cold dark matter non-baryonic species, there is no way the structures would have become like we observe today. In particular the hypothesis of a non-relativistic dark matter at the time of decoupling is significant because with decreasing temperature - hence kinetic energy - particles are progressively more gravitationally bounded and this speeds up the formation of structures.

To extract the dark matter amount from the CMB map the idea is to fit the angular power spectrum to the cosmic parameters, in particular Ω_b and Ω_{CDM}. The power spectrum is a way of evaluating the temperature anisotropies, because it is obtained by measuring the deviation from the mean temperature in each point and then decomposing it in spherical harmonics (See Figs.1.4 and 1.5).

The relative amplitude of the peaks depends on the abundance of different species at the "photon freeze-out" [30, 33] and this allows the calculation of the dark matter density ρ_{CDM}. From the ratio of the odds to the even peaks heights it can be inferred the baryon density Ω_b. Instead the subsequent peaks amplitudes depend on the matter density Ω_m, so it is possible

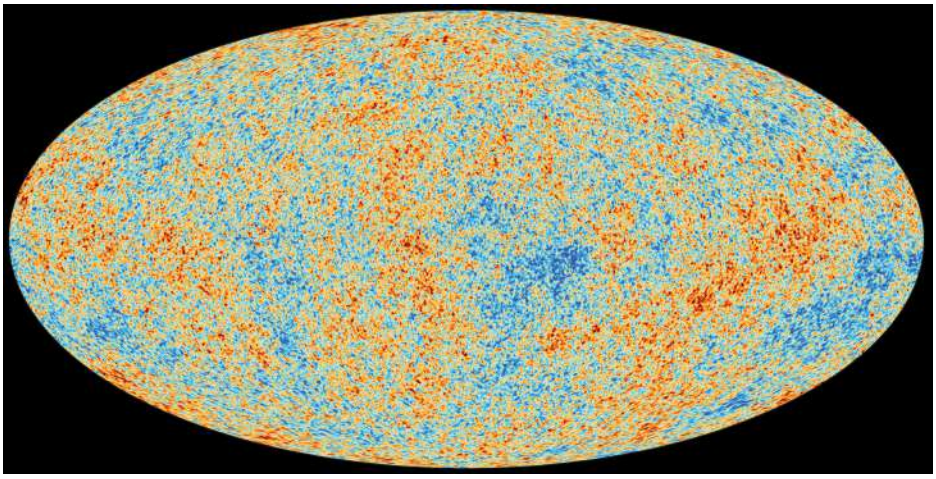

Fig. 1.4 The Cosmic Microwave Background (CMB) as recorded by the Planck satellite. The image is the result of the subtraction of all the spurious effects given by microwave sources in and outside the galactic plane and by Earth's, Sun's and galactic motions with respect to the CMB reference frame [4].

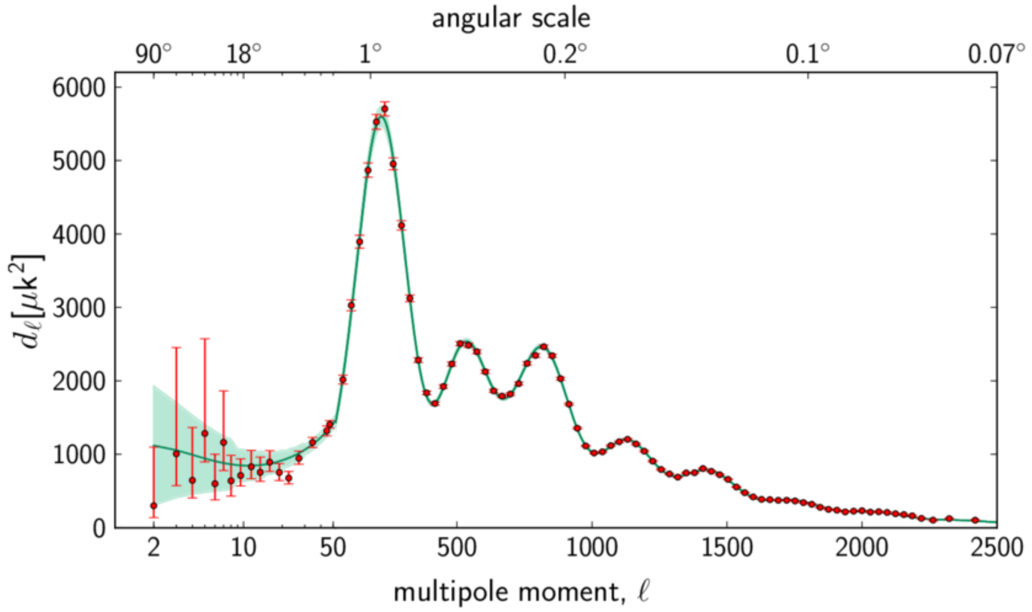

Fig. 1.5 The CMB angular power spectrum: red points are data as recorded by the Planck mission, the green line is the best fit obtained with the ΛCDM model. The ratio among the first and second peak heights allows to calculate the baryon density, while the ratio among the second and third peak heights gives the total matter density [4].

to evaluate separately the parameters. Recent values, from the Planck Collaboration, in terms of the reduced Hubble constant ($h = H_0/(100\ kms^{-1}Mpc^{-1})$) are $\Omega_m h^2 = 0.1426 \pm 0.0020$, $\Omega_b h^2 = 0.02222 \pm 0.00023$ and $\Omega_{CDM} h^2 = 0.1197 \pm 0.0022$. These results show that dark matter is five times more abundant than baryonic matter.

1.1.5 Big Bang Nucleosynthesis

Big Bang Nucleosynthesis (BBN) provides an independent measurement of Ω_b that reinforces the fact that baryonic matter can be just the 4% of the Universe [34]. The BBN gives a description of the light nuclei production mechanism, during the first minutes after the Big Bang. After the hadrons formation the primordial nucleosynthesis starts: the first element to be produced is stable deuterium and, immediately after, ^{3}He, ^{4}He and ^{7}Li. Using nuclear physics and numerical simulations, predictions of the abundances can be obtained and compared with the found values. The abundances depend significantly on the baryonic density and are consistent with $\Omega_b \sim 0.04$ [31]. This is a further incontrovertible evidence of the existence of a non-baryonic dark matter component of the Universe.

1.1.6 N-body simulation

Further evidence of the existence of dark matter comes from the study of large-scale structure formation. The model of the evolution of such structures starting from primordial density fluctuations is extremely complex and needs to take into account many different aspects. The most used approach to tackle the problem is that of N-body simulations.

The basic idea is to hypothesize an initial density distribution, which describes the primordial Universe, and simulate its evolution over time based on gravitational interactions. Already in 1973, while Vera Rubin observed the rotation curves of the galaxies, Jeremiah Ostriker and James Peebles simulated their temporal evolution. According to the results they obtained, galaxies similar to the Milky Way would have had to collapse towards the center in less than an orbital period. Conversely to reproduce the shapes of galaxies observed in the sky it was necessary to add a mass distribution of 3 to 10 times higher.

Currently the simulations are much more complex as they take into account the dynamics of gas, possible chemical reactions and other factors; moreover, thanks to the increase of the computing power, they are much more accurate. Assuming the presence of a halo of dark matter, whose density is usually parametrized as follows

$$\rho(r) = \frac{\rho_0}{(r/R)^{\gamma}[1+(r/R)^{\alpha}]^{(\beta-\gamma)/\alpha}} \tag{1.6}$$

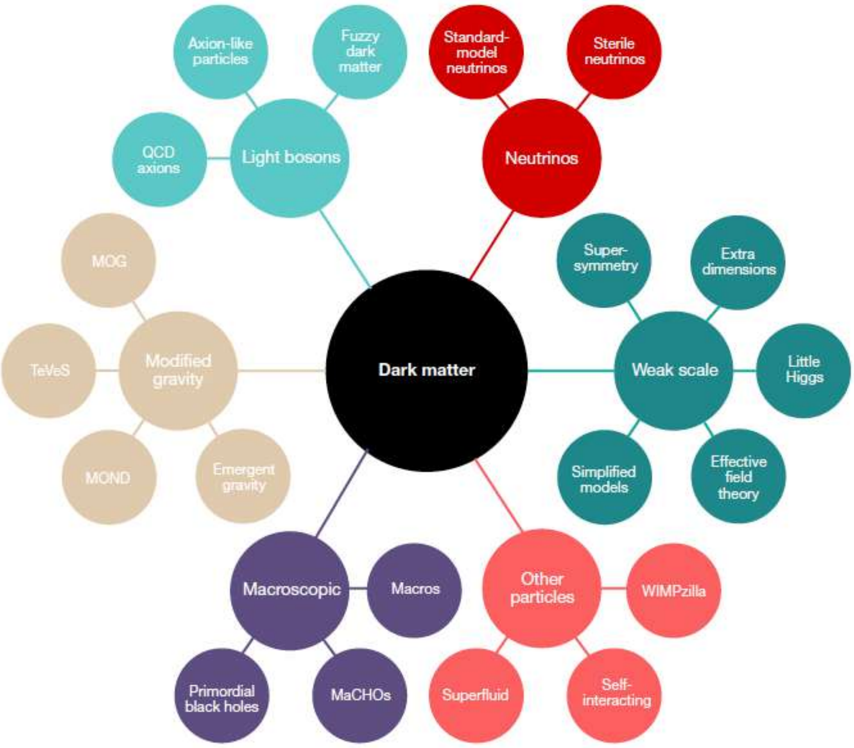

Fig. 1.6 Graphical representation of the most of the dark matter candidates currently under investigation, divided in families [5].

the N-body simulations are able to reproduce the galaxies distribution observed in recent large scale surveys and this is another results that supports the reliability of the ΛCDM paradigm. However have emerged several issues with the N-body simulations model, such as the "Core-Cusp" problem and the "too big to fail problem". As the discussion of these topics goes beyond the scope of my thesis, please refer to Ref. [35, 36].

1.2 What could it be made of?

From the observations described in the previous section it is possible to obtain a generic sketch of a valid dark matter candidate. There are numerous and various possible extensions of the Standard Model that can provide particle dark matter candidates, but among the different proposals it is possible to identify some common criteria that must be satisfied. Dark matter particles should be:

- electrically neutral, because they don’t interact electromagnetically;
- with no colour charge, because they do not feel strong interaction;

- stable on cosmological timescales, otherwise they would have already decayed;
- coupled to standard particles, as well as by gravitational force, at most at the weak interactions scale.

The various models can be divided into two large categories: those that propose relativistic candidates, which we refer to as "hot" dark matter, and those that are based on non relativistic particles, the so-called "cold" dark matter. As already mentioned, most of the dark matter must be cold in order to explain the formation of the structures in the early stages of the Universe. This does not entirely exclude the existence of hot dark matter (like neutrinos), but limits its contribution to no more than $\sim 1\%$ of the total.

1.2.1 MACHOS and primordial black holes

The first hypotheses for solving the missing mass problem were made within the baryonic matter framework. It was simply thought of a class of massive non-luminous objects that could populate the galaxies halos: basically residuals of dead stars, such as brown dwarfs and neutron stars. This family of astronomical bodies is usually referred to by the acronym MACHOs, which stands for MAssive Compact Halo Objects. Using gravitational lensing effects for low masses, of the order of 10^{-7} solar masses, several experiments looked for MACHOs during the past decades. However the results obtained with micro-lensing show that these candidates could explain at most 20% of the effect due to the dark matter [37].

Another possible dark matter candidate are black holes. Of particular interest are the primordial black holes, generated in the early phases of the Universe and therefore possibly not ruled out yet by cosmological constraints [38]. These objects would also be stable on cosmological scales, because Hawking radiation is a very slow process. After the detection of gravitational waves it has been hypothesized that the binary back holes which generated the waves could be primordial and this has renewed interest in this candidate [39]. However, there are stringent constraints that disfavour the idea that a large population of primordial black holes is the main constituent of dark matter [5].

1.2.2 Sterile neutrinos

The standard model describes three neutrino flavours - ν_e, ν_μ, ν_τ - with a non-zero mass and weakly coupled with their respective charged leptons. Neutral, massive, weakly interacting particles, neutrinos appear to be the natural candidate for dark matter. The Planck experiment results fix an upper limit on the neutrino total mass in the interval between $(0.340 - 0.715)$

eV, depending on the data used [4]; adding also data from the BAO the limit becomes $\sum_j m_j < 0.170$ eV. For a complete review on the neutrino masses see [7]. This means that neutrinos were relativistic at the decoupling time. Being hot dark matter they cannot have contributed to the large structure formation, because they would have free-streamed under gravitational force. So standard neutrinos can be a fraction of the dark matter content of the Universe, but for sure not the prevalent component of it.

However, there is an extension of the neutrino family which consists in introducing a new particle, the sterile neutrino, that could be a valid candidate for dark matter. Generally a sterile neutrino is defined as an electrically neutral massive particle, which does not interact through any fundamental force, except gravity. More specifically it could be either a right-handed neutrino not able to couple with leptons, or a new flavour of neutrino which could only oscillate into a known flavour. There are no stringent indications on the mass range of sterile neutrinos, but for having played a role in the formation of structures they must be non-relativistic [40]. So the picture would also be consistent with Planck's bounds on masses because they concern exclusively relativistic species. These neutrinos must also decay very slowly to play the dark matter role today, but statistically someone can be decayed causing an emission of photons. For this reason it has been suggested that the anomalous observation a 3.5 keV spectral line in the X-ray spectrum of 73 clusters of galaxies may be associated with the decay of sterile neutrinos [41].

1.2.3 Axions

The axion is a hypothetical neutral pseudo scalar particle postulated in 1977 by Robert Peccei and Helen Quinn in a completely different context from the dark matter search [42]. It was introduce to solve the so-called CP problem in quantum chromodynamics (QCD). In short, the CP problem consists in the fact that the strong interactions Lagrangian should violate the CP symmetry, but this breaking of symmetry is not observed experimentally. Peccei and Quinn proposed a spontaneous breaking of a new U(1) chiral symmetry, whose associated Goldstone boson would be the axion. If they exist and are abundant enough, axions could constitute a dark matter candidate because of their weak coupling with ordinary matter. For masses between 10^{-5} eV and 10^{-3} eV they would have long enough lifetime, even if they are not stable particles [43]. Axions should convert into two photons and this is the basic principle of present experiments. In particular the so-called "light through wall" experiments produce photons in one resonant cavity, try to convert them into axions which should pass through the wall and finally look for photons in a second cavity on the other side of the wall [7].

1.2.4 WIMPs

The acronym WIMP stands for Weakly Interacting Massive Particle and identifies the most generic massive dark matter candidate, usually indicated with χ. The WIMP is a stable and neutral particle, interacting with the particles of the standard model at the weak scale and not relativistic at the time of decoupling, its mass range goes from a few GeV up to tens of TeV. The weakly interacting massive particles represent the class of candidates which has obtained the most attention in the past decades from both from theoretical and experimental point of view [44]. One natural possibility was the supersymmetric neutralino, but supersymmetry searches at colliders up to $\sqrt{s}$ = 13 TeV have only given null results [7]. However, there are many other different candidates that belong to the large WIMP family, in my thesis I am interested in the general WIMP characteristics, for a more specific review see [6].

WIMPs relic density

WIMPs have become so famous because of the so-called *WIMP miracle*. The core of the argument is that the correct relic density of WIMPs arises assuming an annihilation cross-section of the order of magnitude of the weak interaction for the following reaction:

$$\chi + \chi * \longrightarrow \ell^+ + \ell^- \tag{1.7}$$

The general assumption is that WIMPs were produced thermally, *i.e.* in the early Universe, when $k_B T \gg m_\chi c^2$, they were produced in collisions between standard particles and antiparticles. There was an equilibrium between the production process and the WIMP annihilation, the equilibrium rate was:

$$\Gamma_A = \langle \sigma_A v \rangle n_{eq} \tag{1.8}$$

with σ_A annihilation cross-section, v WIMPs relative velocity and n_{eq} number density at equilibrium. As the Universe expanded and the temperature fell down, WIMP decoupling occured: the rate decreased progressively, until WIMP production and annihilation stopped. From that moment the number density began to vary following a trend inversely proportional to the volume of the Universe. In particular the evolution of n can be written as:

$$\frac{dn}{dt} = -3Hn - \langle \sigma_A v \rangle (n^2 - n_{eq}^2) \tag{1.9}$$

where the first term on the right side takes into account that an expanding Universe leads to WIMP dilution and the second is related to production-annihilation rates. Rewriting equation 1.9 including the entropy conservation law and exploiting the relation between mass density

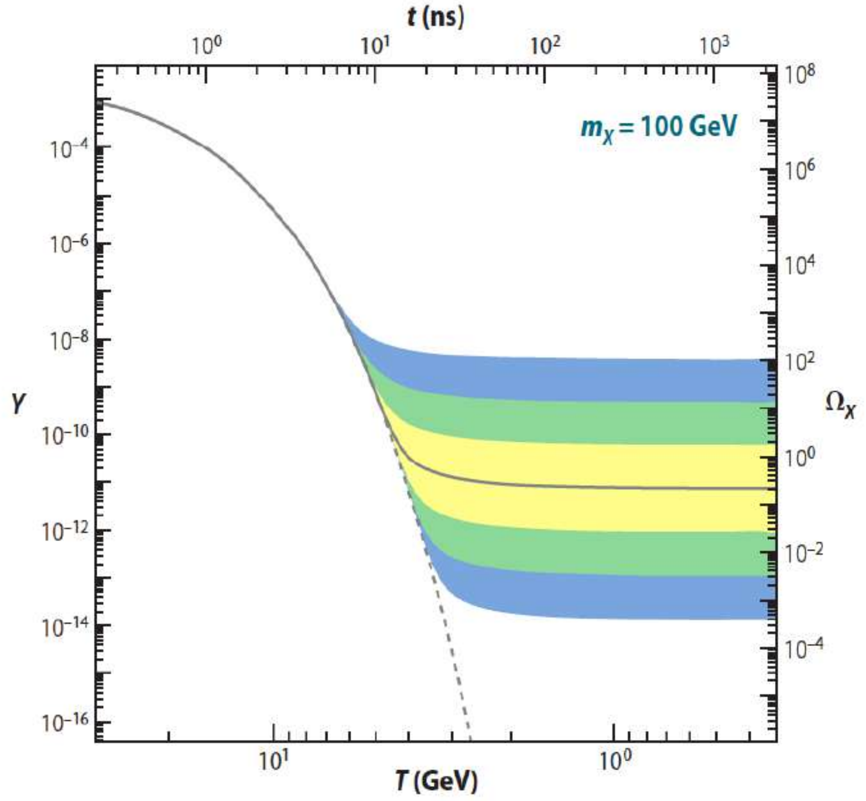

Fig. 1.7 The number density Y and corresponding thermal relic density Ω_χ of a 100 GeV mass WIMP, as a function of temperature and time. The solid gray contour is for an annihilation cross-section that yields the correct relic density, while the coloured regions are for cross-sections that differ by 10, 10^2, and 10^3 from this value. The dashed gray line is the number density of a particle that remains in thermal equilibrium [6].

and Hubble parameter (see Eq. 1.3) we have

$$\frac{dY}{dx} = -\sqrt{\frac{\pi}{45G}}\frac{g_*^{1/2} m_\chi}{x^2}\langle\sigma_A v\rangle(Y^2 - Y_{eq}^2) \tag{1.10}$$

where $Y = n/s$ with s the entropy density, $x = m_\chi/T$ and $g_*^{1/2}$ is a parameter that takes in account the degrees of freedom. A numerical solution of equation 1.10 is shown in figure 1.7. It's interesting to note that there is an inverse relation between the annihilation cross-section and relic density, because WIMPs with weaker interactions (small σ_A) freeze out when the temperature is higher, so their density is enhenced. This is described by the following approximate relation.

$$\Omega_{DM} h^2 \simeq \frac{3 \cdot 10^{-27} cm^3 s^{-1}}{\langle\sigma_A v\rangle} \tag{1.11}$$

So going back to the *WIMP miracle*: if you plug into equation 1.11 a cross-section of the order of the weak scale, $\sim 10^{-39}$ you can obtain a $\Omega_{DM}h^2$ value according to the measurements and this puts constraints on the WIMP mass range and cross-sections [6].

1.2.5 Light WIMPs

Investigating the possibility that dark matter could be made of particles with masses between few GeV and few TeV has been done since decades. But since in the last few years all the experiments looking for GeV-TeV WIMPs have not observed any signal (except the DAMA/LIBRA experiment hint, see section 1.3.3), the search for WIMP candidates in a different mass range has intensified [45].

Low mass dark matter particles have not been considered in the past because they did not seem to have the right relic density. In particular, small masses were associated to low annihilation cross-sections, giving rise to an excessively large relic abundance. This argument is valid if we assume WIMPs to be fermions, because in this case the σ_A is proportional to m_χ^2 [16]. On the contrary if we consider a scalar candidate the relic density depends on the coupling with ordinary matter. There are two main possibilities: either the bosonic WIMP interacts through not yet discovered fermions and this will lead to an asymmetry between dark matter particles and antiparticles, or the mechanism is based on exchanging a new neutral boson [46, 47] . In both cases the relationship between Ω_{DM} and σ_A does not depend strongly on the dark matter particle mass .

Because of the existence of candidates a number of direct detection experiments targeting WIMPs through nuclear recoils have also been actively working to increase their sensitivity to smaller energy depositions and lighter DM candidates [48]. Among these, the DarkSide project, on which I worked during my graduate school, is investigating the low mass region using new analysis techniques [12]. For more details see section 3.1.3.

1.2.6 No dark matter: MOND

It is possible to totally overturn the point of view and try to explain all the evidence described in section 1.1 without introducing a new matter species but assuming a modified law of gravity. In 1983 Mordehai Milgrom proposed the idea of Modified Newtonian Dynamics (MOND) applied to galaxies [49]. His model claims that for very low accelerations, below a typical value a_0, the acceleration itself reduces to $a = \sqrt{a_0 \nabla \Phi_N}$, with Φ_N the gravitational field. Small accelerations correspond to large distances from the galactic center, so it can be

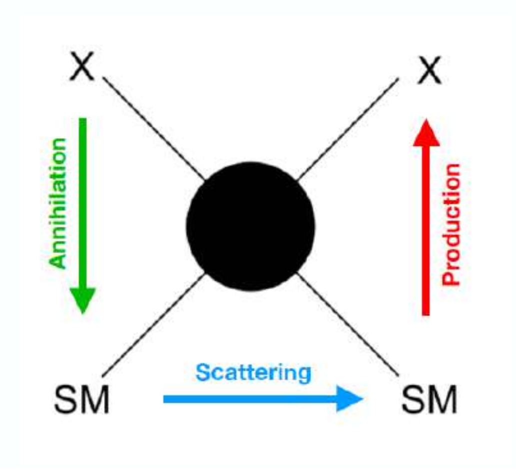

Fig. 1.8 Sketch of the three possible dark matter interactions. Reading it from top to bottom, following the green arrow, the diagram represents two dark matter particles that annihilate producing standard model products. Vice versa, from bottom to top, along the red arrow, the drawing shows an hypothetical dark matter production. Finally the light blue arrow indicates the possible dark matter scattering on a standard particle.

assumed $|\nabla\Phi_N| \sim GM/r^2$ and then the circular velocity v_c can be written as

$$v_c^4(r) \sim GMa_0 \tag{1.12}$$

If on the one hand the strength of MOND is that a flat rotation curve is obtained without the need to invoke dark matter, on the other the biggest problem is that it still does not reproduce the features of large scale structure, CMB anisotropies and more importantly the Bullet Cluster behaviour with the same success as ΛCDM [50]. Many theories of modified gravity have been recently ruled out by the gravitational waves detection by the LIGO/VIRGO collaboration [51, 39].

1.3 Dark Matter detection

After examining the evidences of dark matter and its candidates, the possible detection techniques remain to be analyzed. It may be useful to schematize the hypothetical interactions of dark matter with a rough sketch, as in Fig. 1.8, and starting from possible interaction channels go through different way of catching dark matter signals. Following the diagram from bottom to top we have two particles of the Standard Model that interacting produce two dark matter particles. This is the typical event that one tries to reproduce at high energy colliders, such as the Large Hadron Collider (LHC). Any dark matter particles produced would escape the detectors, so what we are looking for is missing energy and momentum, associated precisely with the escaped particles. Despite the numerous efforts that are currently pursued at the LHC, there has been no evidence of particle dark matter observed so far.

If instead we read the scheme from top to bottom we have the depiction of dark matter annihilation, where the products are assumed to be ordinary matter. Looking for an excess of Standard Model particles - gamma rays, neutrinos, anti-nuclei - is what we call indirect detection.

Finally we can consider a dark matter scattering process, described from left to right in Fig. 1.8, which will leave some recoil energy to the target, that may be measured. In particular WIMPs with GeV-scale masses are expected to produce nuclear recoils at the keV energy scale (See Eq.1.16). Because of the low recoil energy and also of the low cross-section direct search experiments need to fulfill several requirements as we will see in section 1.3.2.

Since during my graduate school I worked on a direct detection experiment (see chapter 3), in the following of this section I will briefly describe the interaction principle and the most significant experimental techniques. As the dark matter candidate I will refer to WIMPs because they are the most generic and widely searched.

1.3.1 WIMPs rate and cross-section

f If we consider a WIMP elastic scattering on nucleus we can write the event rate for recoil energy as:

$$\frac{dR}{dE_R} = N_t \Phi_\chi \frac{d\sigma}{dE_R} \tag{1.13}$$

where E_R is the recoil energy, N_t is the total number of particles in the target, Φ_χ is the dark matter flux and $d\sigma/dE_R$ is the differential cross-section. Let's analyse all the three ingredients:

- N_t can be written as the ratio between the total target mass and the nuclei mass. If we consider a unit mass detector we obtain $N_t = 1/m_N$, denoting with m_N the nuclei mass.
- The dark matter flux can be expressed as a function of the density and the velocity distribution. In particular $\Phi_\chi = n_\chi v f(v) dv$, where n_χ is the number density, which in turn can be written as the ratio between the mass density and the mass of the WIMP $n_\chi = \rho_\chi / m_\chi$.
- The cross-section must be related to the differential scattering cross-section per solid angle, as we will see below.

So it is possible to rewrite the rate, integrating over all the possible velocities:

$$\frac{dR}{dE_R} = \frac{\rho_\chi}{m_N m_\chi} \int_{v_{min}}^{+\infty} v f(v) \frac{d\sigma}{dE_R} dv \tag{1.14}$$

where the cross section stays inside the integral because it depends on velocity, v_{min} is the minimum velocity need to have a nuclear recoil of energy E_R, $v_{min} = \sqrt{2m_N E_R}/2\mu_{\chi N}$.

Differential scattering cross-section The starting point is the differential scattering cross-section per solid angle for the WIMP-nucleus interaction [52]. In a non-relativistic approximation the energy in center of mass can be expressed as the mass sum so we obtain

$$\frac{d\sigma}{d\Omega} = \frac{1}{64\pi^2} \frac{1}{(m_\chi + m_N)^2} \frac{p_f}{p_i} |\mathcal{M}|^2 \tag{1.15}$$

where p_i and p_f are the initial and final momenta and $\mathcal{M}$ is the scattering amplitude. Considering a zero momentum transfer frame $p_i = p_f$ and the recoil energy can be expressed as

$$E_R = \frac{\mu_{\chi N}^2 v^2}{m_N}(1 - cos\theta_{cm}) \tag{1.16}$$

with $\mu_{\chi N} = m_\chi m_N/(m_\chi + m_N)$ the WIMP-nucleus reduced mass and θ_{cm} the scattering angle in the center of mass reference frame. It is also useful to report the recoil energy as a function of the recoil angle in the laboratory frame, that we will denote as θ_R.

$$E_R = 2\frac{\mu_{\chi N}^2 v^2}{m_N} cos^2\theta_R \tag{1.17}$$

So combining this expression with $d\Omega = dcos\theta d\varphi$:

$$\frac{dE_R}{d\Omega} = \frac{\mu_{\chi N}^2 v^2}{2\pi m_N} \tag{1.18}$$

At this point from $d\sigma/d\Omega$ and $dE_r/d\Omega$ we have

$$\frac{d\sigma}{dE_R} = \frac{|\mathcal{M}|^2}{32\pi m_\chi^2 m_N v^2} \tag{1.19}$$

We will not go into the detail of the scattering amplitude calculation, but let's say that we can separate the interaction and therefore the cross-section into a spin-dependent part and spin-independent part. Below we will consider only the spin-independent cross-section and the associated amplitude is

$$|\mathcal{M}|^2_{SI} = 16 m_\chi^2 m_N^2 |f_p Z + f_n(A-Z)|^2 |F(q)|^2 \tag{1.20}$$

where Z and A - atomic and mass numbers respectively - depend on the target nucleus, f_p and f_n are the WIMP couplings to the proton and neutron and $F(q)$ is the nuclear form factor that carries a momentum dependence.
So the cross-section becomes

$$\frac{d\sigma_{SI}}{dE_R} = \frac{m_N}{2\pi v^2} |f_p Z + f_n(A-Z)|^2 |F(q)|^2 \tag{1.21}$$

It is very useful to have an expression independent from the target nucleus, to be able to compare results from different experiments. So it is common to rewrite Eq. 1.21 in terms of the WIMP-nucleon cross-section, with $\sigma^n_{SI} = \sigma^{neut}_{SI} = \sigma^{prot}_{SI}$

$$\frac{d\sigma_{SI}}{dE_R} = \frac{m_N \sigma^n_{SI}}{2\mu^2_{\chi p} v^2} |Z + \frac{f_n}{f_p}(A-Z)|^2 |F(q)|^2 \tag{1.22}$$

where $\sigma^n_{SI} = \mu^2_{\chi p} f_p^2/\pi$ with $\mu_{\chi p}$ is the WIMP-proton reduced mass.

Going back to Eq. 1.14 and substituting the spin-independent cross-section we obtain:

$$\frac{dR}{dE_R} = \frac{\rho_\chi}{2 m_\chi \mu^2_{\chi p}} \sigma^n_{SI} |Z + \frac{f_n}{f_p}(A-Z)|^2 |F(q)|^2 \int_{v_{min}}^{+\infty} \frac{f(v)}{v} dv \tag{1.23}$$

Usually WIMPs are considered to be distributed as an isothermal sphere with an isotropic Maxwellian velocity distribution, with upper limit the escape velocity. With these assumptions - which form the so-called Standard Halo Model (SHM) - the velocity integral results in a roughly exponential spectrum and the rate can be simplified as:

$$\frac{dR}{dE_R} \propto A^2 F^2(q) e^{-\frac{E_R}{E_0}} \tag{1.24}$$

where $E_0 = 2\mu^2_{\chi N} v_0^2 / m_N$ and with v_0=220 km/s that is the average speed relative to the Earth. It is important to note the there is an A^2 dependence, which corresponds to the fact that heavier elements are expected to see higher rates for a fixed target mass. It is also significant that the rate decreases exponentially with E_R, specifically for threshold energies in the detectors.

1.3.2 Direct detection techniques

As already mentioned, one of the peculiar characteristics of dark matter detectors is a low threshold in energy, to identify nuclear recoils induced by WIMPs. Moreover, due to the low expected rate of events, it is needed a detector where it is possible to monitor and then discard all the background signals. This also allows to have large volumes of target material, to improve sensitivity. Typically the physical signals used are heat, scintillation light or ionization charge. Many experiments are based on the combination of two of these signals.

Scintillation light

The scintillation mechanism is basically when excited atoms of a material emit optical photons. In particular if a particle deposits energy in a scintillator its molecules go in an excited state and then de-excite emitting light. To have a good scintillator it is important that the material is transparent to its own light. Usually the number of photons produced is proportional to the energy deposition, so it is possible to perform an estimation of the energy deposited in the scintillator.
Not all scintillators can be used in the dark matter search, only a few materials can reach the levels of radio purity necessary for low background experiments such as those we are talking about. These scintillators are divided into two great categories: noble cryogenic liquids (typically argon or xenon) and crystals (for example NaI or $CaWO_4$). Scintillation light is then detected using many different kinds of photosensors, depending on the experimental setup.

Ionization charge

When the incoming particle deposits enough energy inside the target, some of the atoms may be ionized, generating free electrons. With the presence of an electric field, these electrons are drifted away from the positive ions, to avoid recombination and then they are collected or converted. In some cases the charge is measured directly using for example semiconductor detectors; in other kind of systems, like time projection chambers filled with noble liquids, the electrons are subjected to a very high electric field so they discharge into gas producing light.

Heat

A nuclear recoil in a crystal lattice generates phonons, *i.e.* collective excitation of lattice atoms. Phonons cause a tiny temperature variation in the target material and using bolometers

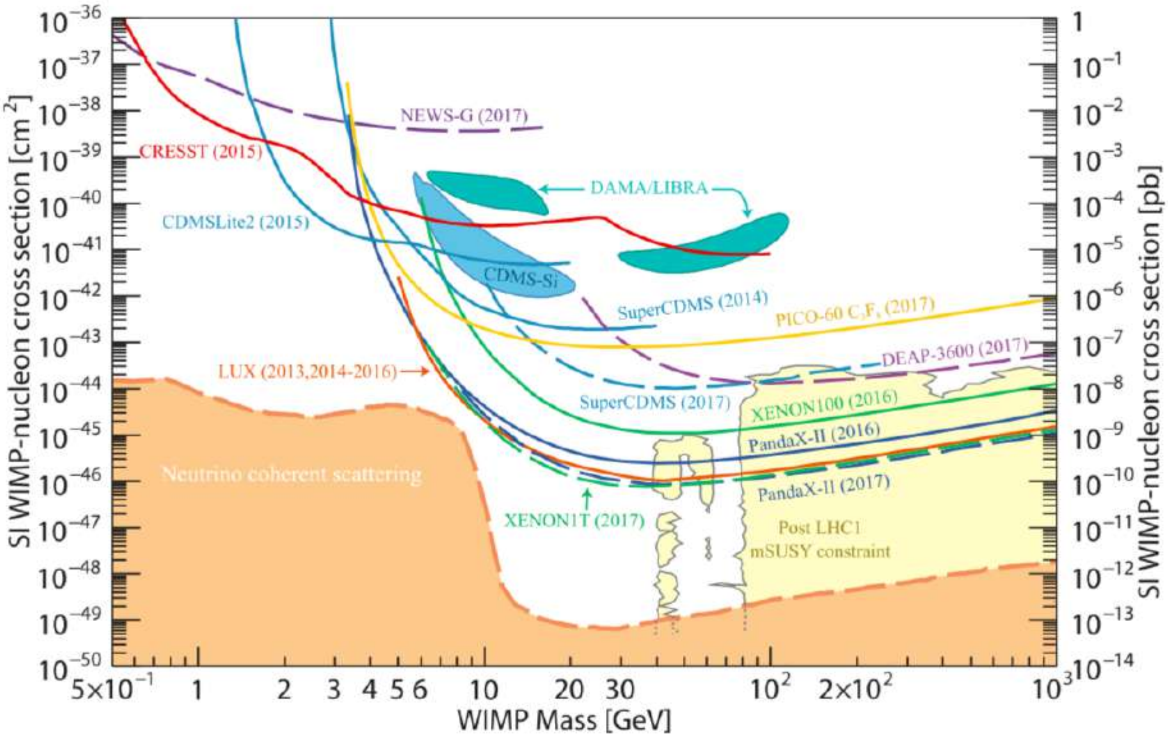

Fig. 1.9 Spin-independent WIMP-nucleon cross-sections versus mass. The open lines are some of the current best exclusion limits, while enclosed areas are regions of interest from possible signal events [7].

it is feasible to detect this heat. The crystal used are cooled down to cryogenic temperatures and covered usually with tungsten films. Measuring a change in its resistivity you can reconstruct temperature variations of the order of μK.

A different technique which also exploits heat is the use of cryogenic bubble chambers. The basic principle is to observe bubbles produced by a recoil that causes a phase transition from superheated liquid to vapor.

1.3.3 Direct detection status

Dark matter direct detection results are typically given showing the spin-independent WIMP-nucleon elastic scattering cross-section as function of the particle mass. The different results of the various experimental techniques described are summarized in the plot in Fig.1.9. The region of masses above 100 GeV has been explored by a large number of experiments, but for now they were only able to set upper exclusion limits, which are represented by the open curves.

As regards experiments with noble liquids a large progress in sensitivity has been made, as shown by many interesting results: on the one hand there are the limits set by XENON [53, 54] and LUX [55], both based on a dual-phase xenon Time Projection Chamber (TPC), on the other side the ones set by DEAP [56] and XMASS [57] that use an argon target in single phase and by DarkSide, using a dual-phase argon TPC [11]. However no hints of a signal have been observed so far.

The DAMA/LIBRA case Closed curves highlight the preferred regions of the parameter space for experiments which found a significant signal excess in their data. The most famous example of such a situation is the DAMA/LIBRA experiment [58, 59], based on NaI scintillating crystals, which measured an effect of annual modulation in the event rate. These results, despite their robustness, are difficult to reconcile with other experiments under simple hypothesis, making the interpretation controversial. In the future the SABRE experiment could give some crucial hints performing a simultaneous measurement in the northern and southern hemispheres [60].

Finally the orange dashed line is the so-called neutrino floor. The orange region below is the area of the parameter space in which the sensitivity of the detectors could allow them to see the coherent scattering of neutrinos on nuclei at a rate equal or higher than a hypothetical WIMP signal. Since coherent scattering of neutrinos on nuclei would be indistinguishable from WIMP-induced nuclear recoils, performing a search inside or even near that area will require a really careful evaluation of the ν-induced background. In this regard, R&D projects are underway to study directional sensitivity: in particular, during my thesis I worked on the ReD-Recoil Directionality experiment, which I will discuss later in detail (see chapter 4). To push the limits down to the neutrino floor level an increase in the target masses in needed: XENONnT, LZ and DarkSide-20k are working in this direction, towards better sensitivities detectors.

Chapter 2

Argon

Liquefied noble gases have been considered extremely promising in the last thirty years for dark matter direct search. First of all they can be used to build large mass detectors: this feature is crucial to maximize the active volume because of the small expected WIMP cross section. Noble liquids have excellent ionization and scintillation properties, for example, as we will see in detail in this chapter, in liquid argon a particle can produce $\sim 10^4$ photons per MeV of deposited energy. They are very suitable as target materials also because they are available in large quantities and, in the case of argon, the cost is not very high. Another important requirement for dark matter experiments is the extremely low background level needed and noble gases can be easily purified from radioactive impurities. Moreover using these materials allows to drift and collect electrons released in the ionization process, or alternatively extract them in gas phase and create a secondary scintillation signal. This last property has fundamental relapse because, by simultaneously measuring ionization and scintillation signals, it is possible to obtain information on the primary incident particle.
In this chapter I will analyse only the properties of argon, leaving out xenon, as all the detectors of the DarkSide project use this active medium. I am going to describe the main response properties of argon in order to understand in detail the working principle of a dual-phase Time Projection Chamber (TPC) for the research of dark matter. I will give particular attention to the mechanisms of microphysics - typical of argon - that allow, through the study of the temporal shape of the signals, to discriminate between nuclear recoil and electronic recoil events, and therefore between hypothetical WIMP events and background. Finally, I will briefly summarize what has always been considered, until recent years, the weak point of the use of liquid argon, namely the presence of the ^{39}Ar radioactive isotope and in particular I will focus on how the DarkSide collaboration solved this problem.

Parameter	**Value**
Z	18
A	40
Boiling point at 1 atm	87.3 K
Liquid density at 87.3 K	1399 kg m^{-3}
Gas density at 273 K, 1 atm	1.761 kg m^{-3}
Liquid dielectric rigidity	100 kV/cm
GAr dielectric constant, ε_g	1
LAr dielectric constant, ε_l	1.5
Electron mobility, μ_l	$\approx$ 500 $cm^2s^{-1}V^{-1}$
$W'_{g,\beta}$	26.4 eV
$W'_{l,\beta}$	23.6 eV
First ionization potential, I	15.7 eV
Liquid argon energy gap, E_g	14.2 eV
Rayleigh scattering length, λ_0	90.0 cm
Scintillation light wavelenght	128 nm

Table 2.1 Argon basic propreties. See Ref. [15] for more details.

2.1 Particle interactions in liquid argon

The process of energy loss in argon is quite complex and depends on numerous different conditions. The released energy can ionize or excite atoms, generating electrical charge or a light signal respectively. Furthermore, part of the ionization charge undergoes a recombination process, during which further scintillation light is emitted. Finally, a fraction of energy is dispersed in the form of heat and is usually not measured. In this section and in the following we will examine the mechanisms mentioned in detail, trying to highlight the interdependencies between them.

Starting from the most general case possible a particle that interacts in liquid argon gives a certain amount of energy to the atoms of the medium. According to Lindhard's theory this energy can be transferred either to electrons or to nuclei [61]. It is reasonable to consider these two contributions separately because the slow-moving atoms, which are recoiling after a primary interaction, can not excite the electrons, conversely the energy given to the electrons can only return to the atoms slowly. This allows to write the total deposited energy as:

$$E_0 = \bar{\nu} + \bar{\eta} \tag{2.1}$$

where $\bar{\nu}$ is the mean energy spent in nuclear collisions and $\bar{\eta}$ is the mean energy given to the electrons. The energy given to argon nuclei will be either transferred to other nuclei, generating a sort of cascade of nuclear recoils, or will be dissipated as heat. What is usually considered for signal formation in noble liquid detectors is the electronic fraction of the deposited energy that can divided into three different contributions, corresponding to three different physical mechanisms [15]. In particular, energy can be spent in ionization, or to excite an atom or to energize free electrons. The combination of these three effects can be parametrized as follows:

$$\bar{\eta} = N_i \bar{E}_i + N_{ex} \bar{E}_{ex} + N_i \bar{\varepsilon}_{se} \tag{2.2}$$

with N_i the number of ion-electrons pairs produced, $\bar{E}_i$ the mean energy spent for each couple; N_{ex} is the number of excited atoms with mean energy $\bar{E}_{ex}$ and $\bar{\varepsilon}_{se}$ is the sub-excitation electrons energy that goes into heat because it is lower than the excitation potential. Usually, in the case of argon gas, all the energies are normalized with respect to the ionization potential (I = 15.75 eV). However, liquid argon shows a band structure of the electronic states, more similar to that of a solid, whereby the ionization potential loses its meaning. So the energies are referred to the energy of the band gap E_g and equation 2.2 can be rewritten as:

$$\frac{\bar{\eta}}{E_g} = N_i \frac{\bar{E}_i}{E_g} + N_{ex} \frac{\bar{E}_{ex}}{E_g} + N_i \frac{\bar{\varepsilon}_{se}}{E_g} \tag{2.3}$$

with $E_g = 14.2/eV$ for liquid argon. This equation can be used to make a balance at the end of ionization processes, but before recombination begins. In general the ratio between excited atoms and ion is assumed to be ~ 0.2 for electron recoils and ~ 1 for nuclear recoils. But it is important to remind that especially in a condensed medium, recombination plays a very important role in understanding the response to the various possible incident particles. In particular, the measured ionization and scintillation signals are not the same as those expected on the basis of the values of N_i and N_{ex}; they also strongly depend on the eventual electric field.

2.1.1 Ionization and recombination

The ionization process consists in the formation of free electrons and positive ions Ar^+; as already mentioned it is useful to borrow the solid state physics framework referring to positive ions as "holes". These holes form immediately - in times of the order of picoseconds - molecular ions Ar_2^+. The electrons, on the other hand, lose their kinetic energy both through inelastic collisions, generating further ionizations and excitations, and through elastic collisions with atoms, which give rise to phonons.

In general, to characterize the ionization process we use the average energy spent to generate an ion-electron pair, however around this definition is often generated confusion, because it

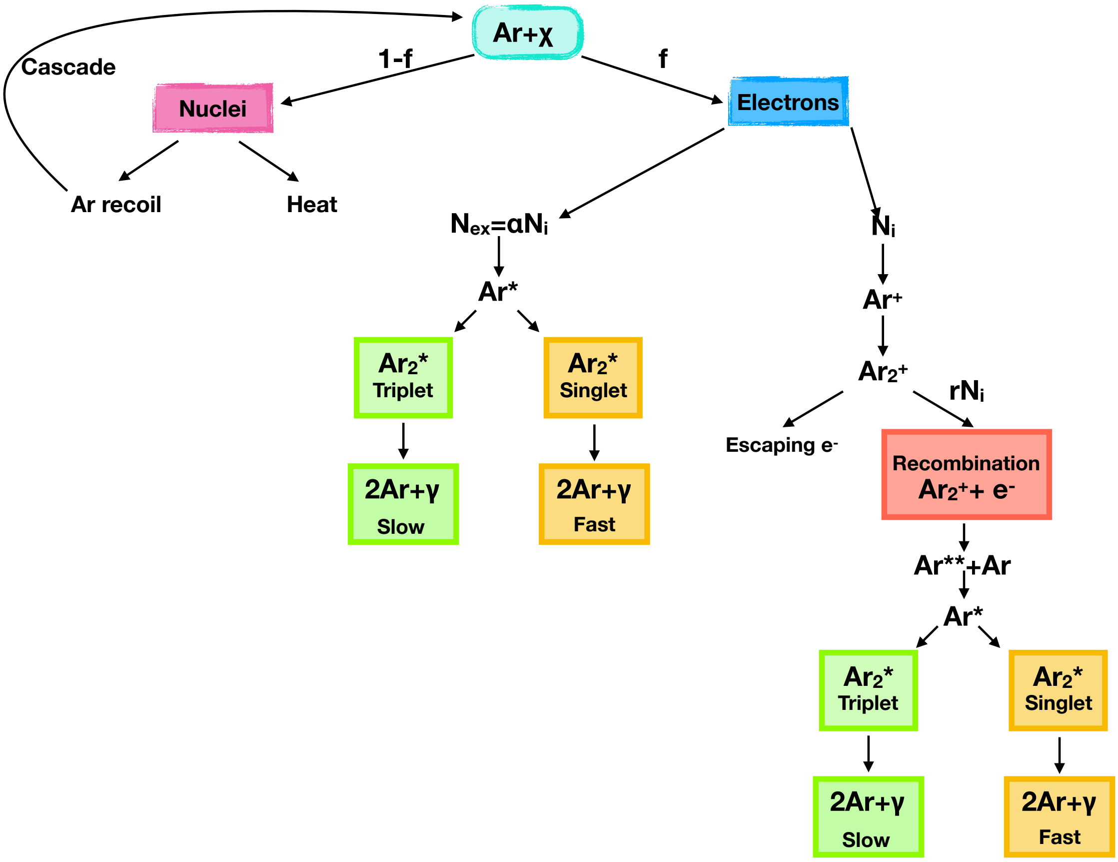

Fig. 2.1 Scheme of the interaction processes in liquid argon. When an hypothetical WIMP χ scatters in liquid argon, it originates a nuclear recoil. The recoiling nucleus looses a fraction f of its energy through electronic collisions, the remaining part is given to other nuclei. The energy given to the electrons can generate both ionization and excitation. Excited atoms can form excimers and the produce scintillation light; on the other hand the free electrons can either escape or undergo to recombination.

can depend on the class of particles considered. In particular we define

$$W(E_0) = \frac{E_0}{N_i} \tag{2.4}$$

the ratio between the total deposited energy and the number of pairs produced; instead

$$W' = \frac{\bar{\eta}}{N_i} \tag{2.5}$$

is the ratio between the energy given to electrons and the number of pairs produced. The confusion comes from the fact that for relativistic particles $E_0 \sim \bar{\eta}$, almost all the deposited energy goes to electrons, so $W_\beta \sim W'_\beta$; on the contrary in case of slow ions which generate nuclear recoils the two variables assume different values, so you have $W_{NR} = W'_{NR}(\bar{\nu}+\bar{\eta})/\bar{\eta}$. It is a reasonable approximation to suppose that $W'_\beta = W'_{NR}$ = 23.6 eV in liquid: this means that the average energy spent to create an electron-ion pair does not depend on the kind of primary particle which interacts with the argon atoms, although the energy loss is strongly correlated to the particle type. In other words, the different number of pairs generated by slow ions and relativistic particles depends only on the different fraction of energy given to the electrons.

These parameters are useful to describe ionization, but from an experimental point of view they are not very practical because it is extremely challenging to perform absolute charge measurements. The main problem is that the electric charge collected with an electrode (or in any case proportionally measured) is never identical to that initially produced by the primary interaction. This is due to the presence of electronegative impurities which absorb electrons, but above all it is caused by the recombination phenomenon, which can not be eliminated because it occurs at any finite value of an electric field.

Recombination is a highly articulated mechanism, studied since the beginning of the twentieth century by George Jaffé [62]. It basically depends on two conditions:

- the kind of particle that caused the ionization and also the kinematic conditions, because these two aspects determine the initial distribution of ions and electrons;
- the strength of the electric field applied.

There are also other aspects to be taken into account such as mobility inside the liquid, the diffusion rate and the distance travelled by the electrons before they reach the thermal equilibrium with argon. It is possible to identify two classes of recombination models: those based on the so-called geminate theory and those based on the columnar theory.

The geminate theory of recombination, first introduced by Onsager, is based on the assumption that each electron-ion pair is independent of the others and that therefore an electron can recombine only and exclusively with its parent ion [63]. In this framework, if the we consider a low electric field, the collected charge can be written as:

$$\mathcal{Q}(\mathcal{E}_d) = \mathcal{Q}_0 \left(1 + \frac{\mathcal{E}_d}{\mathcal{E}_{kT}}\right) e^{-\frac{r_c}{r_0}} \qquad if \qquad \mathcal{E}_d \ll \mathcal{E}_{kT} \tag{2.6}$$

with $\mathcal{E}_d$ the applied drift field, $\mathcal{E}_{kT} = 2\varepsilon k^2 T^2/e^3$, r_0 the thermalization length and $r_c = e^2/\varepsilon_r kT$ the so-called Onsager radius. This radius is the distance between a ion and a electron for which the thermal energy of the electron is equal to the electrostatic potential energy; for liquid argon we have $r_c = 80$ nm. Even with very low fields, of the order of less than 1 kV/cm, Eq. 2.6 does not reproduce the data. The main problem is that in liquid argon you have induced dipoles near the ions, so assuming an infinite range Coulomb attraction does not give a good description of the real status of the system. On the other side, the columnar model, initially formulated by Jaffé and then refined by Thomas and Imel, hypothesizes a distribution of charges in a sort of column around the particle trace, where the electrons can recombine with any ion [64]. It is very difficult in this context to elaborate a single theory of recombination because the primary charge distribution - often called track structure - strongly depends on the type of particle and different dE/dx. In general the volume around the track is divided into two regions: the innermost, called *core*, is usually cylindrically symmetric and has the greater energy density, the outer one consisting of the δ-rays, is called *penumbra* and has lower energy density. For high energy particles the columnar model works quite well. In particular for 1 MeV electrons one can imagine a cylinder in which the average distance between two ions is of the order of the Onsager radius (r_c) and, as between two atoms there are $\sim$ 4 nm, these two ions are separated by hundreds of neutral argon atoms. So if the electrons are inside the sphere defined by the Onsager radius it dominates the Coulomb attraction, otherwise the thermal agitation takes them away from the ions. As the thermalization length for an electron in liquid argon is ~ 1.7 μm, much larger than r_c, a large number of electrons thermalize too far from the ions to recombine. In this case, in the absence of an electric field, they are usually called "escaping electrons", vice versa in the presence of an external field such electrons will be drifted away. In the case of α-particles and fast heavy ions the escaping electrons are almost absent, due to the higher ionization density which is estimated $\sim 10^{-2}$ nm^{-3}, compared to typical values in the case of 1 MeV electrons, that are about $\sim 2 \cdot 10^{-7}$ nm^{-3}. The electrons being trapped in a volume where the positive ions are very close together, recombine in a extremely short time, less than 1 ps, well before reaching the thermal equilibrium.

For low energy β/γ events the track shape is not cylindrical, but it resembles a sort of sphere. Thomas and Imel proposed the so-called box model, assuming a uniform charge distribution

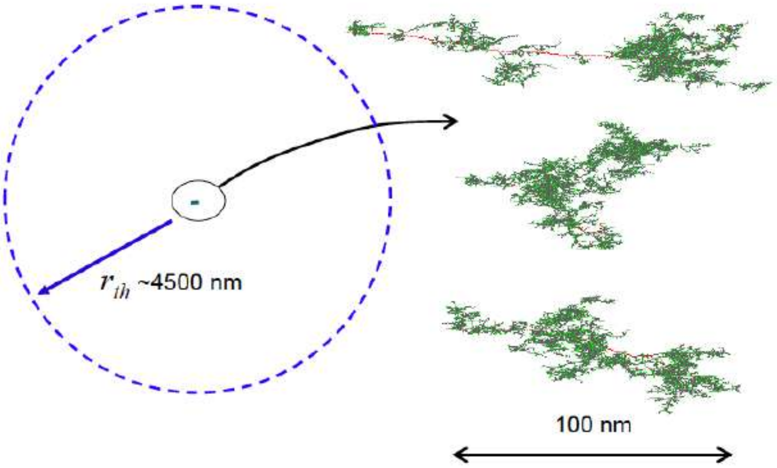

Fig. 2.2 Nuclear recoil tracks simulated with the TRIM software, compared to the thermalization distance [**?**].

in a volume of side a, whose dependence on the drift electric field was parameterized as:

$$\mathcal{Q}(\mathcal{E}_d) = \frac{\mathcal{Q}_0}{\xi} ln(1+\frac{1}{\xi}) \tag{2.7}$$

where ξ is a free parameter to be extracted from the fit of data, that depends from the field as follows:

$$\xi = \frac{N_0 \alpha}{4a^2 \mu \mathcal{E}_d} \tag{2.8}$$

with N_0 the initial number of electrons, α the recombination coefficient and μ the electron mobility. Later this model was improved introducing two distinct parameters, ξ_0 and ξ_1, to take into account the fact that along the track the dE/dx increases, thus increasing to also the ionization density.

Finally, for what concerns nuclear recoils it is crucial to consider that a fraction of the energy deposited is lost in nuclear collisions ($\bar{\nu}$), this process is sometimes called nuclear quenching. In order to hypothesize a track structure it is necessary to consider this phenomenon. Furthermore, the primary recoil event can transfer a high fraction of its kinetic energy by striking atoms of the same species. This means that, as already mentioned before, a sort of cascade of secondary recoils of comparable energy is generated, where it is no longer possible to identify the original projectile. The topology of the trace, also in this case, is not cylindrical, but a very complicated structure with various ramifications, in which it is not easy to identify a dimension much greater than the others. When comparing the size of the cascade with the length of thermalization, there is a factor ~ 40 difference (See Fig. 2.2). The electrons can be distributed in a volume that is approximately constant, so in the case of low-energy recoils I have less charge in a constant volume, therefore less density and consequently less recombination.

2.1.2 Scintillation

Liquid argon is a natural scintillator that under certain conditions emits vacuum ultra violet (VUV) photons with $\lambda = 128$ nm. What we usually call scintillation is closely connected to the recombination process discussed in the previous section, in fact after an ion-electron pair has recombined it causes the emission of light. Therefore the overall scintillation light that can be observed in liquid argon is the sum of two components, coming from two distinct processes:

- excitation luminescence, due to the primary excitation of argon atoms;
- recombination luminescence, originated by the formation of an excited state after recombination.

More precisely, as we will see in the following, in both cases a photon is emitted by the de-excitation of the same argon excimer, that is an unstable argon excited molecule. What differentiates the two contributions is the formation process of the excimer itself.

Excitation luminescence When a particle, for example an electron, impacts with an argon atom some of the deposited energy goes to the atomic electrons generating a excited atom, denoted as Ar^*. The excited atom has one valence electron promoted to the next higher orbital: this favours the dimerization with a ground state atom. They form a strongly bounded molecule, $Ar_2^{*,v}$, which initially is in a vibrational excited state, that becomes a pure electronic excited state, Ar_2^*, through non radiative mechanisms. Finally the excimer emits a scintillation VUV photon decaying to the ground state and the molecule is dissociated. The formation of the $Ar_2^{*,v}$ and its light emission is a very fast process, which takes order of picoseconds, and it is often called exciton self-trapping. All the steps are summarized as follows:

$$\begin{aligned}
&Ar + e^- \to Ar^* + e^- && \textit{primary excitation}\\
&Ar^* + Ar \to Ar_2^{*,v} && \textit{excimer formation}\\
&Ar_2^{*,v} + Ar \to Ar_2^* + Ar && \textit{relaxation}\\
&Ar_2^* \to Ar + Ar + h\nu && \textit{VUV emission}
\end{aligned} \tag{2.9}$$

Recombination luminescence The alternative luminescence mechanism starts when an argon ion binds with a neutral argon atom in the ground state, forming a molecular ion denoted as Ar_2^+. Then a free electron - previously produced by ionization - recombines with the positive ion causing the split of the molecule. What you obtain is one neutral argon in the ground state and a doubly excited atom (Ar^{**}). At this point the Ar^{**} dissipates some energy in heat and becomes a single excited atom that undergoes the exciton self-trapping described above. Here the whole process:

$$\begin{aligned} & Ar + e^- \rightarrow Ar^+ + 2e^- && \textit{ionization} \\ & Ar^+ + Ar + Ar \rightarrow Ar_2^+ + Ar && \\ & e^- + Ar_2^+ \rightarrow Ar^{**} + Ar && \textit{recombination} \\ & Ar^{**} + Ar \rightarrow Ar^* + Ar + heat && \\ & Ar^* + Ar + Ar \rightarrow Ar_2^* + Ar + heat && \\ & Ar_2^* \rightarrow Ar + Ar + h\nu && \textit{VUV emission} \end{aligned} \tag{2.10}$$

In both cases the atomic de-excitation of argon is disfavoured: in average the Ar^* forms the excimer before emitting any photon. The relative contribution of these two emission channels has been studied by applying electric fields of varying intensity. If the primary interaction is due to an electron, applying an electric field of 10 kV/cm allows to collect about 100% of the ionization charge. In this case the scintillation yield is reduced by a factor of 3; which means that about 1/3 of the light is produced via direct excitation, while the remaining 2/3 are caused by recombination. It is important to underline that in the case of heavy particles interactions, which then generate high ionization density tracks, an electric field of 10 kV/cm allows to extract only a few percent of the charge produced. So in this case it is not possible to make a measurement of the excitation light only.

Both these two scintillation processes are affected by competing mechanisms which lead to a light reduction, referred to as electronic quenching. Indeed there are three possible reactions that allow argon excitons to decay non-radiatively: bi-excitonic quenching, photo-ionization, and the Penning process. Respectively:

$$\begin{aligned} & Ar^* + Ar^* \rightarrow Ar + Ar^+ + e^- && \textit{Bi-excitonic collisions} \\ & Ar^* + Ar_2^* \rightarrow Ar + Ar_2^+ + e^- && \textit{Photo-ionization} \\ & Ar_2^* + Ar_2^* \rightarrow 2Ar + Ar_2^+ + e^- && \textit{Penning process} \end{aligned} \tag{2.11}$$

These phenomena are mainly due to the high exciton density, so they are more effective on particles with high stopping power. When discussing scintillation signal intensity, it is therefore useful to use units of keV "electron equivalent", denoted as keV$_{ee}$, which express the energy an electron would need to have to produce the same amount of scintillation light.

The 128 nm scintillation photons (that correspond to $\sim$ 9.7 eV) produced by these processes are originated from two nearly degenerate excimer states. They are spectroscopically indistinguishable, but they have different decay times. In particular the excimer Ar_2^* is in a Rydberg state, which means that it can be roughly schematized as a spin 1/2 core around which there is a bound electron, so the possible states are the following four. We can identify a long-lived triplet state and a short-lived singlet state:

$$\left.\begin{array}{l} |\uparrow\uparrow\rangle \\ \frac{1}{\sqrt{2}}|\uparrow\downarrow\rangle + |\downarrow\uparrow\rangle \\ |\downarrow\downarrow\rangle \end{array}\right\} triplet \tag{2.12}$$

$$\left.\frac{1}{\sqrt{2}}|\uparrow\downarrow\rangle - |\downarrow\uparrow\rangle\right\} singlet \tag{2.13}$$

The final state has total spin equal to 0, so the singlet state can perform a direct transition (allowed by selection rules) in a very short time of the order of $\tau_s \sim 6$ ns; on the contrary the triplet state transition is forbidden because it would go from a spin 1 state to a spin 0 state. However this becomes possible because of spin-orbital coupling between different states, but it implies a longer life-time of $\tau_t \sim 1.5\ \mu$s. The time constants of these states do not vary depending on the particle type that generated the interaction, as it can be seen in figure 2.3, but the relative contribution of the triplet slow component and the singlet fast component depends strongly on the energy loss density. It has been observed that the increase of the singlet fraction is correlated with dE/dx, so high ionization density events have more singlet component and consequently generate faster scintillation signals. The causes of this phenomenon are not yet clear. A possible explanation, given by Ref. [65], is that singlet to triplet transitions can occur, induced by super elastic collisions with thermal electrons. These collisions would be more likely in the case of electrons, compared to heavy particles, simply because they have more time to take place because of the slower recombination. This feature is crucial, as we will see, to make an analysis of the signals in time that allows to discriminate electronic recoil events from nuclear recoil events, through the so-called Pulse Shape Discrimination (PSD).

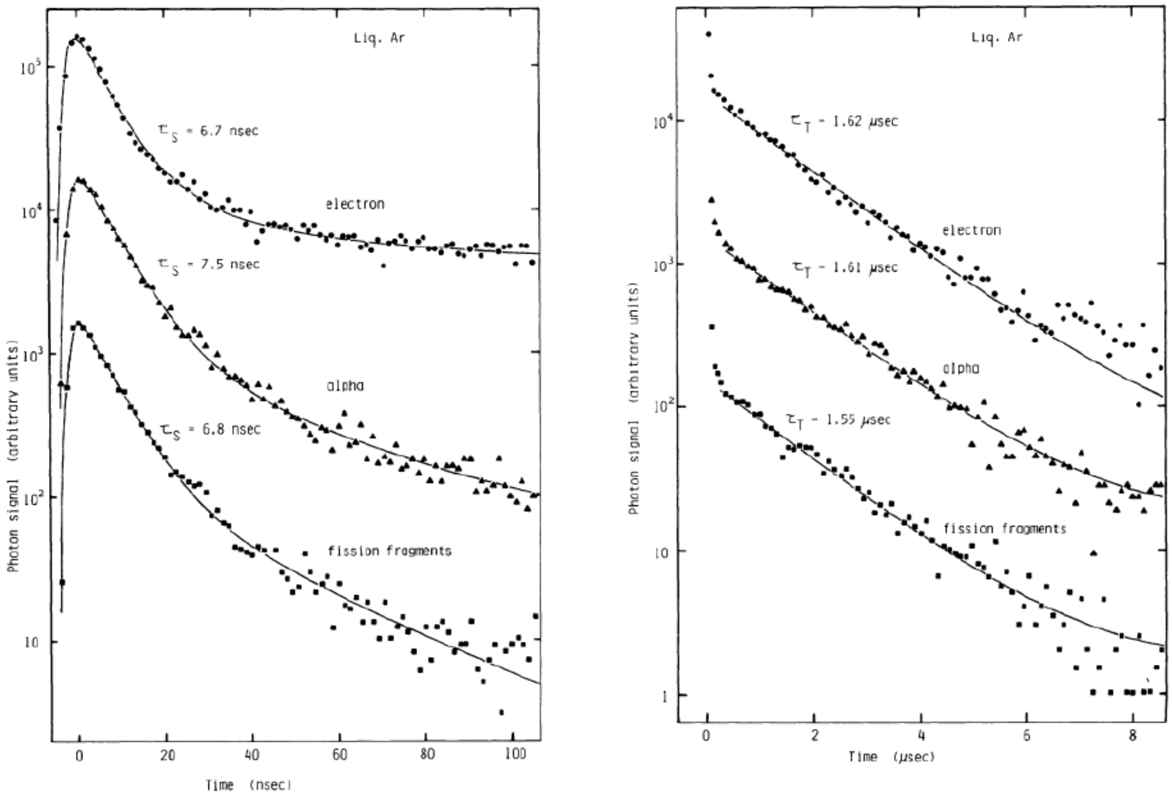

Fig. 2.3 Singlet (left plot) and triplet (right plot) decay times for electrons, alpha particles and fission fragments in liquid argon [65].

Particle	τ_s **(ns)**	τ_t **(ns)**	I_s/I_t
Relativistic e^-	6	1590	0.3
α	7.1	1660	1.3
FF	6.8	1550	3

Table 2.2 Argon time constants for singlet and triplet components for different particles: electrons, alpha particles and fissions fragments.

2.1.3 Propagation of the signals

We have therefore seen that a particle which deposits energy in liquid argon generates two different measurable physical signals: scintillation light, due to excited atoms and recombination of ionized atoms, and ionization charge that escapes recombination. In order to carry out measurements of these two quantities it is necessary to take into account the propagation of both the light and the electric charge in the medium.

Light - The first crucial observation is that liquid argon is extremely transparent to its own scintillation light. As we have seen in the previous sections, VUV photons are emitted by the Ar_2^* excited dimer, so the photon frequency depends on the molecular orbitals structure. The emitted photon can not be reabsorbed because it has less energy than the excitation energy, due to a Stokes' shift. As shown in Eq. 2.9 a fraction of energy is lost because of vibrational relaxation. Assuming therefore that the light produced can travel through liquid argon, we need to analyze what it hinders the propagation, giving rise to a finite attenuation length. Absorption due to impurities and Rayleigh scattering iare the processes that intervene: the first leads to a reduction in the number of photons, the second is elastic diffusion. The total length attenuation length can be written as follows, considering that the absorption length L_A, is much larger than the scattering one:

$$\frac{1}{L} = \frac{1}{L_S} + \frac{1}{L_A} \qquad \Longrightarrow L \sim L_S \tag{2.14}$$

From experiments in liquid argon we have a scattering length of L_S =66 cm.

Charge - To collect ionization charge several conditions need to be satisfied by the carriers:

- they have to avoid recombination;
- they need to have high mobility;
- they do not have to generate low mobility systems along their path;
- they need to be amplified in order to have a measurable signal.

Electrons have high mobility in liquid argon (μ_l = 500 cm^2 s^{-1} V^{-1}) so they can be drifted efficiently, while ions are a factor 10^5 slower, so they are usually not collected. The real problem are the electronegative impurities, like water and oxygen that are the most common. It is therefore necessary to have a very pure gas to liquefy, but it is also necessary to purify it further with the use of getters. It is also very important to keep under control the cleanliness of all the parts of the detector: both selecting the proper materials and handling carefully the components. To quantify the purity of the liquid it is used a parameter called electron lifetime (τ_l), that corresponds to the time necessary for the number of electrons to be reduced by a factor 1/e. Solving the capture process equations you obtain:

$$N_e(t) = N_e(0)e^{-\frac{t}{\tau_l}} \tag{2.15}$$

The life time is related to the number of impurities N_{imp} and to the electron capture reaction rate K_{imp}, so $\tau_l = (\sum_{imp} N_{imp} K_{imp})^{-1}$ summing on all the impurity types. Today it is not difficult to reach an electron lifetime of $\sim$ 1 ms, that corresponds to drift lengths greater than one meter. It is also very important to keep under control the cleanliness of all the parts of the detector: both selecting the proper materials and handling carefully the components.

2.2 Dual-phase Time Projection Chamber

In this section I will present the general working principle of a biphasic argon Time Projection Chamber (TPC), using as reference the DarkSide-50 detector, described in section 3.1. The dual phase liquid TPC technology allows to measure both the scintillation light and the ionization charge at the same time, improving energy resolution and also giving rise to a further discrimination parameter in addition to the pulse shape discrimination of the signal. As we will see in the following the physical quantity that is measured is light in both cases, so the TPC is equipped with photosensors to measure both the signal produced in the liquid and the one generated in the gas.

In general, a double phase TPC consists of a volume of liquid above which there is a thin layer of the same element, but in the gaseous phase, the so-called gas pocket. Usually at the top and at the bottom there are two conductive planes, kept to potential and used respectively as anode and cathode. Just below the interface surface between liquid and gas there is a metal grid, also kept at fixed voltage. See a sketch of the essentials components of DarkSide-50 TPC in figure 2.4. Between the cathode and the grid it is generated the so-called drift electric field, that rips off the ionized electrons. To guarantee the drift field uniformity there is a metal field cage all around the TPC volume. Between the grid and the anode there is another potential difference, that gives rise to two electric fields, one in liquid and one in gas, of different intensity due to the different dielectric constants in the two phases. The field present in the liquid above the grid is called the extraction field, because it allows the drifted electrons to pass into the gaseous phase. The field in the gas pocket, on the other hand, is

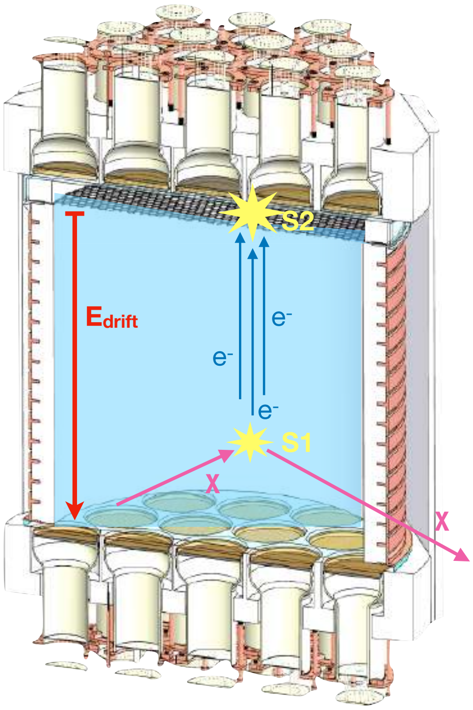

Fig. 2.4 DarkSide-50 double phase argon Time Projection Chamber (TPC) scheme. The detector is filled of liquid argon up to just above the metal grid, the rest of the volume is filled with argon gas.

called electroluminescence field or, sometimes, a multiplication field (see Fig. 2.5). Let's now look at these two processes in more detail.

The scintillation signal produced in liquid - from now on we will call it S1 - is proportional to the number of photons and it depends both on the number of excited atoms and recombined ions (see Sec. 2.1.2) as follows:

$$S1 \propto N_{ph} = N_{ex} + rN_i \tag{2.16}$$

where r is the charge recombination fraction. The electrons that escape the recombination are drifted through the liquid up to the grid; at this point they are extracted from liquid to gas. This transition is energetically disadvantaged, but some electrons in the tail of the velocity distribution can overcome the barrier, if there is even a weak electric field forcing them to

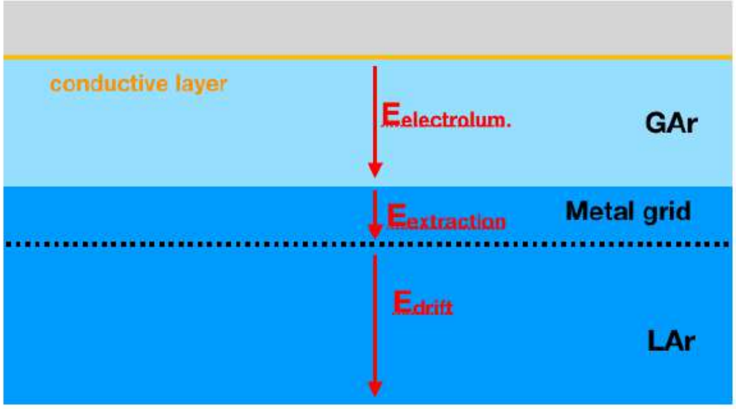

Fig. 2.5 Electric fields configuration. Between the grid and the cathode, which is not shown in the sketch, there is the drift field. In the liquid layer above the grid there is the extraction field, that rips of the electrons from the interface between liquid and vapour. In the gas phase, because of the different dielectric constant, the field changes and it is called of electroluminescence; this is the field which cause the discharge that causes the S2 signal.

approach the surface. As one increases the filed,the mean electron kinetic energy starts to grow and the number of extracted electrons increases. The electrons that pass into the gas can be divided into two categories based on their kinetic energy. Those that cross the potential barrier immediately - because the energy gained from the electric field is much greater than the average thermal energy - are called *hot* electrons. The ones that are backscattered to the liquid at the first attempt are called *thermal* electrons. The fraction of *hot* electrons increases with the field strength: in particular for fields of the order of $2.5 \div 3$ kV/cm all the electrons are *hot* and so have in average enough kinetic energy to be extracted directly. For a detailed model of the electric potentials, with different dependencies from the dielectric constants and the thickness of the interface see Ref. [66, 67].

Once passed in the gas phase the electrons are accelerated by the present field. They can therefore give rise to two different phenomena: ionize other atoms producing an avalanche effect or excite them generating light again. This process of secondary scintillation in gas is called electroluminescence and it allows a strong multiplication because hundreds of photons are generated for each electron extracted. The mechanisms of microscopic interaction in gas are completely analogous to those already described for the liquid in Sec. 2.1.2 and generate photons with $\lambda = 128$ nm. To be precise there is a tiny difference in wavelength because the energy levels of the excitons in liquid are shifted down with respects to the ones in gas. The light signal produced, denoted as S2, can be measured with the same optical sensors used for

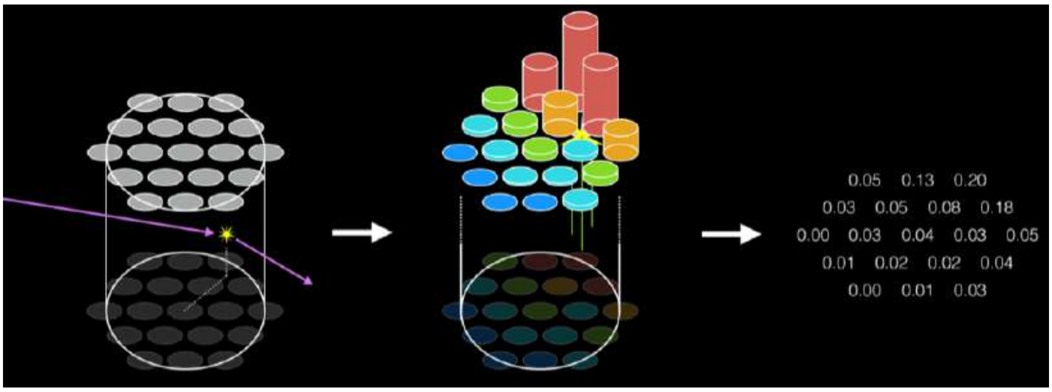

Fig. 2.6 *(x,y)* position reconstruction scheme in DarkSide-50 TPC. The algorithm that is used to find the event position on the horizontal plane is based on the charge fraction collected by each top PMT. Figure from Ref. [8]

the liquid scintillation light. The light yield in gas is a linear function of the pressure and of the electric field. One possible parametrization is the following:

$$\frac{dN_{ph}}{dx} = \alpha E - \beta P - \gamma \tag{2.17}$$

Exploiting the two signals it is possible to perform a 3D position reconstruction. The vertical position, associated to the z coordinate, can be inferred from the time delay between S1 and S2 signals: the time interval between the two signals allows to calculate the drift distance travelled by electrons, knowing their speed in liquid. The horizontal position, in the *(x,y)* plane, is reconstructed from the S2 distribution across the top photosensors that is depicted in figure 2.6. As we have seen, one of the peculiar characteristics of argon is the huge difference in singlet and triplet decay times and the different fraction of these states for electron and nuclear recoils. As show in figure 2.7, the two types of signal can be easily distinguished by looking at their shape in time. To fully exploit this feature and perform af efficient discrimination between background and potential WIMP events, in DarkSide-50 we use the fraction of prompt scintillation light with respect to the total. The parameter, called $f90$, is defined as:

$$f90 = \frac{\int_0^{90ns} S1dt}{\int_0^{t_{end}} S1dt} \tag{2.18}$$

where 0 is the start time of the scintillation signal and t_{end} is the time when S1 is finished. Considering calibration data taken with an americium-berillium (AmBe) neutron source and plotting the $f90$ parameter, as a function of the scintillation signal S1, two populations of events appear (see Fig.2.8). There is an upper band, which corresponds to $f90 \sim 0.7$, due to the neutron scatterings and a lower band made by β/γ events that has mean value around

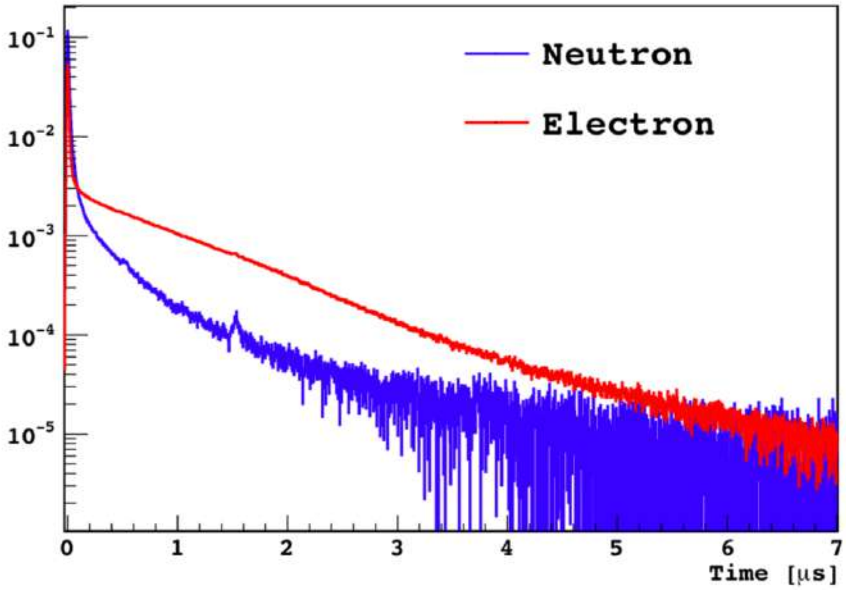

Fig. 2.7 The plot shows electron (red) and nuclear (blue) recoil averaged waveforms in liquid argon, as a function of time. The different shape of the two kind of signals is the basis of the pulse shape discrimination technique for the β/γ background rejection.

0.3. Taking this two distributions as the starting point it is possible to the define a region of interest for the dark matter search, as explained in the following chapter (Chap. 3).

2.3 Underground argon

Argon is the third most abundant gas in the atmosphere following nitrogen and oxygen, in particular it is made of three stable isotopes: ^{40}Ar that is the 99.604%, ^{38}Ar that is 0.063% and ^{36}Ar that is 0.335%. Moreover there is a small amount of ^{39}Ar, an unstable isotope which β-decays with an endpoint energy of 565 keV and has a half-life of 269 years. The presence of this radioactive isotope was one of the reasons why in the past it was often preferred to use xenon as a target for dark matter detectors. The decays occurring in the argon active volume generate events with energy of the order of a hypothetical dark matter signal, but these events can be eliminated through the pulse shape discrimination technique. In addition, if the concentration of ^{39}Ar is excessive, the problem of the pileup emerges: if the rate of ^{39}Ar events is of the order of the maximum drift time, it is likely to trigger on this type of decay.

The DarkSide collaboration has made enormous progress over the past few years to address this issue. The starting point was that it had been measured an ^{39}Ar activity of $\sim$ 1 Bq/kg in

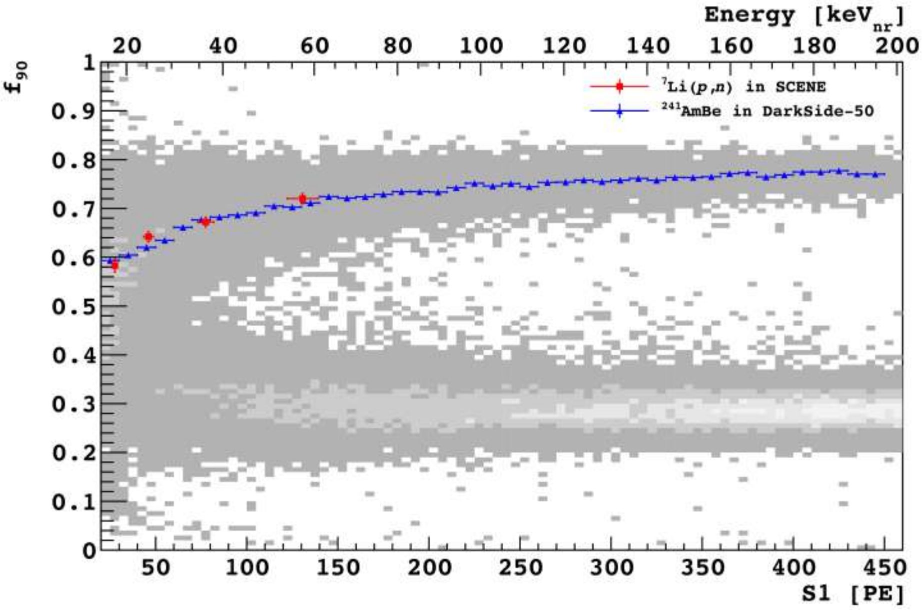

Fig. 2.8 Discrimination parameter, denoted as $f90$, distribution as a function of the scintillation light (S1 signal), obtained in the DarkSide-50 detector during a calibration campaign with an AmBe neutron source. Nuclear recoil events correspond to the population around $f90 = 0.7$, while electron recoil are the lower band around $f90 = 0.3$ [9].

atmospheric argon and from this began a meticulous search to find the most effective way to clean up the argon. The mechanism of production of the isotope is the cosmogenic activation in the upper layers of the atmosphere, through the reaction:

$$^{40}Ar + n \longrightarrow ^{39}Ar + 2n \tag{2.19}$$

so argon extracted from underground sites is expected to be poor in ^{39}Ar, because rocks shield from cosmic rays. However, even underground there is a production channel of the ^{39}Ar by neutron capture on potassium. In particular neutrons produced in the uranium and thorium decay chains can undergo the ^{39}K(n,p)^{39}Ar reaction generating ^{39}Ar. The content of this isotope depends on the neutron flux underground, so it is important to find a place with very low uranium and thorium concentrations, because they can induce n with (α, n) reactions. Earth's mantle has ppb levels, in fact the deep deposits of gas have a quantity of ^{39}Ar about 1000 times lower than those in the crust. The DarkSide collaboration found a possible site in the Kinder Morgan Doe Canyon mine in Cortez, Colorado. Between 2013 and 2015 about 156 kg of underground argon (UAr) were extracted and sent to Fermilab for further purifications procedures based on isotopical distillation. In April 2015, the DarkSide-50 time

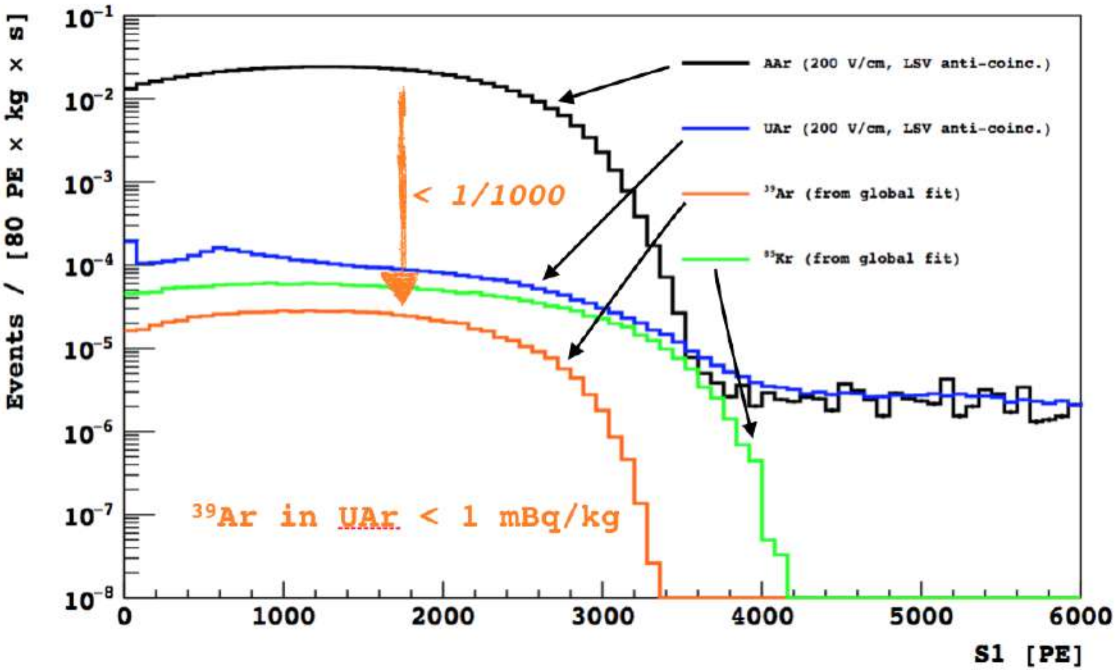

Fig. 2.9 Reduction of ^{39}Ar in underground argon: the black line corresponds to the data collected with atmospheric argon, that has to be compared with the blue line obtained with the underground argon. The green and the orange lines are respectively the ^{85}Kr and the ^{39}Ar components extracted from the global fit to spectrum, see Ref. [10] for details.

projection chamber was filled with ultra-pure underground argon and, as shown in figure 2.9, the ^{39}Ar concentration was measured to be lower than atmospheric argon by a factor $(1.4 \pm 0.2) \times 10^3$ [10].

For the future, the collaboration has developed a broader strategy to increase the production of UAr, to procure the target required for the next detector DarkSide-20k (see Sec.3.2).

Chapter 3

The DarkSide project

DarkSide is an extensive dark matter direct search program that is focused on a staged series of experiments based on liquid argon, but also includes accessory projects for the development and optimization of the new technologies necessary to improve the performance of the detectors used. All the DarkSide experiments are, or will be, housed at Laboratori Nazionali del Gran Sasso (LNGS), in Italy.

From 2011 to 2013 preliminary studies were made on a small technical prototype, called DarkSide-10, which was then replaced by the detector currently installed at LNGS, called DarkSide-50; during the next years the new DarkSide-20k detector will be built and assembled. The number in the names of the different experiments indicates approximately the liquid argon mass used, expressed in kilograms.

Among the variety of detector technologies, the detection properties of liquid argon Time Projection Chambers (TPCs) are significant for direct dark matter searches. In particular operating the detector in dual phase mode, collecting both the scintillation light and the ionization electrons produced, allows a powerful discrimination against background (see Sec. 2.2).

The first half of this chapter is dedicated to DarkSide-50, I will describe the three detectors that compose it and briefly present the last results obtained. Later I will focus on the design of DarkSide-20k emphasizing continuity and differences with respect to the previous detector. I will only mention projects parallel to DarkSide-20k, dedicated to the extraction and purification of the argon (Urania and Aria) and to the optimization and production of the photosensors (NOA-Nuova Officina Assergi).

The ReD-Recoil Directionality experiment, which is a DarkSide R&D project devoted to investigate liquid argon sensitivity to directionality, will be described in detail in chapters 4 and 5.

3.1 DarkSide-50

The DarkSide-50 experiment is located at Laboratori Nazionali del Gran Sasso (LNGS) in Italy, underground at a depth of 3400 m.w.e.. Its apparatus consists of three nested detectors (Fig. 3.1) that from the center outward are: the dual-phase argon Time Projection Chamber (TPC), the Liquid Scintillator Veto (LSV) and the Water Cherenkov Veto (WCV). The TPC is the heart of DarkSide-50 and, containing the active target, it is the dark matter detector. The TPC is surrounded by two additional detectors devoted to the background active tagging. The LSV is a sphere of boron-doped scintillator, designed to detect radiogenic and cosmogenic neutrons; the WCV is used as passive shielding and to tag cosmic muons. The LSV and the WCV are the outer detectors and together they form the so-called veto system. Both the two veto detectors work in anti-coincidence with respect to the TPC, so if there is a coincidence the event is discarded.

As explained in section 2.3 the DarkSide collaboration solved the ^{39}Ar issue using ultra pure argon from deep underground sources and this was done using the DarkSide-50 TPC. Recently DarkSide-50 has demonstrated an extraordinary background rejection capability exploiting both a unique pulse shape discrimination technique and excellent 3D positional resolution for fiducialization, based on the measurement of direct scintillation light together with the electroluminescence signal produced in the gas phase. Although its sensitivity is not competitive with that of the current liquid xenon experiments, these recent results open the way for DarkSide-20k, the new detector under construction that will have a mass greater than 20 tons.

3.1.1 TPC

The general working principle of a dual-phase time projection chamber are described in section 2.2. The core of the whole experiment is a dual phase TPC, placed in a stainless steel cryostat filled with $\sim$ 150 kg of liquid argon.

The TPC itself consists of a cylindrical teflon (PTFE) structure that encloses an argon active volume of height 36.5 cm and diameter 36.5 cm, that corresponds to $\sim$ 50 kg. The PTFE of the cylinder is a reflecting material to prevent light leakage. The light generated is detected through Hamamatsu R11065 3" low-background, high-quantum-efficiency photomultiplier tubes (PMTs): 19 are arranged below the lower face and 19 above the upper face of the cylinder. Between the active volume and the photosensors there are two transparent fused-silica windows. Since the PMTs are not sensitive to the VUV light emitted by the argon, the presence of a wavelength shifter is necessary. The internal surfaces of the walls and windows are coated with tetraphenyl butadiene (TPB): a material that absorbs photons of 128

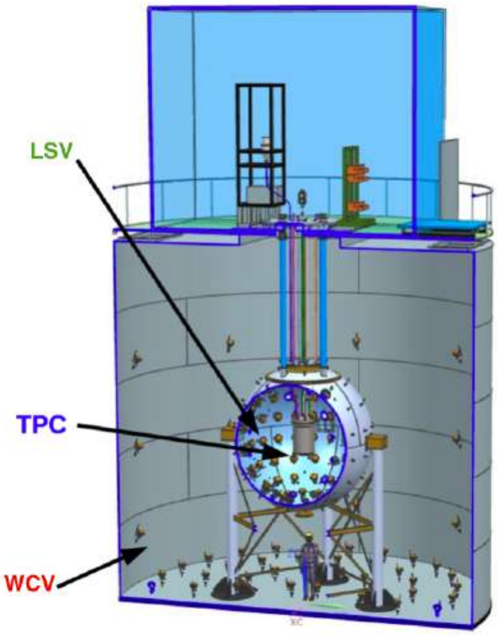

Fig. 3.1 DarkSide-50 nested apparatus: the outer most cylinder is the muon Cherenkov detector (WCV), that contains a stainless steel sphere filled with boron-loaded scintillator to detect neutrons (LSV). The inner grey cylinder is the cryostat that houses the dual phase liquid argon TPC.

nm and re-emits them in the visible spectrum, with a peak around 420 nm. In addition the windows are coated on both faces with a conductive material which allows to hold them at high voltage, constituting the cathode and anode. So, to be precise, the fused silica is covered with a transparent indium tin oxide (ITO) film, that is 15 nm thick; on the top of this film, only on the inner face it is evaporated the TPB. The thickness of the TPB layer depends on the position: on the windows it is thicker at the center and thinner at the edges, on the walls instead it is thinner at halfheight. The top window it is not just a disk like the bottom one, but it as a rim which extends downwards crating what we call the "diving bell". It is a sort of cap that has the purpose of containing the argon gas, thus allowing the creation of a thin ($\sim$1 cm) layer of vapour, the so-called gas pocket. To generate the gas there is a bubbler outside the active volume that boils the liquid argon and keeps the thickness of the gas layer under control through a level meter. Inside the TPC there are three vertical electric fields, generated by three electrodes: the cathode and the anode are respectively the bottom and the top window ITO layer, moreover a few millimeters below the liquid surface is positioned a stainless steel grid held to potential. The field between the cathode and the grid is the drift one, to bring electrons up to the liquid-gas interface and it is maintained uniform by a copper field cage surrounding the active volume. During normal data taking the grid id kept at -5.6

Fig. 3.2 DarkSide-50 time projection chamber seen from the bottom. The cold pre-amplifiers attached to the bottom PMTs can be clearly seen in the foreground. Furthermore, the teflon structure and the copper field cahege are visible.

kV and the cathode at -12.7 kV, creating a 200 V/cm drift field. Thanks to the different dielectric constants of the liquid and gaseous phases, between the grid and the anode - which is usually grounded - two different fields are created. In the liquid layer above the grid there is the electron extraction field, equal to 2.8 kV/cm. Between the surface of the liquid and the anode, in the gas pocket, there is the electroluminescence field, equal to 4.2 kV/cm. The maximum drift time is 373 μs, and the measured value of the drift speed is (0.93 ±0.01) mm/μs [9].
The measured light yield is (7.9±0.4) PE/keV at null electric field and (7.0±0.3) PE/keV at 200V/cm of drift field. The energy resolution measured at 41.5 keV$_{ee}$ (from ^{83m}Kr) is 7%.

3.1.2 Veto system

Trying to minimize backgrounds in a dark matter search experiment is of crucial importance, since possible WIMP interactions are extremely rare. Backgrounds can be divided in two categories: internal or external. The first type of events are generated in the detector itself, in particular they are caused by radioactive contaminants in the various components. The second type of background comes from the environment, for example radioactivity in the laboratory or cosmogenic particles coming from atmosphere. The latter is reduced placing

the apparatus in a underground laboratory, in this case the LNGS.
A different way of classifying backgrounds is distinguishing between electron and nuclear recoils. As explained before (see Sec.2.2), electron recoils can be rejected effectively using the pulse shape discrimination technique, so nuclear recoils are the primary remaining background. In particular neutron elastic scattering on argon produces a signal that is indistinguishable from an hypothetical WIMP interaction, so it constitute the most insidious background. In addition to removing fake WIMP events, having an active veto allows in situ measurements of the actual neutron background in the experiment, so that background models may be compared to real data.
In this section I will briefly describe the two detectors that make up the DarkSide-50 veto system [68].

Liquid scintillator veto

The liquid scintillator veto (LSV) is an active neutron detector that is able to tag neutrons from both internal and external sources with high efficiency. It consists of a 4.0 m diameter stainless steel sphere that contains 30 tonnes of boron-loaded liquid scintillator. The scintillator mixture has basically three components: pseudocumene (PC), trimethylborate (TMB), and 2,5-diphenyloxazole (PPO). The presence of TMB - a molecule with one atom of boron - is due to ^{10}B high cross section for thermal neutron capture. In particular the $^{10}\mathrm{B}(n;\alpha)^{7}\mathrm{Li}$ reaction has a cross section of 3837(9) barn and it generates charged products which are easily detectable. There are two possible channels:

$$^{10}\mathrm{B}+n \longrightarrow \begin{cases} ^{7}\mathrm{Li}\ (1015\ keV)+\alpha\ (1775\ keV) & (B.R.\ 6.4\%) \\ ^{7}\mathrm{Li}^{*}+\alpha\ (1471\ keV) & (B.R.\ 93.6\%) \\ \quad ^{7}\mathrm{Li}^{*}\rightarrow {}^{7}\mathrm{Li}(839\ keV)+\gamma(478\ keV) & \end{cases} \tag{3.1}$$

Because both the α particle and the ^{7}Li nucleus have a short range, there is always a visible energy deposit in the LSV associated to a neutron capture. However, the emitted light is strongly suppressed due to ionization quenching, causing a scintillation signal equivalently to a 50–60 keV electron. Thermal neutrons can also be captured on hydrogen, causing the emission of a 2.2 MeV γ-ray.
Detecting these decay products therefore requires a good light collection efficiency, for this reason the sphere is lined with a reflecting foil of Lumirror. The photosensors are 110 Hamamatsu R5912 LRI 8” PMTs, mounted on the inside surface of the sphere. The measured light yield is (0.54±0.04) PE/keV allowing detection of neutrons with efficiency of 99.8 % [69].

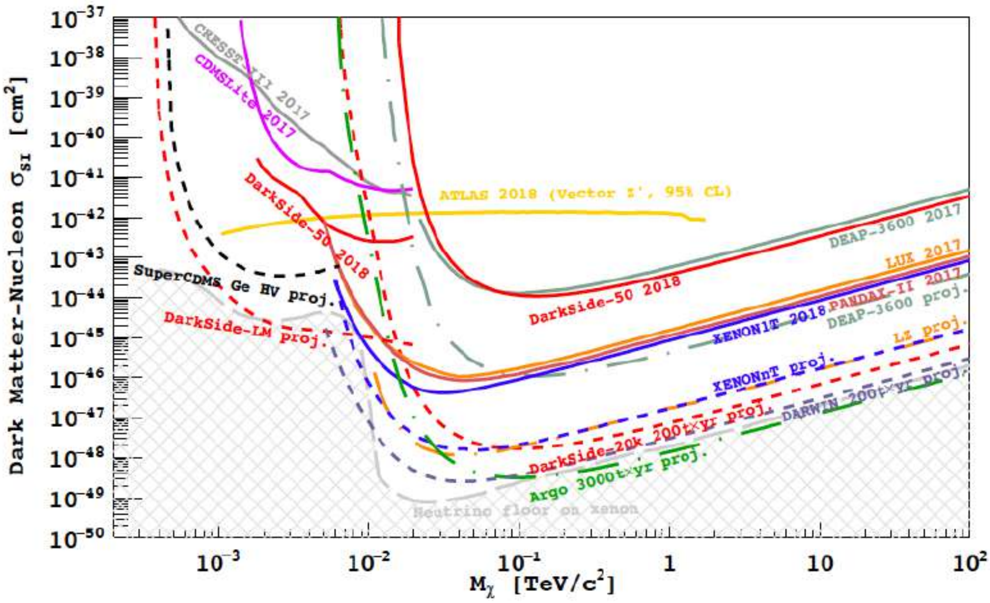

Fig. 3.3 Exclusion limits on the WIMP-nucleon cross section with spin-independent coupling. DarkSide-50 latest result is shown with the black solid line. Dashed lines represent projections for future detectors [11].

Water cherenkov veto

The water Cherenkov detector is the outermost part of the apparatus, it is used both as a efficient shield against external background, and also as muon detector based on the Cherenkov effect. It is a stainless steel cylinder (Borexino counting test facility, CTF) with a diameter of 11 m and height of 10 m that, in addition to the LSV and TPC, contains 1000 tons of purified water. The reason why cosmogenic muons can be a problem is that they are able to produce high-energy penetrating neutrons. So to eliminate any signals induced by these neutrons, the muons that generate them are directly detected. The WCV is equipped with 80 8” photomultiplier tubes that are placed on the floor of the cylinder and in columns on the lateral surface. The signal detected is the Cherenkov light produced in water by muons and their shower products. In order to maximize the light collection efficiency, all the internal surfaces are covered with a layer of Tyvek reflector and also the exterior part of the LSV sphere is covered with Tyvek.

3.1.3 Latest results

As I said DarkSide-50 is not a competitive experiment for dark matter search in the 100 GeV - TeV range, basically because of its small active mass compared to the ton scale xenon

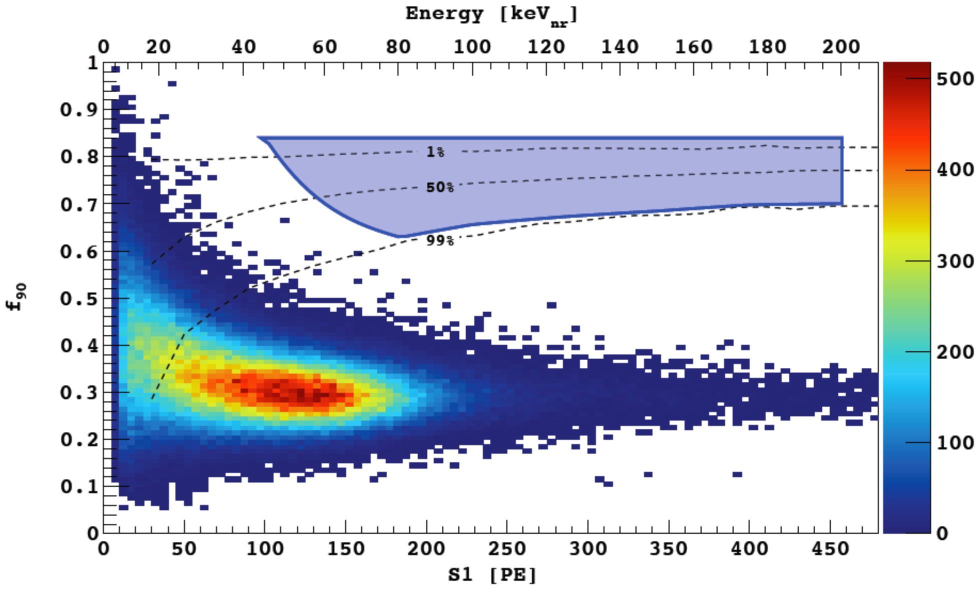

Fig. 3.4 Observed events in the $f90$ *vs.* S1 plane surviving all cuts in the energy region of interest. The solid blue outline indicates the DM search region. The 1%, 50% and 99% $f90$ acceptance contours for nuclear recoils, as derived from fits to our ^{241}Am-Be calibration data, are shown as the dashed lines.

detectors now operating. Rather, it is a prototype used to test the argon's discriminating power and verify the possibility of operating the detector in a background free mode, exploiting the extraordinary purity of underground argon (UAr).

After a first phase with atmospheric argon, the cryostat was filled with UAr in April 2015. From August 2015 to October 2017 a 532.4 live-days exposure has been accumulated and all these data have been analyzed with a blind analysis technique [11]. The basic idea was to elaborate a set of criteria to be able to reduce all the backgrounds to a level considered sufficient, without looking at possible WIMP events. So the blinding scheme consisted in hiding from users a specific category of events initially quite large and progressively allowing to see more and more data, testing the predictions. Once all the criteria for the background rejection were set, the last category of data was also opened, *i.e.* those in the region of interest for the dark matter search, the so-called dark matter box. The two main steps in the analysis were first the background predictions in the region of interest and second the developing of cuts to reduce the predicted background below the maximum level acceptable. In particular was considered acceptable 0.1 event of expected background.

All the procedure was structured around the $f90$ *vs.* S1 distribution, both the design of the dark matter box which is a region in this plane and the blinding/unblinding phases. Finally

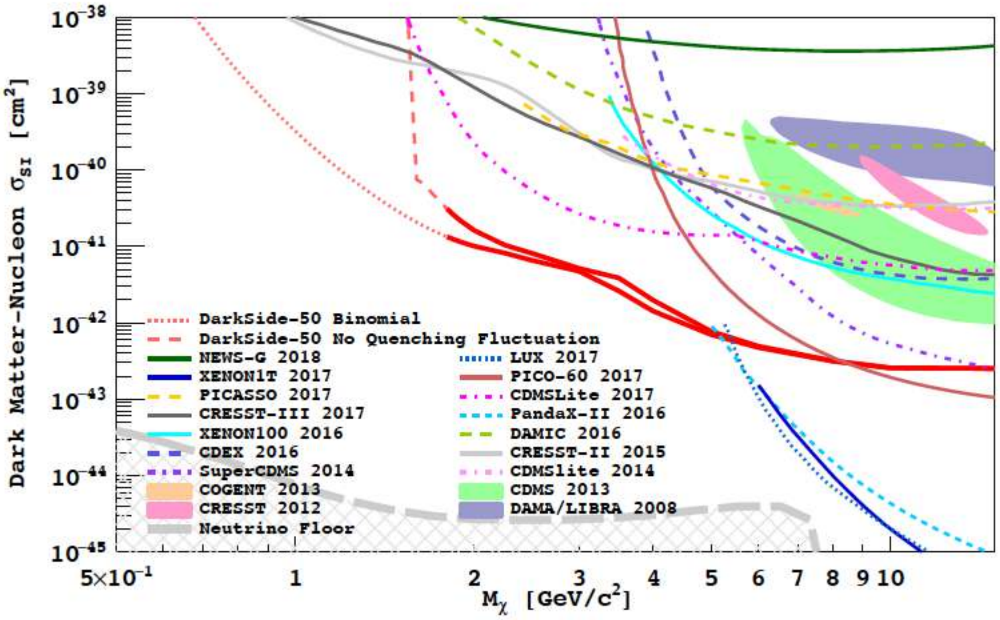

Fig. 3.5 Upper limits on the WIMP-nucleon cross section the the low mass region, above 1.8 GeV/c^2. The DarkSide-50 results, obtained from the analysis of the ionization signals, are plotted in red [12].

when the data were completely opened, and after applying the analysis cuts, no events were observed in the defined dark matter search region (see Fig. 3.4). A limit on spin-independent DM-nucleon scattering was derived assuming the standard isothermal WIMP halo model, with v_{escape} = 544km/sec, v_0 = 220 km/sec, v_{Earth} = 232km/sec, and ρ_{DM} = 0.3 GeV/c^2 cm^3. The obtained result, which is background free, as well al signal free, is consistent with up to 2.3 expected DM-nucleon scatters (90% C.L.). This corresponds to an upper limit on the spin-independent scattering cross section at 1.14$\times$ 10^{-44}cm^2 (3.79$\times$ 10^{-44}cm^2, 1.10$\times$ 10^{-44}cm^2) for 100GeV/c^2 (1TeV/c^2, 126GeV/c^2) dark matter particles (see Fig. 3.3).

Another significant result obtained with DarkSide-50 is the ability to explore the mass range below 20 GeV/c^2, performing an analysis based only on the ionization signal. Light WIMPs, with masses down to 1.8 GeV/c^2, produce low energy nuclear recoils for which detection efficiency for scintillation signals (S1) is very low. On the contrary, exploiting the gain due to the electroluminescence mechanism, it is possible to detect ionization signals (S2). The outcome of this "S2-only" analysis is a 90% C.L. exclusion limit above 1.8 GeV/c^2 for the spin-independent cross section of WIMPs on nucleons (see Fig. 3.5), extending the exclusion region for dark matter below previous limits in the range 1.8-6 GeV/c^2 [12]. In order to exploit this capability in DarkSide-20k it is necessary to improve the ionization yield

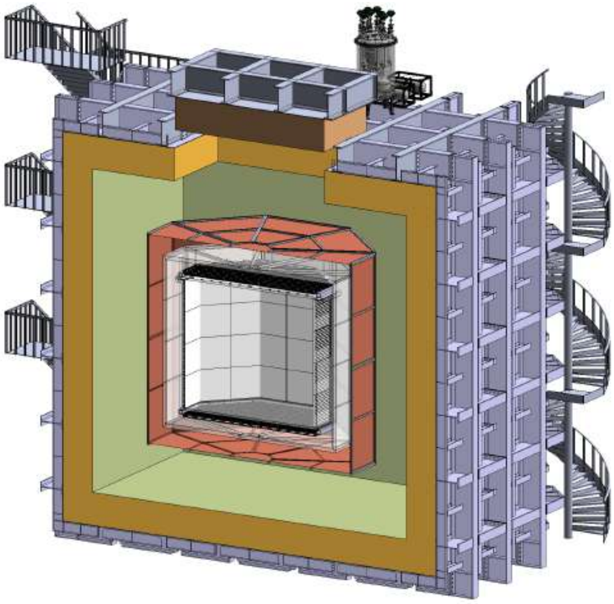

Fig. 3.6 Conceptual drawing of the DarkSide-20k detectors: the innermost part is the octagonal TPC, surrounded by the acrylic shell which is part of the neutron veto. The complete structure of the veto system in not shown in this picture, see Fig. 3.8 for details. The outer most structure is the Proto-DUNE like cryostat, that will be filled with atmospheric argon.

measurement and to elaborate a better ionization fluctuation model. The ReD project has also the purpose of characterizing the S2 signal in liquid argon.

3.2 DarkSide-20k

DarkSide-20k will be the next detector to be built at LNGS, as part of the DarkSide project. Much of the fundamental features are based on the successful experience of constructing and operating DarkSide-50 in a a background-free mode. The concentric structure of the detectors will be maintained, also in this case the dark matter detector will be a liquid argon biphasic time projection chamber (TPC), surrounded by a neutron veto (See Fig. 3.6). What changes drastically is the active mass of argon: we pass from 46.4±0.7 kg of DarkSide-50, to 38.6 t of DarkSide-20k. The entire apparatus will be positioned at LNGS, in the underground Hall C [70].

The two big differences with respect to the DarkSide-50 setup are the photosensors and the neutron veto system. Instead of the PMTs DarkSide-20k will be instrumented with cryogenic silicon photomultipliers (SiPMs), customized specifically by the Bruno Kessler Foundation (FBK) in Trento. Regarding the veto, there will be no liquid scintillator or water, but the TPC will be inserted in a large cryostat full of liquid argon, equipped with plastic structures rich in gadolinium to moderate and capture neutrons [71].

DarkSide-20k is designed to have ultra-low backgrounds and will also take advantage of the ability to measure its backgrounds with the veto system. It is foreseen to reach a sensitivity to WIMP-nucleon cross sections of 1.2×10^{-47} cm^2 (1.1×10^{-46} cm^2) for WIMPs of 1 TeV/c^2 (10 TeV/c^2) mass, to be achieved during a 5 yr run producing an exposure of 100 t yr free from any instrumental background (*i.e.* background other than ν-induced nuclear recoils). Given its exceptionally low instrumental background, DarkSide-20k could extend its operation to a decade, increasing the exposure to 200 t yr, reaching a sensitivity of $7.4 \times 10^{-48} cm^2 (6.9 \times 10^{-47} cm^2)$ for WIMPs of 1 TeV/c^2 (10 TeV/c^2) mass. DarkSide-20k is going to operate from 2022 and will either detect WIMP dark matter or exclude a large fraction of the favored parameter space.

To make the construction of this detector possible, it is necessary to carry out in parallel projects that develop the key technologies that will then be used. In particular:

1. **Low-Radioactive underground argon with Urania**: It is crucial to procure tens of tons of UAr during the next years, in order to fill the DarkSide-20k TPC. Urania is an underground argon extraction plant that will be able to procure 250 kg per day of UAr. It will be installed in Colorado, at the Kinder Morgan Doe Canyon Facility.

2. **Active depletion with Aria**: Before filling the detector the argon needs to undergo to a further chemical purification. For this purpose the Aria project consist in a cryogenic distillation column - to be installed in Sardinia, at the Seruci mine - capable of separating isotopes exploiting the tiny difference in volatility due to the difference in isotopic mass. It will aslo be the occasion to test the possibility of active depletion of ^{39}Ar.

3. **Cryogenic SiPMs**: SiPMs are considered much better detectors than PMTs for this kind of application, because of their higher photon detection efficiency and better single-photon resolution. They also feature a higher radiopurity, up to one order of magnitude better than PMTs. In DarkSide-20k about 15 m^2 of SiPMs will be needed, that will be operated in liquid argon and integrated into tiles to cover large areas.

4. **Large cryostat**: The TPC will be hosted in a ProtoDUNE-like cryostat (see Ref. [72] for details) that allows eliminating the stainless steel cryostat and placing SiPMs outside the TPC, thus reducing drastically the radioactive internal sources and lowering

Fig. 3.7 DarkSide-20k octagonal TPC. An ultra-pure acrylic sealed structure will contain the ultra-pure underground argon used as active target. Just above and below the windows there will be the SiPMs arrays, held by special mechanical supports.

the background. Furthermore, the elimination of the liquid scintillator facilitates the procedures for securing the whole apparatus at LNGS.

3.2.1 TPC

The DarkSide-20k TPC will contain a total active mass of 38.6 tons of liquid argon, in an octagonal volume with a height of 263 cm and a distance from edge to edge of the octagon of 350 cm. All the structure will be made of ultra-pure poly(methyl methacrylate) (PMMA), in particular reflector panels and top and bottom windows will separate the UAr inside the TPC from the AAr contained in the cryostat. As in DarkSide-50 all the internal surfaces are going to be coated with TPB wavelength shifter, in order to make the UV scintillation light detectable from the photosensors [73].

What we usually call a photodetector module (PDM) is the basic photosensing unit of the experiment. It is constituted by a tile of 24 SiPMs that covers an area of 50×50 mm^2 and operates as a single detector. Each silicon photomultiplier is 11.7×7.9 mm^2 big and has a 30μm cell pitch and is mounted with a 5 MΩ quenching resistance at liquid nitrogen temperature [70]. The PDM has a plastic mechanical structure that holds the tile and also hosts a cryogenic preamplifier to amplify the signal very close to the sensor. Finally, integrated in the PDM, there is an optical converter that allows to transmit the signal through optical fibers. The PDMs are grouped in mechanical units called motherboards: to cover the two octagonal windows there are both squared and triangular motherboards with the same edge size of 25 cm. The top and bottom full readout octagonal panels are made of 4140 tiles each and are going to be placed outside the acrylic vessel, above the anode and below the cathode.

As in DarkSide-50, the electrodes - needed to create the electric fields - are two transparent conductive indium-tin-oxide (ITO) films deposited on the acrylic windows and a metal grid positioned just below the liquid surface. The gas pocket is maintained by the "diving bell" shaped anode.

All components of the detector, above all the inner components, must be made from materials of highest radiopurity to keep backgrounds as small as possible.

3.2.2 Veto system

The veto system, hosted inside the ProtoDUNE-like cryostat, will be composed by three different concentric volumes. Closest to the TPC, all around it, there will be a $\sim$40 cm thick layer of active liquid atmospheric argon. This will be completely surrounded by an octagonal-shaped passive shell made of acrylic (PMMA) and loaded with gadolinium. Outside there will be a second active argon volume, again $\sim$40 cm thick. These three volumes should be optically insulated from the rest of the passive argon that fills the cryostat. The PMMA acts as passive material to moderate neutrons, while the gadolinium captures them because of its high capture cross section, resulting in the emission of multiple γ-rays. The plastic shell will be 10 cm thick and loaded with $\sim$2% by weight of Gd. The γ-rays reaching liquid argon will produce scintillation light that will be detected using SiPMs tiles, as the ones used for the TPC, placed on both faces of the acrylic structure (See Fig. 3.8). The active argon volumes will be divided into optically insulated vertical sectors to reduce the pile-up event rate and to obtain a sufficiently high photoelectron yield. The TPC outer surface, as well as the Gd-loaded structure and the sectors walls will be covered with reflector, on which TPB needs to be evaporated.

Finally, the ProtoDUNE-like cryostat will be surrounded by layers of plastic for moderation of cosmogenic and radiogenic neutrons from the rocks surrounding the LNGS Hall C.

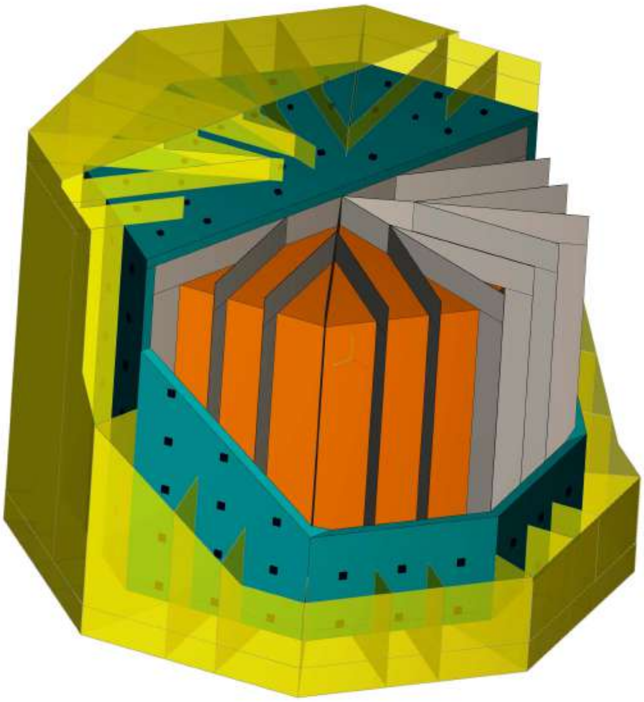

Fig. 3.8 DarkSide-20k neutron veto system. The TPC (orange) will be surrounded by an active atmospheric argon volume, optically divided in vertical sectors. The green volume in the drawing represents the PMMA shell, loaded with gadolinium; the little black squares are the photosensor tiles. Immediately outside the acrylic there will be a second active argon buffer, also optically insulated from the rest of the passive argon.

Chapter 4

ReD: the idea

As we saw in the previous chapter the DarkSide collaboration has demonstrated, thanks to the DarkSide-50 detector, extraordinary background rejection capability and it is now preparing for the construction of the DarkSide-20k detector. DarkSide-20k is designed to limit the number of instrumental background interactions to < 0.1 events during the whole exposure, so that a positive claim could be made with as few events as possible [73]. So the only irreducible background source will be due to the coherent elastic neutrino-nucleus scattering (CEnNS) interactions. Coherent scattering of neutrinos on complex nuclei was proposed in 1974 as a prominent probe to study neutral-current (NC) neutrino-nucleus processes [74] and it has been observed in 2017 from the COHERENT experiment [75]. This is a particularly challenging background because nuclear recoils from CEnNS can almost perfectly mimic an authentic weakly interacting massive particle signal. One possible feature that could be exploited to discriminate ν-induced nuclear recoils from WIMP-induced events is the sensitivity to the direction of the incoming particle [76].

As we will see in section 4.1.1, the expected WIMP events rate, assuming the Standard Halo Model (SHM), is strongly anisotropic, due to the motion of the solar system within our galaxy, in particular we expect that dark matter induced recoil distribution is pointing opposite to the Cygnus constellation direction. So having a dark matter detector with sensitivity to the direction on the recoil would allow to identify any signal with the dark matter galactic halo and hence to make an unambiguous dark matter discovery, even with few events.

The collaboration DarkSide wants to verify, through the ReD-Recoil Directionality project, whether it is possible to operate a directional detector made with a two-phase liquid argon Time Projection Chamber (TPC). The main goal of the project is to prove the directionality sensitivity, in the WIMP-Ar scattering energy range, exploiting the dependence of columnar recombination on the alignment of the recoil momentum with the electric field present inside the detector.

Moreover DarkSide-50 has recently performed an "S2-only" analysis (see section 3.1.3) which produced very competitive limits in the low mass region, between 1.8 GeV/c^2 and 6 GeV/c^2 [12]. This result opens to very promising possibilities that require a further characterization of the ionization signal. The ReD experiment can play a crucial role in deepening the S2 comprehension for low energy events, as we will see in the following.
The project aim is to irradiate a small liquid argon dual-phase TPC with neutrons of known energy and direction, produced by the TANDEM accelerator at the Laboratori Nazionali del Sud, in Catania. The scattered neutrons are detected by a neutron spectrometer that - given the closed kinematics - allows the study of the signal as a function of the scattering angle. The TPC contains many of the DarkSide-20k technological upgrades, such as cryogenic silicon photomultipliers, the non-cylindrical shape and the use of acrylic windows. This allows us also to test and develop eventual improvements to the DarkSide-20k design.
In the first part of the chapter I will briefly explain the importance of sensitivity to the recoil direction for a dark matter detector and how to obtain it in liquid argon studying the recombination mechanisms. Then I will illustrate the working principle of the ReD experiment and give a a rough estimate of the expected values.

4.1 Scientific motivation

4.1.1 Directionality

A good starting point to discuss dark matter directional detection is the assumption of the Standard Halo Model (SHM), which means a Maxwell-Boltzmann velocity distribution, that can be written as follows:

$$f(\vec{v}) = \frac{1}{\sqrt{(2\pi\sigma_v^2)^3}} exp\left[-\frac{1}{2}\left(\frac{\vec{v}+\vec{V}}{\sigma_v}\right)^2\right] \tag{4.1}$$

with $\vec{V}$ the velocity relative to the galactic center and σ_v the width of the distribution in a coordinate system at rest with respect to the center of the galaxy. It is convenient to perform a Radon transform, to write this distribution as a function of the minimum velocity and of the recoil direction, obtaining:

$$\hat{f}(v_{min},\hat{q}) = \frac{1}{\sqrt{2\pi\sigma_v^2}} exp\left[-\frac{1}{2}\left(\frac{v_{min}+\hat{q}\cdot\vec{V}}{\sigma_v}\right)^2\right] \tag{4.2}$$

where $v_{min} = \sqrt{2m_N E_R}/2\mu_{\chi N}$ and $\hat{q}$ is the recoiling nucleus momentum.

To understand if and how the recoil direction of the nucleus can influence a possible dark matter signal, it is necessary to write the recoil rate per unit mass making explicit, unlike what has been done in section 1.3.1, the dependence on the recoil direction and integrating over the energy.

$$\frac{dR(E_{th}, E_{max}, \hat{q})}{d\Omega_R} = \int_{E_{th}}^{E_{max}} dE_R \frac{d^2R(E_R, \hat{q})}{dE_R d\Omega_R} \tag{4.3}$$

The double-differential recoil rate, contained in equation 4.3, depends on the velocity distribution as follows

$$\frac{d^2R(E_R, \hat{q})}{dE_R d\Omega_R} = \frac{\rho_\chi}{m_\chi} \frac{\sigma_{\chi N} F^2(q)}{4\pi\mu_{\chi N}^2} \hat{f}(v_{min}, \hat{q}) \tag{4.4}$$

where ρ_χ is the WIMP density, m_χ is the WIMP mass, $\sigma_{\chi N}$ is the total spin-independent WIMP-nucleus cross section, $F(q)$ is the nuclear form factor and $\mu_{\chi N}$ is the WIMP-nucleus reduced mass.

It is important to observe that the anisotropy of the rate depends on the velocity $\vec{V}$, which in turn depends on the choice of the reference system. If the event is measured in a frame at rest with respect to the galactic center $\vec{V} = 0$ by definition and so the rate is isotropic. Considering instead a coordinate system at rest with respect to the Sun, $\vec{V}$ is just the component due to the revolution of the solar system about the galactic center. This velocity, denoted as $\vec{V}_{SG}$, is in the direction of the Cygnus constellation and is almost equal to the orbital speed at the Sun position $V_{SG} \approx v_0 = 220$ km/s.

The effect of this motion of the solar system is analogous to what would happen if there was an apparent "WIMP wind" coming from the Cygnus constellation, which means opposite to the Sun direction of motion. To better illustrate this anisotropy, it is useful to introduce the galactic coordinates, ($l_\odot$, $b_\odot$), that have the Sun as the origin and measure respectively the longitude in the galactic plane, $0° < l_\odot < 360°$, and the latitude above the galactic plane $-90° < b_\odot < 90°$. In this reference frame the Cygnus constellation is roughly placed at ($l_\odot$=90°, $b_\odot$=0°) while the recoil rate, that is clearly anisotropic as expected, has a peak in the opposite direction ($l_\odot$=270°, $b_\odot$=0°). In figure 4.1 it is plotted the recoil rate in galactic coordinates (see Eq. 4.3) for an argon target, assuming 200 GeV for the WIMP mass and a recoil energy interval from 50 keV up to 200 keV. The reddish region shows evidently the peak due to the "WIMP wind", pointing opposite to the Cygnus direction. Since the experimental setup is in an Earthbound laboratory, it is not practical to choose a reference frame at rest relatively to the Sun. We shall consider also the Earth orbital velocity with respect to the Sun and so the total velocity can be written as $\vec{V} = \vec{V}_{SG} + \vec{V}_{ES}$. The Earth velocity $\vec{V}_{ES}$ rotates with annual periodicity around the solar system direction of motion and

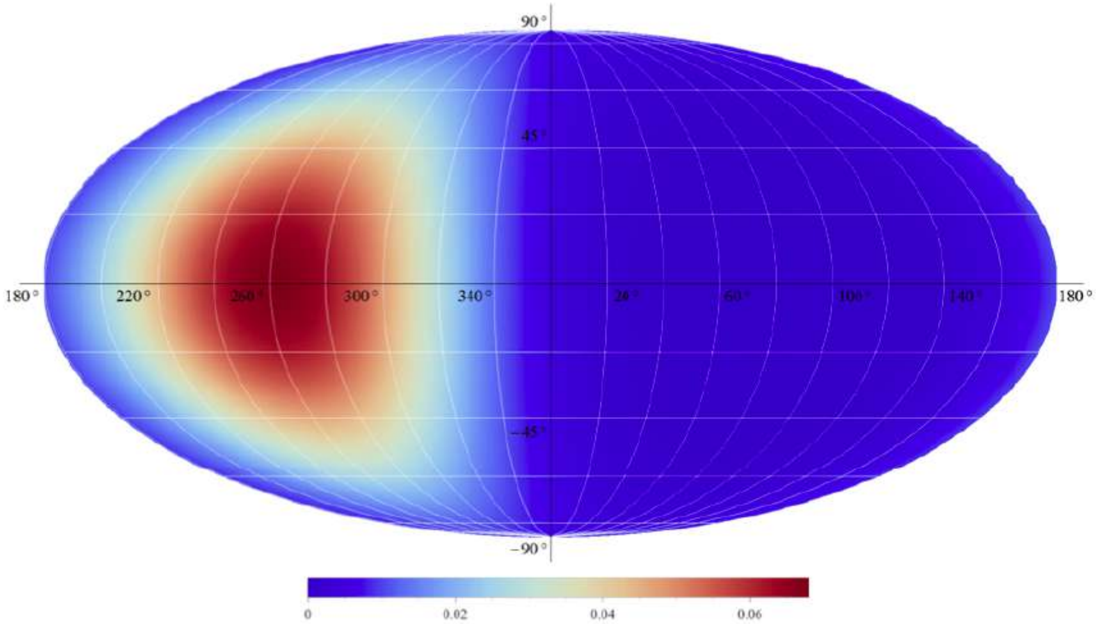

Fig. 4.1 Differential recoil rate plotted on a Mollweide equal area projection map of the celestial sphere in galactic coordinates. The chosen energy range is between 50 keV and 200 keV, the WIMP mass is 200 GeV and the cross section 10^{-46} cm^2. See Ref.[13]

this induces an annual modulation in the dark matter signal. Indeed $\vec{V}_{ES}$ can be decomposed for each position on the orbit on two orthogonal axis: at a certain moment during the year one of these projections will be parallel to the direction of the motion of the solar system. On the contrary after 6 months - as it can be seen in picture 4.2 - the same component will be antiparallel with respect to $\vec{V}_{SG}$ [77]. Clearly when the two velocities sum up the dark matter flux encountered by the Earth will reach a maximum, instead when the $\vec{V}_{ES}$ component is opposite the flux will be minimum. Therefore an hypothetical dark matter signal will exhibit an annual modulation, due the Earth revolution around the Sun, that would reach the minimum at the end of November and the maximum around the end of May. To avoid confusion it is significant to stress the fact that this modulation does not require a directional detector to be observed. Regarding this specific phenomenon the DAMA collaboration reported an observation; for further information see [58, 59].

In addition to the revolution motion around the Sun, Earth rotates on its own axis and to complete one rotation it takes a period defined sidereal day (23 h, 56 m, 4 s). The difference with respect to the solar day, that is the average time between to local solar noons, is due to the fact that Earth moves slightly along its orbit, so after a complete ratation, *i.e.* a sidereal day, it still need to rotate before the Sun reaches again noon. From now on we will use the word day referring to sidereal day. Because of this rotation the $\vec{V}$ direction in the Earthbound frame

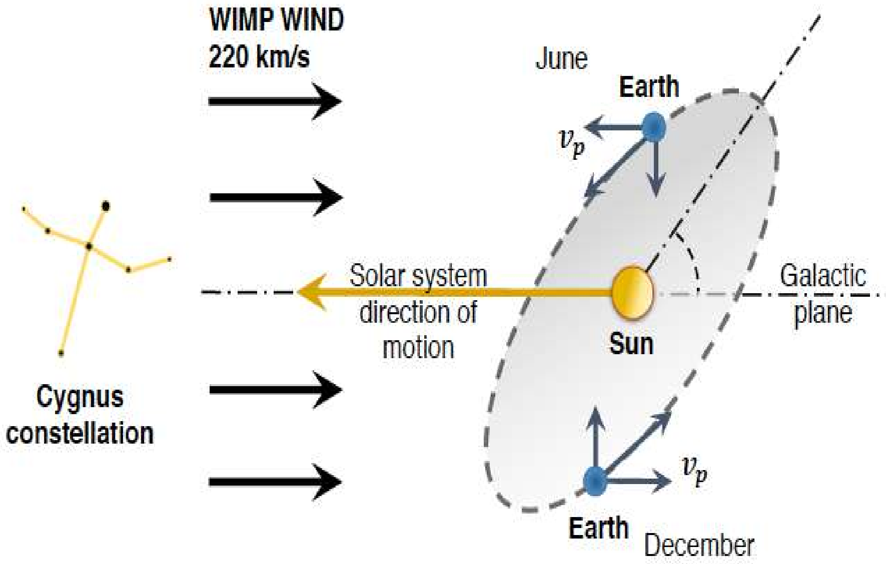

Fig. 4.2 Schematic representation of the Earth revolution around the Sun that leads to ad annual modulation in the dark matter signal. The different orientations of the Earth velocity with respect to the solar system motion in through the galaxy cause a different dark matter event rate.

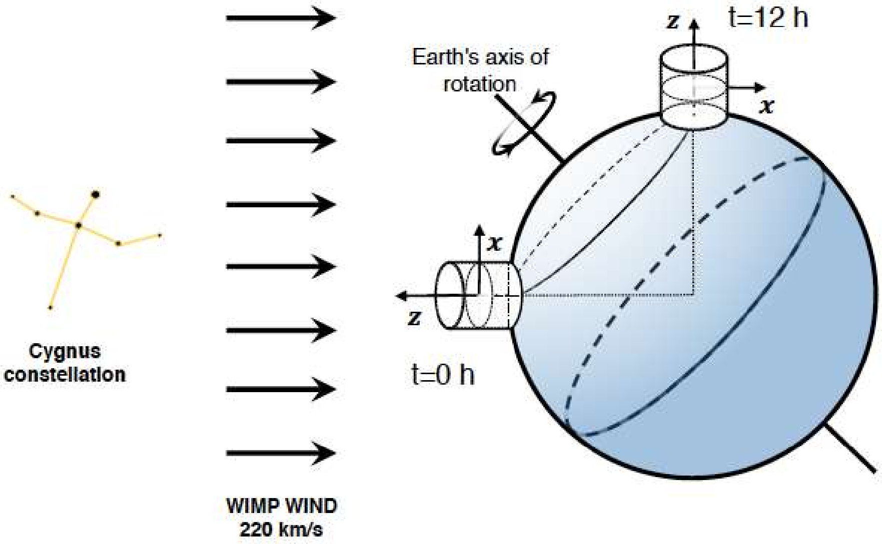

Fig. 4.3 direction variation of V during a sidereal day

changes accordingly, as shown in figure 4.3. If we consider a Cartesian coordinate system that has, for example, the $\hat{z}$ axis pointing towards the Cygnus constellation, the whole $\vec{V}$ at a given instant will be along the $\hat{z}$ axis, but after 12 hours the same $\hat{z}$ axis will be perpendicular to the "WIMP wind". This causes a daily variation of the average recoil direction [78]. The peculiarity of directional dark matter signals search is based on the study of the expected recoil rates as function of the recoil angle and of the time of the day. Choosing a reference frame at rest with respect to the laboratory, with the $\hat{z}$ in the vertical direction, the nucleus recoil angle θ_R can be defined as the angle between this axis and the nucleus recoil direction. Events can then be divided in two classes using this parameter:

- vertical events - recoils that correspond to $|cos\theta_R|\geq0.5$;
- horizontal events - recoils that correspond to $|cos\theta_R|<0.5$.

The trend of the rate of these two categories during a sidereal day is shown in figure 4.4 and it is in close correlation with the Cygnus position variation. During the first hours, when the constellation in close to the zenith there is an excess of vertical events; on the other hand between hour 10 and 20, when the Cygnus is around the horizon, the rate of horizontal events is dominant [13].

So to summarize, the sensitivity to the direction of the particle that caused a recoil would allow me, first of all, to compare that direction with the position of the Cygnus constellation

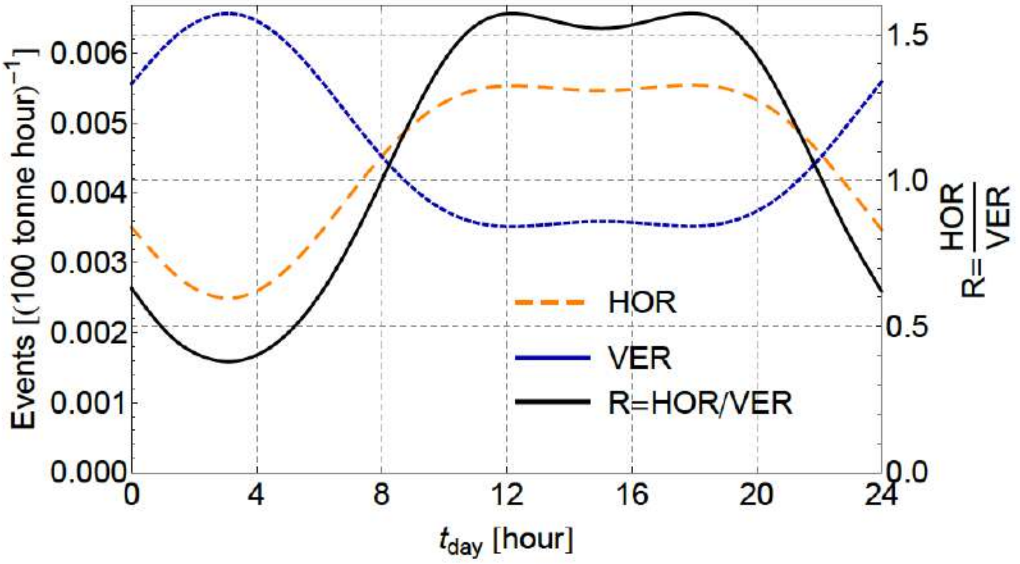

Fig. 4.4 Vertical and horizontal event rates as a function of time in event per 100 tonne per hour. Curves drawn for a reference frame at Laboratori Nazionali del Gran Sasso, in Italy at the summer solstice day.

at that time, and consequently with the one of "WIMP wind"; moreover, thanks to the daily modulation that causes a motion of the constellation with respect to the horizon, it would be possible to study the correlation between this motion and the rate of events from different directions. This feature, that is independent from the WIMP interaction details, would constitute a very strong signature that a detected new particle is indeed a dark matter candidate.

4.1.2 Columnar recombination

A possible strategy for combining a large mass detector, which could guarantee significant exposures for dark matter detection, and a detector sensitive to the direction of the incident particle, is to exploit the phenomenon of columnar recombination in a dual-phase argon time projection chamber.

As we saw in chapter 2, a nuclear recoil in liquid argon produces excitation and ionization of the surrounding atoms. A fraction of the freed electrons can avoid the recombination process, due the presence of an electric fields that drifts them away form the positive ions. Some columnar recombination models [62, 79, 80] suppose that the recombination fraction could depend on the angle between the recoil direction and the drift electric field. Let's

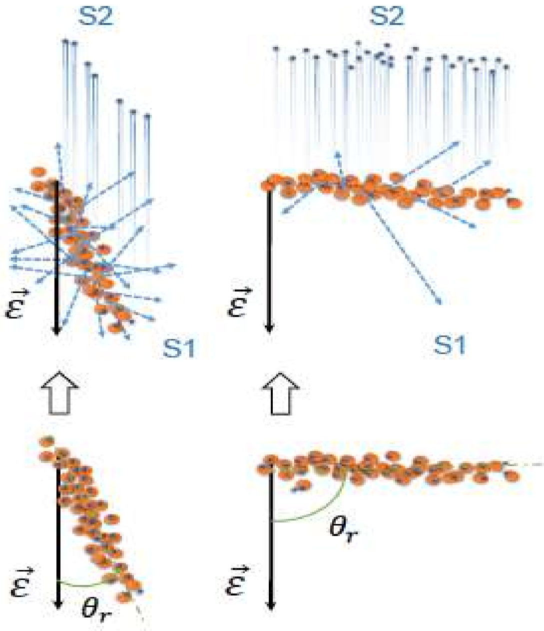

Fig. 4.5 Schematic representation of the columnar recombination effect.

examine the extreme cases to get an idea of the causes of this difference in the recombination effect. If the recoil track is perpendicular to the electric field, electrons will drift for a short distance inside the ionized particles cloud and then pass in region of neutral atoms, reducing the recombination probability. On the other hand when the track is parallel to the field lines, the free electron must pass through almost the whole column during the drift, maximizing the recombination probability. These two opposite situations are sketched in figure 4.5. To be more precise, the recombination mechanism can take place when a free electron get sufficiently close to an ion and also has the correct energy. The distance for the electron capture to occur is the Onsager radius (see Sec. 2.1), when the electrostatic potential is balanced by the electron kinetic energy. The first condition necessary for there to be a directional response, in the columnar recombination framework, is that the recoil track exceeds the Onsager radius. In liquid argon, where T= 87 K, the Onsager radius is approximately 80 nm, that correspond to a recoil energy of about 30 keV matching the energy region of interest for the direct dark matter searches [81].

The measurable effect of the electron-ion recombination is the reduction of the signal in gas (S2), which depends on the number of extracted electrons, and a corresponding increase of the scintillation in liquid (S1). So the ionization signal should reach a maximum when θ_R=90°and be minimal when θ_R=0°, depending on the perpendicular component of the electric field with respect to the recoil direction. Exploiting this feature, studying both S1

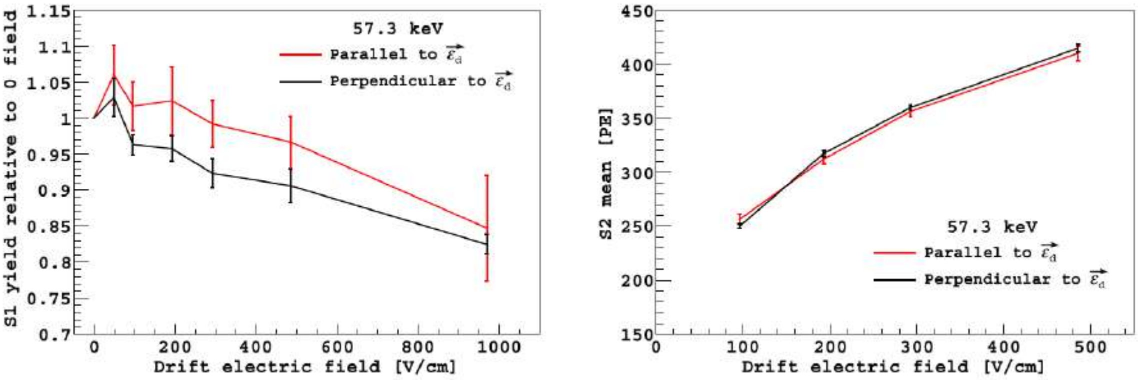

Fig. 4.6 Hints from SCENE of directional sensitivity for nuclear recoils in a LAr TPC. The scintillation light yield (left panel) decreases as a function of the applied electric field, while the ionization signal (right panel) increases. The scintillation yield for recoils parallel to the electric field direction appears higher than the corresponding one in the perpendicular direction, hinting to a greater recombination effect in the former case as expected [14].

and S2, it should be possible to extract information on the orientation of the tracks, but not to tell the direction of the recoil. This model does not have "head/tail" discrimination, so it cannot distinguish events differing by 180°. So the angular information is contained in the so-called "folded" angular recoil rate [78], defined as:

$$\frac{dR_f(|cos\theta_R|)}{d|cos\theta_R|} \equiv \frac{dR}{dcos\theta_R}(cos\theta_R) + \frac{dR}{dcos\theta_R}(-cos\theta_R) \tag{4.5}$$

Results on directional effects have been observed in liquid argon, by experiments using highly ionizing particles of several MeV energy [82]. The SCENE experiment, based on a small dual-phase liquid argon TPC, opened the possibility of building a detector sensitive to the direction of nuclear recoils. In figure 4.6 it is shown a small excess of the scintillation yield (S1 signal), for nuclear recoils parallel to the electric field with respect to those orthogonal, at an energy of the recoiling nucleus of 57.3 keV [83, 14]. This slight excess, although with a still low statistical significance, is intriguing and goes in the expected direction.

Given the importance it would have in a high mass detector like DarkSide-20k the capability to distinguish nuclear recoils parallel to the vertical direction of the drift field from the perpendicular ones, the collaboration is working to further investigate the hint given by SCENE. For this purpose was designed and realized the Recoil Directionality (ReD) project, which I will describe in detail in the continuation of this work.

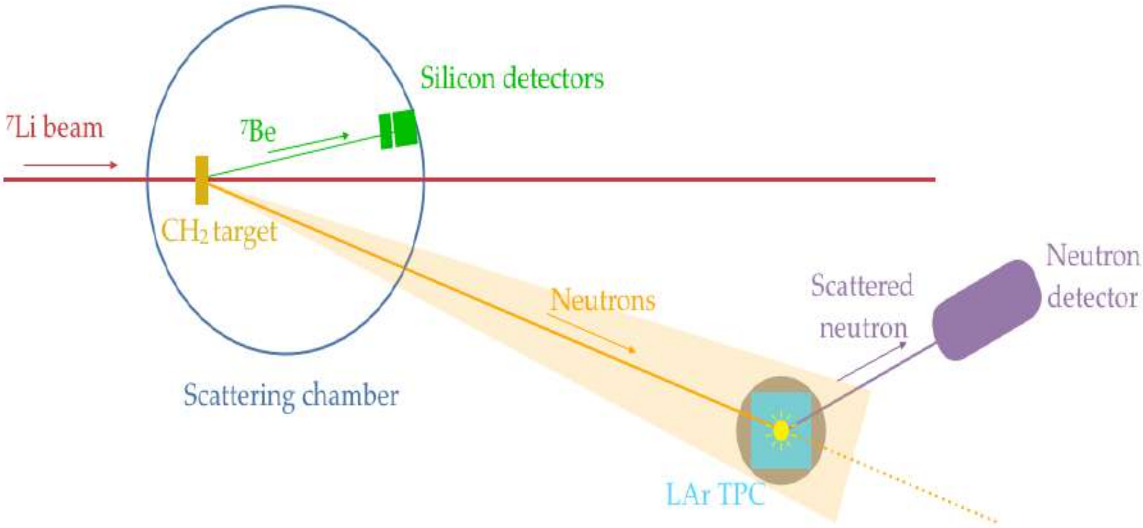

Fig. 4.7 ReD scheme

4.2 The ReD recipe

As I mentioned earlier, the primary purpose of the ReD project is to demonstrate the sensitivity to directionality for nuclear recoils in liquid argon. The heart of the project is therefore a small double-phase liquid argon Time Projection Chamber (TPC), equipped with two cryogenic silicon photomultiplier tiles. The basic idea is to expose the ReD TPC to neutrons of know energy, produced at Laboratori Nazionali del Sud (LNS), in Catania, using a TANDEM accelerator. Briefly, neutrons are produced by the reaction p(^{7}Li,n)^{7}Be, which simultaneously gives rise to a neutron and a ^{7}Be. Inside the scattering chamber, where the production reaction takes place, there are three silicon detectors: two to identify the beryllium, operated in coincidence with neutron scattering in the TPC and mounted in a telescope configuration, and the third to monitor the beam current. Furthermore, eight neutron detectors are positioned downstream of the TPC, at different angles with respect to the initial neutron direction, to identify neutrons with different scattering angles. A sketch of the entire process is shown in figure 4.7. All the details of the experimental setup will be described in the next chapter (see chapter 5). The distinguishing feature of the ReD setup is the capability of precisely identifying the energy and the direction of the nuclear recoils occurring in the liquid argon, thanks to the closed kinematic. This allows to study the dependence of scintillation (S1) and ionization (S2) signals as a function of the recoil track direction with respect to the drift field. Combining the time-of-flight measurements and the pulse shape discrimination of both the TPC and the liquid scintillators, used as neutron detectors, it is possible to have a stringent selection, performed event by event, on neutrons that produced a single elastic scattering in liquid argon. With the TANDEM apparatus is also possible to vary the beam energy, changing consequently the neutrons energy: this makes possible to study a wide nuclear recoil energy range, between 20 keV and 100 keV, that is the region of interest for the dark matter scattering on argon.

With regard to the low-energy recoils measurement, one dedicated neutron detector has been positioned in a specific geometric configuration, different with respect to all the others, that allows to select a reduced scattering angle.

4.2.1 The neutrons production and the geometry

It is quite common to produce mono-energetic neutrons through two-body reactions by bombarding light nuclei. However, these reactions give rise to isotropic neutron distributions, while in the case of ReD it is useful to have a collimated source in order to irradiate the active volume of the TPC with a sufficiently high flux. For this reason we decided to produce neutrons through the reaction p(^{7}Li,n)^{7}Be, in inverse kinematics, *i.e.* with the heavy ion used as projectile. Using this method gives the best combination between a white neutron source, which could provide a very collimated beam, and monochromatic source that will give a high flux [84].

The reaction has a threshold of $\sim$13 MeV, so a TANDEM accelerator that can reach at least 9 MV is required to obtain neutron production. This is one of the reasons that led to the installation of ReD on the 80°Catania TANDEM line: in fact the LNS hosts one of the few active infrastructures able to reach a maximum terminal voltage of 14 MV.

At the threshold energy the neutron source is mono-energetic and a 1.44 MeV neutron is produced in a known direction. Increasing the beam energy opens up new reaction channels, complicating the spectrum, and the semi-angle of the cone θ_{pn} in which the neutrons are emitted increases as follows [85]:

$$\theta_{cpn} = arcsin(1 - \frac{E_{th}}{E_{Li}}) \tag{4.6}$$

where the subscript *pn* stands for "cone of primary neutrons", to avoid any confusion between the many angles that will be introduced. To obtain nuclear recoils between few keV and 100 keV, it is necessary to produce neutrons of different mean energy and this implies, for the geometrical configuration we adopted at LNS, varying the ^{7}Li beam energy between 18 MeV and 34 MeV. In this range, as it can be seen from table 4.1 where all the possible channels are

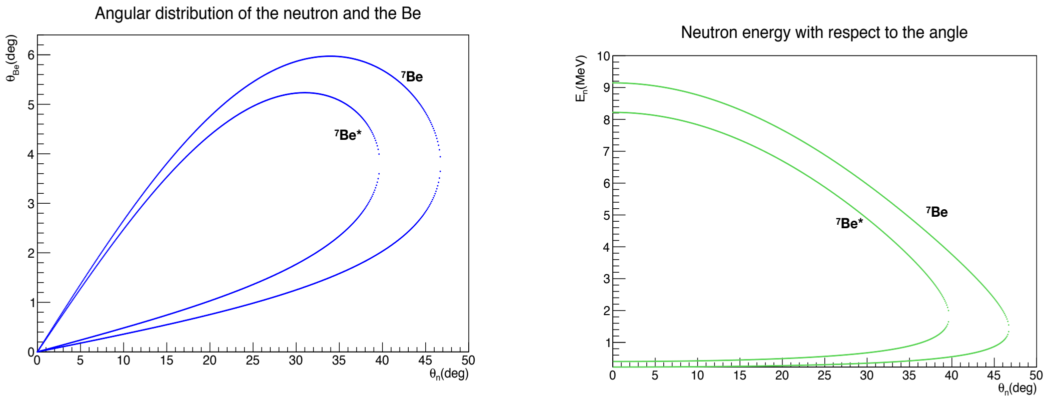

Fig. 4.8 Kinematic plots for the neutron production reaction p(^{7}Li,n)^{7}Be. *On the left:* the graph shows the angular distribution of the ^{7}Be with respect to the neutron angle. The two concentric lobes represent the ground state (external line) and the excited state (internal line) of the ^{7}Be. *On the right:* is plotted the neutron energy as a function of the emission angle. Also here the lobes correspond to the ^{7}Be states.

reported, the production of a ^{7}Be nucleus in its first excited state, at 0.429 MeV, is possible [86].

Exit channel	**Q-value (MeV)**	**Threshold (MeV)**	**Neutron energy 0°**
n+^{7}Be	-1.644	13.098	1.44
n+^{7}Be* (0.429 MeV)	-2.073	16.513	3.84
n+^{3}He + ^{4}He	-3.230	25.726	8.18
n+ ^{7}Be* (4.57 MeV)	-6.214	49.489	18.79

Table 4.1 Four possible neutron production mechanisms associated to the p(^{7}Li,n)^{7}Be reaction.

The reaction is planar, but not horizontal, in particular the interaction plane is inclined of 56.37°. On the reaction plane we can define the two production angles, with respect to the beam direction: θ_{Be} is the beryllium angle and θ_n is the neutron angle. We studied in detail the two-body kinematics, in order to find the best geometry configuration of the whole experiment, which is quite complicated. The results of the calculations, done with the LISE++ software, but also cross checked with a custom code, are shown in figure 4.8.

Finally, regarding the cross section of the production reaction, we have studied it as a function of the beam energy [85, 87] and of the angle [88]. Considering 28 MeV for the ^{7}Li energy and neutrons emitted at an angle θ_n=22.3°(we shall see in the following where this value comes from), we found $d\sigma/d\Omega$=80 mb as the best value.

The ReD geometry has been specifically designed to obtain both parallel and perpendicular nuclear recoils with respect to the electric drift field present in the TPC, *i.e.* parallel or orthogonal to the vertical direction. The experiment is performed in a fixed geometry configuration, so we decided to put the TPC in a position that would allow us to meet three crucial requirements. In particular we wanted the TPC position to:

- make possible to detect Ar recoil both parallel and orthogonal to the electric field. In this regard it would have been sufficient not to be at the same height as the lithium beam; a vertical component of the momentum of the primary neutron is needed.
- be compatible with the dimensions of all the components of the apparatus.
- allow tagging the beryllium associated with the neutron. A θ_{Be} not too small, otherwise we would have to put the silicon detectors on the primary beam direction.

The best choice to get a good compromise between the three needs is to place the TPC at 150 cm from the target and at an angle of 22.3°with respect to the beam line (See Fig.4.9). It is important to note that this a 3D angle, which is convenient do decompose on vertical and horizontal planes. This leads to define:

- φ_{tpc}=**12.8**°, as the angle, between the beam line and the horizontal projection of the vector which goes from the target to the TPC;
- θ_{tpc}=**18.4**°, as the angle between the horizontal plane containing the beam line and the vector which goes from the target to the TPC, *i.e.* the primary neutron cone axis.

Of course, by definition, these two angles identify the axis of the neutron cone we are interested in, that is why we consider θ_n=22.3°. Having fixed the ^{7}Li beam energy E_0 and the neutron angle θ_n implies also a know neutron energy E_n.

Now we need to introduce three new angles in order to describe the interaction in the TPC and the neutron detectors geometry. The recoil angle θ_R, already introduced in the previous sections, is defined by the Ar track and the electric field direction (-$\hat{z}$). The two scattering angles $\theta_{n'}$ and θ_{Ar} are respectively the angles of the diffused neutron and of the recoiling nucleus with respect to the primary neutron direction. So to have a recoil parallel to the electric field, which means θ_R=0°, it is necessary to have

$$\theta_{Ar} = 90° - \theta_{tpc} = 90° - 18.4° = 71.6° \qquad for\ //\ \vec{\mathcal{E}}_{drift} \tag{4.7}$$

At this point, since E_n and θ_{Ar} are frozen, we can obtain $\theta_{n'}$ from kinematic calculations in the non-relativistic limit at the first order:

$$\theta_{n'} = 180° - 2\theta_{Ar} \qquad \Longrightarrow \qquad \theta_{n'} = 36.8° \tag{4.8}$$

In these conditions the kinematics is closed and so also the recoil energy E_R is fixed. The ReD main purpose is to study directional effects, so we want to look at recoils with the same energy, but different θ_R. For this reason eight neutron detectors are placed all at the same scattering angle $\theta_{n'} = 36.8°$, keeping the kinematics identical, but at different azimuthal angles with respect to each other. They are distributed on a circumference that is the basis of a cone with vertex in the center of the TPC liquid argon volume, considered as the interaction point, and semi-opening angle $\theta_{n'}$ = 36.8° (See Fig.4.9). We denote the azimuthal angle on this circumference with φ_{LSci}, where the subscript stands for liquid scintillators, that are the neutron detectors we use. We choose φ_{LSci} = 0° in the lowest point of the circumference. Different φ_{LSci} tag events with the same energy, but different θ_R. Let's give the two limit examples: when θ_R= 0° the scattering is contained in a vertical plane where the argon nucleus goes downwards, while the scattered neutron points to the top neutron detector, which corresponds to φ_{LSci} = 180°; on the other hand when is θ_R= 90°, keeping the same $\theta_{n'}$ and θ_{Ar} implies that the neutron can point to two symmetric detectors one in φ_{LSci} = 83.6° and the other in φ_{LSci} = 276.4°. As we said before, to study different E_R values we need to change E_n by varying the beam energy E_0.
There is also a ninth neutron detector - that we will call LSci∅ - which is devoted to the low energy measurement. It is placed at $\sim$ 4.3° scattering angle, that corresponds to a recoil energy of $\approx$ 1 keV. This measurement is particularly delicate and more detailed studies are being performed at the time of writing, for a more detailed description see [89]. Now that we explained the geometry configuration needed for physical constraints let's go back to the scattering chamber and the beryllium tagging. Because the TANDEM beam is continuous, it is necessary to have a trigger signal. Tagging the ^{7}Be and requiring a coincidence with the TPC, taking into account the time of flight of the neutron, can provide a nice trigger to the whole system. Of course the silicon telescope has to be able to distinguish between different particles, to avoid random coincidences with scattered ^{7}Li. Taking into account the kinematics of the reaction, the relation between the angles is the following:

$$\theta_{Be} = sin^{-1}\left(\frac{p_n}{p_{^7Be}} sin\theta_n\right) \tag{4.9}$$

with p_n and $p_{^7Be}$ the neutron and beryllium momentum respectively. This equation in our case, for θ_n = 22.3°and E$_0$ = 28 MeV, leads to θ_{Be} = 5.15°. In order to protect the silicon

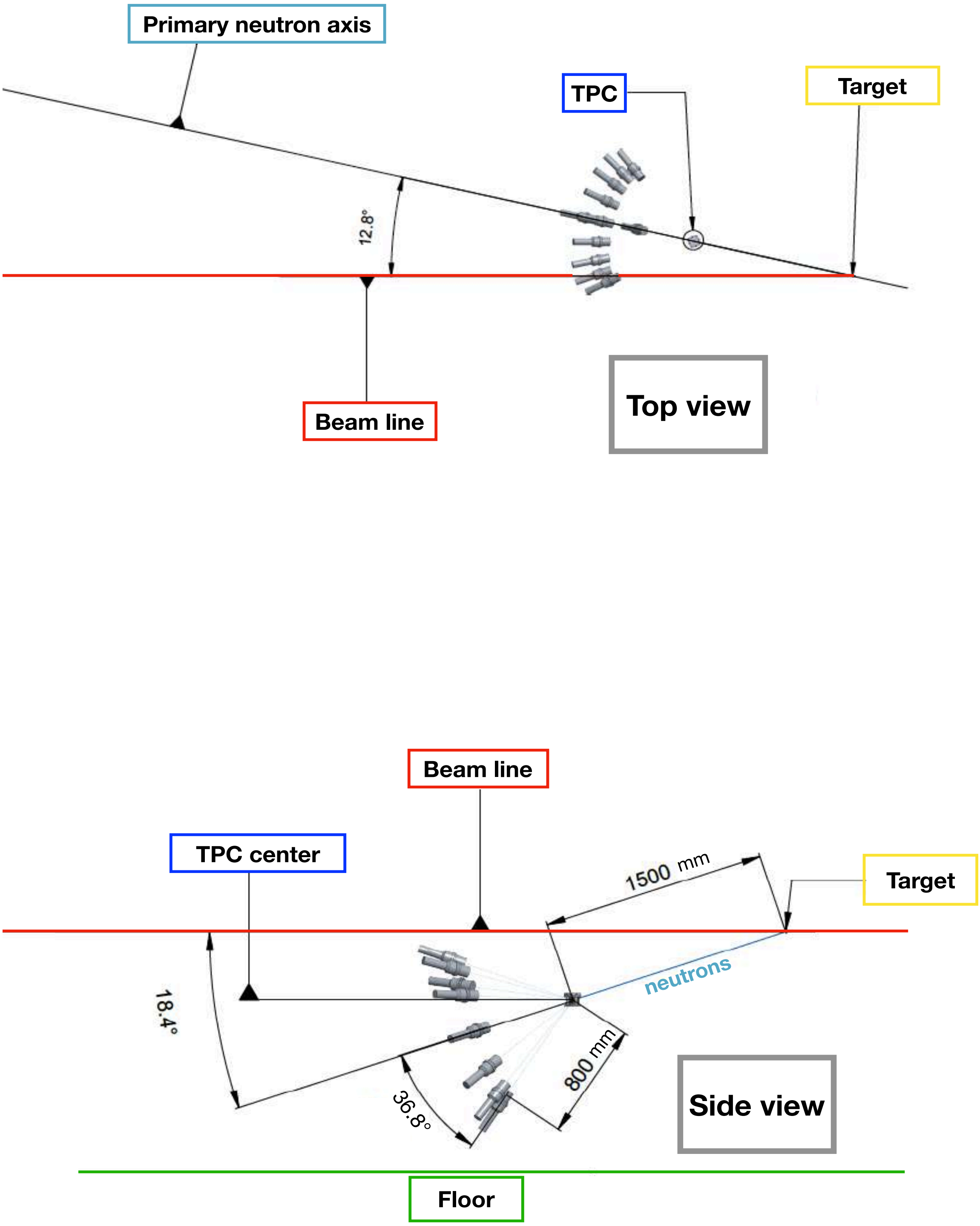

Fig. 4.9 ReD geometry. *Top:* View of the experiment from the top. The horizontal projection of the primary neutron axis forms a 12.8° angle with the beam line. *Bottom:* Side view of the setup. The primary neutron cone axis, that corresponds by construction to the line passing through the target and the TPC, forms a 18.4° angle with the horizontal plane of the beam line.

telescope from radiation damage we mounted in front of it a 3 mm diameter collimator (see Sec.5.4 for technical details), which selects a solid angle of 0.0326 msr, that corresponds to a total opening angle of the ^{7}Be cone of 0.4°. Differentiating equation 4.9 we find that dθ_n = 4.4·dθ_{Be}, that means that the neutrons cone has an opening angle of ~2°. This is important to evaluate if the TPC is completely irradiated, as we will see in chapter 6.

4.2.2 Rough expectation values

For the directionality measurement, the type of events we select are the so-called triple coincidences, in which the Si-telescope, the TPC and one of the eight LScis simultaneously record a signal. To get an idea of the expected rate of events, we split the process in two steps by first estimating the rate of neutrons incident on the TPC and then the scattered neutrons on one of the eight detectors.

Neutron rate on the TPC The number of neutrons that enter the TPC per unit time can be written as:

$$\frac{dN_{n,tpc}}{dt} = \frac{dN_{Li}}{dt} \cdot \rho_H \cdot d_t \cdot \frac{d\sigma_{Li,H}}{d\Omega}(E_0, \theta_n) \cdot d\Omega_{tpc} \tag{4.10}$$

with $\frac{dN_{Li}}{dt}$ the number of lithium ions that arrive on the target per unit time, ρ_H the H number density in the target, d_t the target thickness, $\frac{d\sigma_{Li,H}}{d\Omega}(E_0, \theta_n)$ the ^{7}Li cross section at a given energy and angle, $d\Omega_{tpc}$ the solid angle corresponding to the TPC with respect to the interaction point. Since what we measure is the electrical beam current, to get the number of ions we need to divide by $3e$: for simplicity I assume i_{beam} = 3 nA, which is a reasonable value for the TANDEM performances, so I get $\frac{dN_{Li}}{dt}$ = 6.24× 10^9 s^{-1}. The target is characterized by its mass surface density, which can be converted in the H numerical surface density eliminating the target thickness d. To give a reference, we used a CH$_2$ target of 244 μg/cm^2 that corresponds to ~2.1×10^{19} cm^{-2}. The ^{7}Li cross section as we said can be considered flat with respect to the neutron angle, so for E$_0$ = 28 MeV the best value is 80 mb [85]. Finally the $d\Omega_{tpc}$ can be easily calculated assuming a 5×5 cm^2 area for the TPC surface illuminated by the neutrons, at 150 cm from the target, obtaining 1/900 sr. Putting everything together:

$$\frac{dN_{n,tpc}}{dt} = (6.24 \times 10^9)s^{-1} \cdot (2.1 \times 10^{19})cm^2 \cdot 80\,\frac{mb}{sr} \cdot \frac{1}{900}sr = 11.6\,Hz \tag{4.11}$$

Neutron rate on one LSci The number of neutrons scattered on one of the LScis can be estimated following the same logic, so:

$$\frac{dN_{n',LSci}}{dt} = \frac{dN_{n,tpc}}{dt} \cdot \rho_{Ar} \cdot d_{Ar} \cdot \frac{d\sigma_{n,Ar}}{d\Omega}(E_n, \theta_{n'}) \cdot d\Omega_{LSci} \tag{4.12}$$

where $\frac{dN_{n,tpc}}{dt}$ is the neutron rate on the TPC calculated above, rho_{Ar} is the argon numerical density, d_{Ar} is the argon thickness that for simplicity we assume $\sim$ 5 cm. Finally $\frac{d\sigma_{n,Ar}}{d\Omega}(E_n, \theta_{n'})$ is the differential neutron elastic scattering cross section in argon and $d\Omega_{LSci}$ is the LSci solid angle referenced to the TPC center. With the described setup the neutron energy E_n at 22.3° is 7.4 MeV (see [86] for further details) so the cross section, evaluated using the Evaluated Nuclear Data File [90], is $\sim$ 0.7 b/sr. The solid angle at 80 cm, considering that the LSci has a 3” diameter, is 7.13×10^{-3}. Substituting the numerical values in 4.12, we get:

$$\frac{dN_{n',LSci}}{dt} = 11.6\,Hz \cdot (2.11 \times 10^{22})\,cm^{-3} \cdot 5\,cm \cdot 0.7\frac{b}{sr} \cdot (7.13 \times 10^{-3})\,sr = 6.1 \times 10^{-3}\,Hz \tag{4.13}$$

Assuming the detection efficiency equal to 1 for the TPC and 0.3 for the LSci [91], the triple coincidence rate on one single LSci is:

$$R_{triple} = 1.83 \times 10^{-3}\,Hz \Longrightarrow 158\,cpd \tag{4.14}$$

All the previous values are consistent with the Montecarlo simulations performed.

Chapter 5

ReD: the hardware

The ReD experiment, located at Laboratori Nazionali del Sud (LNS) in Catania, consists of a rather complex experimental apparatus that for simplicity I conceptually divide into three parts. The first part includes everything related to the neutron production and the tagging of the associated beryllium. In particular a silicon telescope, used to identify the ^{7}Be, is placed in the scattering chamber, where there are the targets and the production reaction starts. The second part is a dual-phase argon Time Projection Chamber (TPC), equipped with two new generation cryogenic silicon photomultiplier (SiPMs) arrays to detect the light produced by the neutron scattering on argon. This small TPC contains many of the DarkSide-20k technological upgrades, such as - besides the new photosensors - the non-cylindrical shape and the use of acrylic windows. This allows us also to test and develop eventual improvements to the design. Another ReD peculiar feature is the single-channel readout of the 24 SiPMs present on the top array: we developed a front end board able to read and amplify the signal of each single SiPM, in order to have a better position resolution for the ionization signal. Together with the TPC there is a custom made cryogenic system for the argon liquefaction, purification and recirculation. Finally, the third part is the neutron spectrometer, made of nine liquid scintillator based detectors, to tag scattered neutrons at different angles. A picture of the whole setup on the 80° beam line at LNS can be seen in figure 5.1.

In this chapter I will give a detailed overview of each part of the ReD apparatus, which I contributed to assemble, test and in some parts also to design. I will describe separately the different detectors used, but I will also discuss their integration into a single system. I will then briefly present the slow monitoring and the data acquisition systems. Finally I will describe the mechanical alignment procedure, elaborated and implemented in order to meet the geometry requirements set out in the previous chapter.

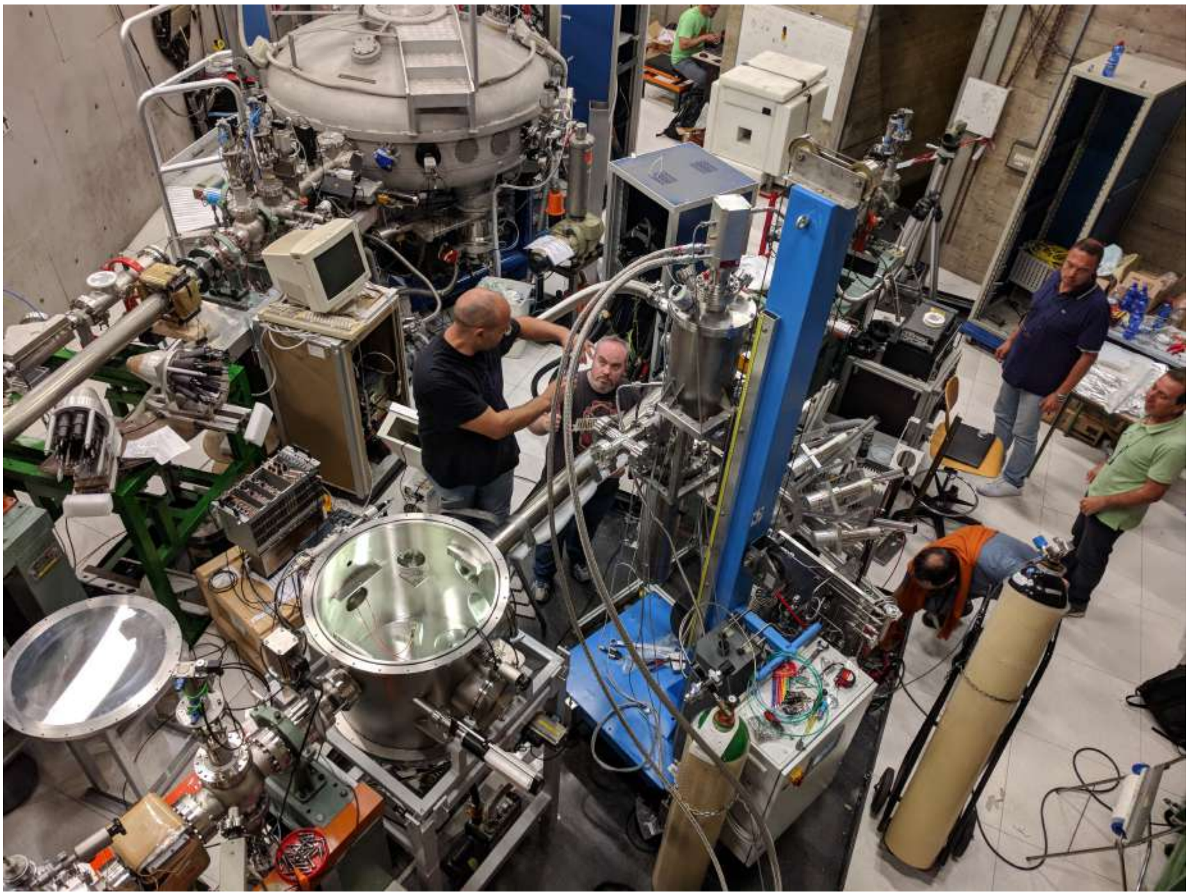

Fig. 5.1 ReD apparatus at Laboratori Nazionali del Sud (LNS), in Catania. The picture was taken during the mounting phase on the 80° beam line. On the left you can see the scattering chamber, which is open, beacuse of the silicon detectors installation. At the center there is the light blue cart holding the cryogenic system. Behind it, on the right, it can be seen part of the neutron spectrometer.

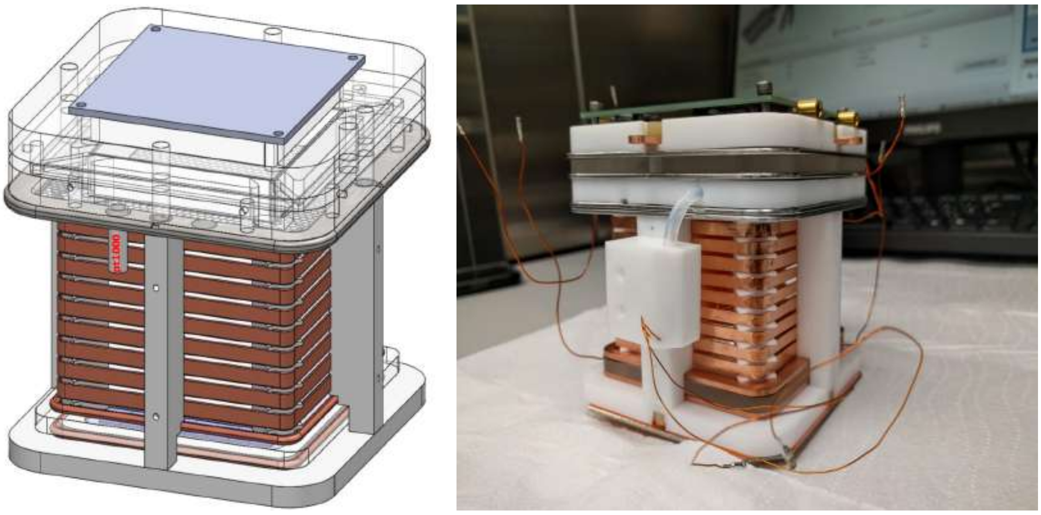

Fig. 5.2 ReD TPC. *On the left:* a 3D drawing of the TPC. *On the right:* a picture of the TPC from which you can see the bubbler structure with the gas inlet tube.

5.1 TPC

The ReD dual-phase Time Projection Chamber (TPC) can be considered the heart of the whole apparatus. It has an innovative geometry, realized by the UCLA DarkSide group, which consists in a square-section volume of 5 cm (length) × 5 cm (width) × 6 cm (height). The inner volume is delimited by two 4.5 mm thick acrylic windows, one at top and the other at the bottom, and by a reflecting "sandwich" acrylic structure on the four walls. Each window is covered on both sides with a 25 nm thick conductive layer, made of tin-indium-oxide (ITO), as in DarkSide-50, which allows to set them to a fixed potential and use them as electrodes. The four vertical walls consist in two 1.5 mm thick acrylic plates which have in between a 3M enhanced specular reflector (3M™ESR) film, with a 98% minimum reflectivity [92]. The "sandwich" protects the 3M reflective surface without reducing the light amount, thanks to the extremely high acrylic transparency; this also avoids the use of PTFE reflector, which was proven with DarkSide-50 to be a Cherenkov background source, that needs to be minimized for DarkSide-20k. Since argon emits 128 nm photons (see Chapter 2), we convert them into visible light, with a wavelength around ∼420 nm which corresponds to the maximum photo detection efficiency of our SiPMs. For this reason the entire internal surfaces of both the windows and the walls are evaporated with tetraphenyl butadiene (TPB) wavelength shifter: the coating thickness is between 160 $\mu g/cm^2$ and ~ 200 $\mu g/cm^2$.
The chamber can be operated both in single and double phase, with different field configurations. All around the active volume there is a field cage made of nine copper shaping rings spaced 0.5 cm from each other. At one centimeter from the top window there is the

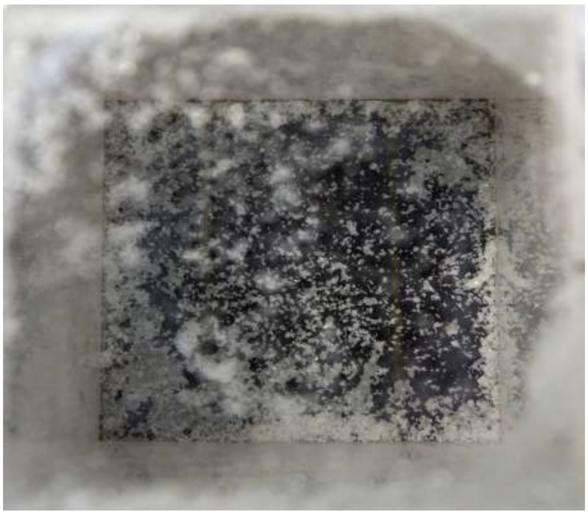

Fig. 5.3 TPB degradation on the acrylic windows. Whitish fragments were spread all around after the first warm up of the system, some can be seen deposited on the grid.

extraction grid, which is a 50 μm thick stainless steel etched mesh, with hexagon cells and a 95% optical transparency.
The outer part of the detector is a PTFE supporting structure made of four main pillars to hold the field cage and two squared frames to sustain the acrylic windows. A third separate PTFE frame is placed on the top window - fixed with vented tefon screws - and it has four copper eyelets in the middle of each side (see Fig.5.2 on the left) to hang the TPC to the cryostat flange through threaded rods.
To create the gas pocket there is a bubbler - placed outside the TPC itself as shown in figure 5.2 - that consists in a Pt1000 resistor acting as a heater. After the gas bubbles are produced, they are released through a tiny teflon tube in an interspace between the external PTFE frame and the active volume. From here the gas passes in the active volume through a cutting in the acrylic "sandwich". The anode window itself, maintained strictly attached to the vertical walls, keeps the volume gas tight. The gas pocket height is mechanically fixed at 7 mm because of a hole placed 3 mm above the grid: when the gas reaches the hole bubbles start to escape, basically because of an overfull mechanism. So when operated in double phase the TPC should have a 5 cm maximum drift length, which corresponds to the distance between cathode and grid, a 3 mm thick liquid argon layer above the grid and a 7 mm thick gas pocket.

After the TPC was subjected to an entire thermal cycle, *i.e.* it was cooled, immersed in liquid argon and then heated up, the status of TPB was strongly degraded. As can be seen in the figure 5.3, most of the TPB, recognizable by its whitish color, is detached from the upper window. Flakes of TPB are visible on the grid and around. From a first visual inspection we can't say if also the ITO coating is degraded, since it is transparent. The

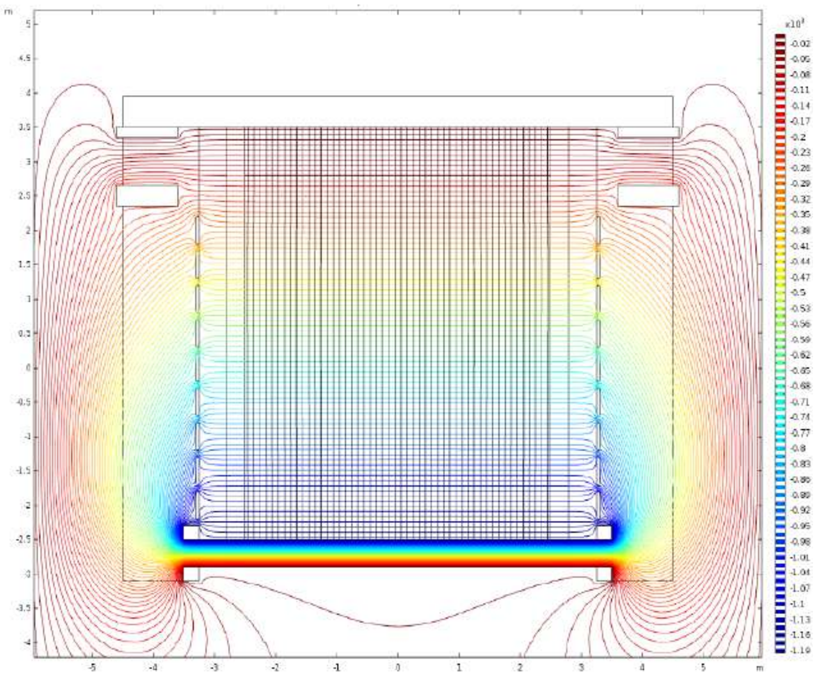

Fig. 5.4 Electric field simulated with the COMSOL software, the contour is the electric potential, while the stream in the electric field. Side view of the TPC. The set values should guarantee a uniform drift field of 200 V/cm.

causes of this phenomenon are still under investigation: one possible hypothesis is that the matching between acrylic, ITO and TPB is not optimal because of different thermal expansion coefficients, another simpler idea is that the first evaporation could have had some defects. In the meantime, the windows have been re-evaporated and subjected to thermal tests. As the status of the TPB was satisfactory after the tests, the TPC was re-assembled and put back into operation.

5.1.1 Electric fields

One of the most delicate aspects in a TPC is the electric field configuration. In order to have stable and uniform fields a special care was devoted to the voltage settings, that have been optimized with a COMSOL simulation. The results are shown in figure 5.4. Using a custom-made triple feedthrough realized at UCLA, we are able to set to potential three different electrodes. In particular we decide to operate the TPC keeping the grid grounded (by connecting it to the flange with a dedicated contact) and providing three different voltages to the anode, the cathode and the first ring of the cage. The idea was to use as a starting point the DarkSide-50 standard fields and in order to obtain the correct values we applied the configuration summarized in table 5.1. Between each ring of the field cage two 100 MΩ

Voltage				Field		
Anode	**Cathode**	**Grid**	**First ring**	**Drift**	**Extraction**	**Electroluminescence**
+3780 V	-815 V	0 V	+85 V	200 V/cm	2.8 kV/cm	4.2 kV/cm

Table 5.1 Standard electric fields configuration in double phase

resistors welded in parallel: so the voltage divider has 450 MΩ equivalent resistance. The first ring potential value is due to the fact that an extra field is needed in order to compensate some side effects and ensure a uniform drift field. To avoid the entrance into the system of a noise contribute, injected by the high voltage power supply, we have realized a simple low-pass filter placed immediately before the feedthrough, out of the dewar.

5.2 Photoelectronics

One of the ReD experiment peculiar characteristics are the photosensors used to read the TPC signal. Ours is in fact the first prototype of dual phase argon TPC, equipped with cryogenic silicon photomultipliers. The SiPMs used have been developed by FBK (Fondazione Bruno Kessler) and have just some minor differences with respect to those produced for DarkSide-20k [93]. The read out electronics, realized with the joint effort of the Naples, LNGS and Bologna INFN groups, allows both the supply of the photosensors and the amplification of the output signals [94].

5.2.1 SiPMs

Silicon Photomultipliers (SiPMs) are innovative and versatile light detectors with a better photon detection efficiency (PDE) with respect to PMTs and a much higher single photon resolution, in addition to the fact that they work with low bias voltage. The fundamental unit that constitutes a SiPM is the so-called SPAD, which stands for Single Photon Avalanche Diode. One single SiPM in fact it is nothing but a set of SPADs added together summed in parallel, in order to get a signal proportional to the number of primary photons. To get an idea of the photosensor working principle let's start from the SPAD. It is a reversed polarized junction operated in Geiger mode: *i.e.* when a photon generates an electron/hole pair these charged carries are drifted by an electric field and when they reach the multiplication region they induce an avalanche. The voltage needed to have an electric field sufficient to trigger an avalanche is called break down voltage [95]. SPADs are biased a few volts above this threshold value, so usually:

$$V_{bias} = V_{bd} + V_{ov} \tag{5.1}$$

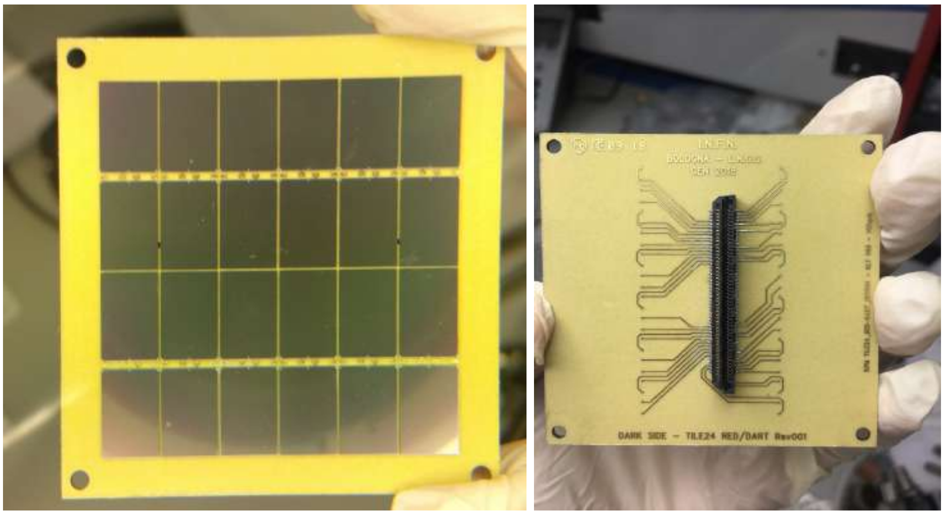

Fig. 5.5 NUV-HD SiPMs tile. *On the left:* front view of the 24 rectangular SiPMs bonded together on the tile. *On the right:* back view of the tile with the wire routing from the FEB connector.

where V_{ov} is the over voltage value. The discharge is self-sustaining, so a passive quenching mechanism, consisting in high resistance placed in series with the SPAD, was adopted in order to stop the current. After the quenching phase the diode can recharge and it becomes ready to detect a new signal. This avalanche mechanism gives rise to an electric current which does not depend on the number of photons in a single SPAD, so a SPAD is basically a binary device. For this reason they are grouped together, each with its own quenching resistance, to form a SiPM: to give an idea, one SiPM is made of thousands SPADs, that have micro-metric dimensions. Measuring the total charge of the SiPM signal one can obtain the number of fired SPADs and consequently the number of arrived photons.

SiPM signals are characterized by a fast rise of the order of few nanoseconds, due to the start of the avalanche, followed by a slow tail of the order of μs, which depends on the recharge time of the cells. SiPMs usually have a gain between 10^5 and 10^7 and a single photo-electron resolution around $\sim 2\%$. Another important parameter is the photon detection efficiency (PDE), that is defined as:

$$PDE = QE \times \mathcal{P} \times \varepsilon_{geom} \tag{5.2}$$

where QE is the quantum efficiency, $\mathcal{P}$ is the probability of generating an avalanche and ε_{geom} is the geometrical efficiency that strongly depends on the active area of the SiPM. The quantum efficiency is the probability that an incident photon generates an electron/ion pair, while $\mathcal{P}$ is the probability that charged carriers reach the multiplication region and generate a discharge. The PDE increases with increasing over voltage [96]. There are different mechanisms that cause noise contributions in SiPMs, the dark count rate and three types of correlated noise. Let's briefly describe them:

1. *Dark Count Rate* - DCR is due to a charged carrier not generated by a photon. At room temperature charges are produced by thermal emission, while at liquid argon temperature by tunneling effects. The signal has amplitude equal to a single photoelectron and an exponential time distribution probability. It increases with the over voltage.
2. *Direct Cross Talk* - DiCT occurs when a photon, generated during an avalanche, reaches a neighbouring cell and provokes a new avalanche. The time difference with respect to primary pulse is of the order of picoseconds, so it is not distinguishable. So the detectable signal, which is the superposition of the primary event with the DiCT, has an amplitude of at least two photoelectrons.
3. *Delayed Cross Talk* - DeCT is caused by an avalanche generated photon that is absorbed in a non-depleted region. The produced carrier diffuses through the silicon until it reaches a multiplication region and triggers a discharge. The amplitude is 1 PE but the pulse is delayed of a few nanoseconds with respect to the primary event, because of the diffusion time.
4. *Afterpulsing* - AP is related to electrons that remain trapped by impurities of the lattice. When released, they induce a new avalanche in the same cell as the first event. For this reason the time distribution and the amplitude depend both on the trapping time constant and on the cell recovery time. In fact if the cell is not completely recharged the after-pulse has a reduced height.

For ReD we use 11.7×7.9 mm^2 rectangular NUV-HD SiPMs, that means they have the maximum photon detection efficiency at $\sim$ 420 nm in the near ultraviolet and have a high density of SPADs. As I said previously, this is the reason why we need to evaporate TPB wavelength shifter on the internal surfaces. The SiPMs are characterized by a triple doping concentration, a 25 μm cell pitch and a 10 MΩ quenching resistance. The SiPMs are assembled in two tiles (see Fig.5.5) that are placed at the top and at the bottom of our TPC. We usually operate them at 7 V of over voltage, which means V_{bias}=34 V. The voltage distribution is different between top and bottom tiles because of the readout electronics, as explained in the following section.

5.2.2 Front-end board

The front-end board (FEB) has been designed to be coupled directly to the tile, to distribute the bias voltages of the SiPMs and to amplify the signals. The key point of the device is the

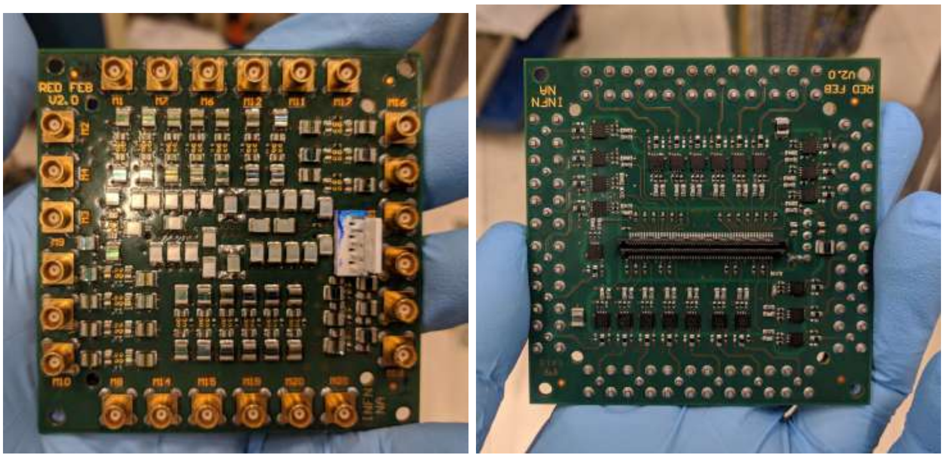

Fig. 5.6 24 channels readout front end board designed an realized in Naples, in collaboration with the LNGS and Bologna DarkSide groups.

low-noise transimpedance amplifier (TIA) based on the LMH6629SD, which is a high-speed and low-noise operational amplifier, characterized by a bandwidth of 900 MHz and an input noise of 2.6 pA/$\sqrt{Hz}$ [97]. In the WSON-8 package there is a compensation pin that allows to decrease the minimum gain from 10 V/V to 4V/V, reducing the bandwidth and increasing the stability of the device.

For the bottom tile we chose to divide the SiPMs in four groups, each made of six SiPMs, and amplify them with an independent TIA. The six SiPMs are arranged putting couples in series and then the three series in parallel one with respect to the other. In order to read the tile we use a four channels FEB, realized at Laboratori Nazionali del Gran Sasso, which also has a voltage divider to distribute the bias. For this reason in order to apply V_{bias}= 34 V we actually supply the bottom FEB with 68 V. On the contrary for the top tile we decided to implement a single-SiPM readout, in order to improve the resolution on the S2 signal.

The 24-channel FEB, designed and assembled at Univeristà degli studi di Napoli Federico II, in Naples , in collaboration with the LNGS and Bologna DarkSide groups, is shown in figure 5.6: you can see on the left the front part of the FEB with 24 MCX connectors for the output signals and on the right the back part with the SAMTEC connector for the tile. The 24 amplifiers, set in inverting configuration, need a ± 2.5 V supply that is delivered via a 5-pin connector which also allows the distribution of the bias voltage. The power supply used for the ± 2.5 V is the Agilent E3631A, which is a low-noise almost linear device, to minimize the electronic noise. All passive devices, made in SMT technology, are the same chosen for DarkSide-20k, on the bases of their respective nominal-value tolerances and on their radio-purity properties at cryogenic temperatures.

The FEBs were tested both at room and cryogenic temperature, first without the tile, than with a "fake-tile" to simulate the loads of the SiPMs, finally with the tile attached. In the case of the 24-channel FEB, an oscillating behavior was shown, which required the use of the above-mentioned compensation pin and a higher feedback resistance, that was changed from 4 kΩ up to 10 kΩ.

5.3 Cryogenic system

ReD is equipped with a cryogenic system, developed specifically by the Criotec company in Chiavasso, which can liquefy gas argon and then recirculate it and purify it, operating as a completely closed system. There is also an electric panel, which allows for an electronic control of some of the parts. Finally the most of the components can be moved in different positions, since they are attached to a cart equipped with a winch. The system is rather complex and we will go through its components exploiting the figure 5.7. The main parts are the following:

- **Condenser:** it is the custom designed unit responsibile for the argon cool down and liquefaction. It consists of a copper cold head inserted in a small cell containing the argon (see Fig. 5.9 for the detailed view). The cold head is connected to a pulse tube which is operated by the compressor. The whole sub-system is contained in a double wall dewar and it is hanged to the pole above the dewar containing the TPC (see Fig.5.7).

- **Compressor:** it cools down the cold head exploiting helium pressure variations. It is a PT90 pulse tube coupled with a CP2850 that has a cooling capacity of 90 W at 80 K, both by Cryomech [98].

- **Dewar:** is a double wall dewar to host the TPC immersed in liquid argon. The thickness of the walls varies with heigh to minimize the amount of steel at the TPC nominal position. The internal diameter at the bottom is $\sim$13 cm, but in enlarges and at the top is closed by a CF250 flange in order to host all the feedthroughs. It attached to the pole, just below the condenser.

- **Gas panel:** it allows the user to control the valves and the mass flow controllers in order to operate the system in different regimes.

- **Recirculation pump:** it is used only in the recirculation phase to pump the argon gas evaporated from the dewar again to the condenser.

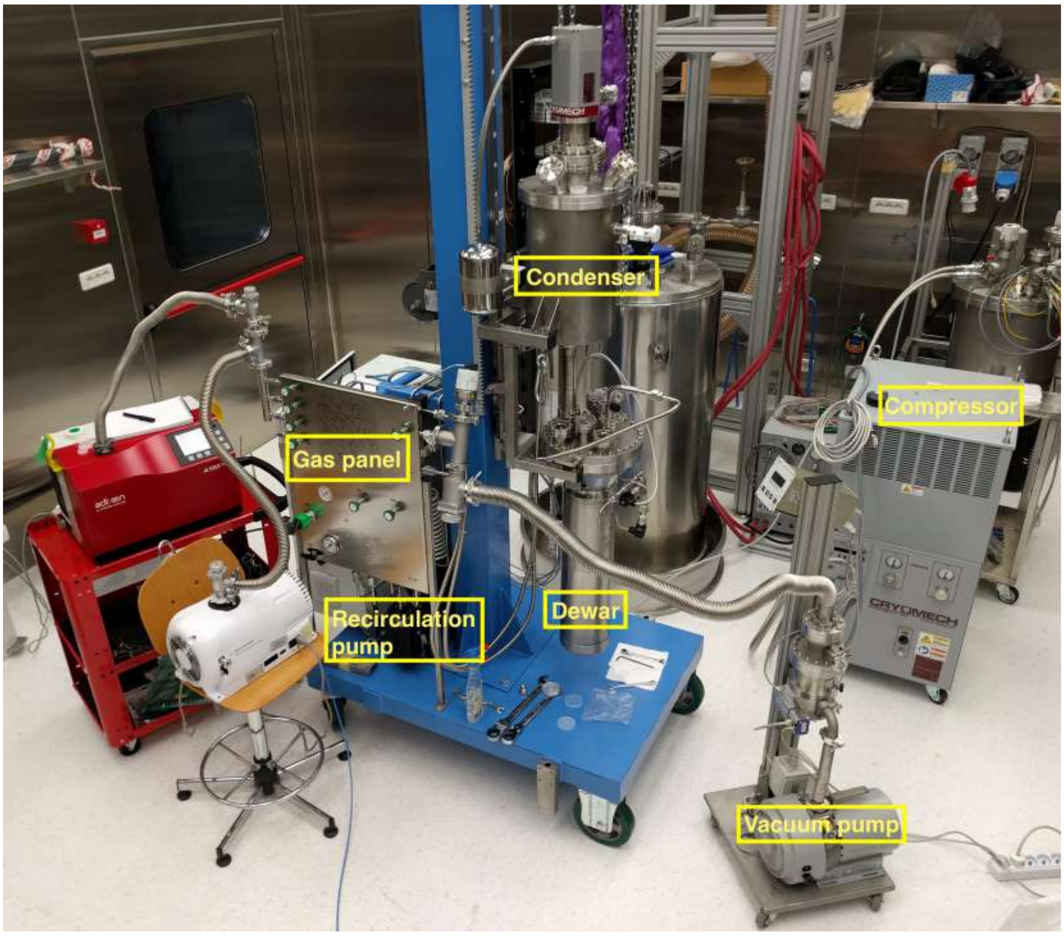

Fig. 5.7 The picture shows the entire cryogenic system mounted in the Naples clean room during the commissioning phase. The condenser and the TPC dewar are attached on the pole. On the left on the cart there is the gas panel, with below the recirculation pump. On the right there is the compressor, not yet attached to the pulse tube at the top. Two pumping stations for the vacuum are present, one on the right and one on the chair.

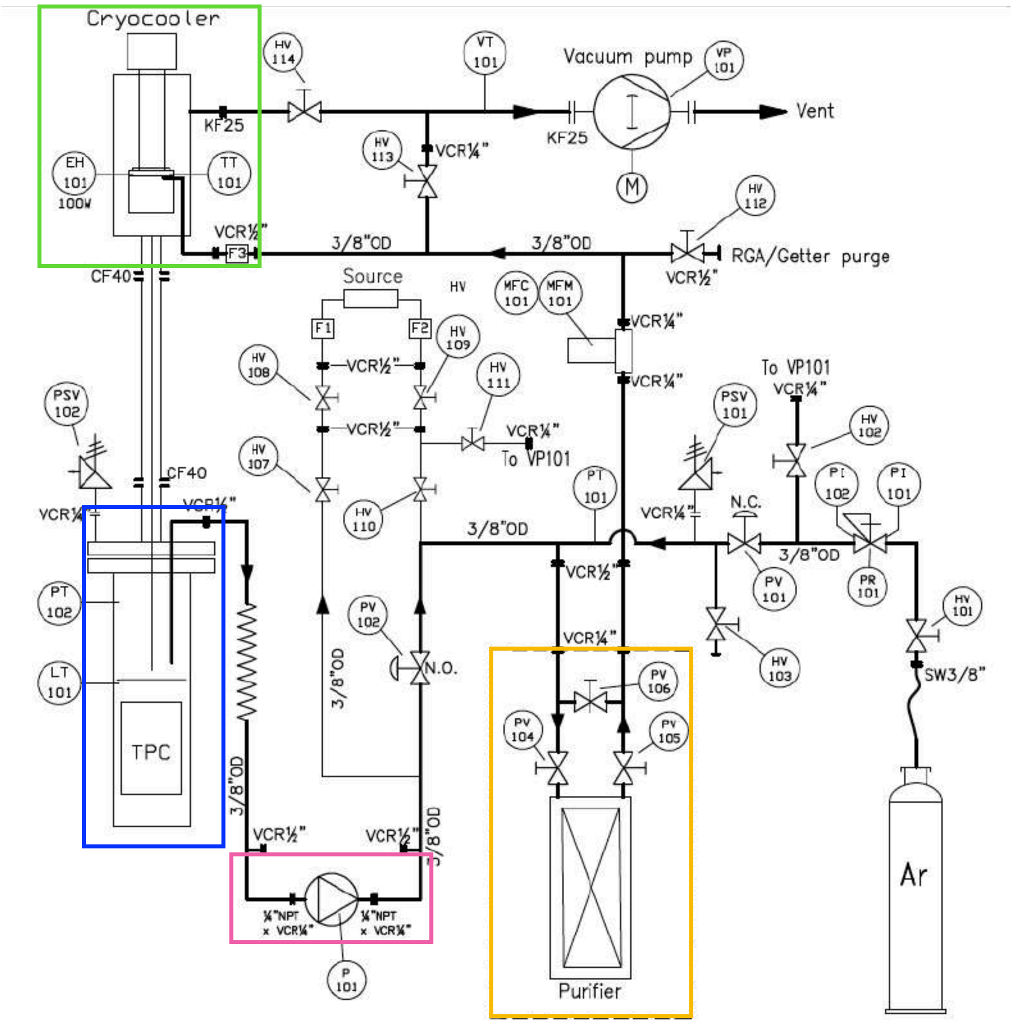

Fig. 5.8 Cryogenics "P&ID" diagram. In the green frame the condenser, attached to the TPC cryostat surrounded in blue. The magenta frame contains the recirculation pump, that is switched off during the filling phase. The orange box highlights the getter purifier.

- **Getter:** it is basically the argon purifier. Gas argon flows through it and the heated getter material forms irreversible chemical bonds with any oxide, carbide and nitride impurities [99]. It can be by-passed if needed.
- **Electric panel:** it is a semi-automatic control system, designed and realized by Omicron, that can be remotely operated communicating through an ethernet port.
- **Displacement system:** it is the light blue part in picture 5.7. Is is made up by a a cart with wheels and a pole equipped with a manual winch to displace the dewar, and consequently the condenser, at different heights.

As far as the operating principle is concerned, the system has been designed to work in two different ways: during the filling and during recirculation. Let's examine the crucial phases by following the "P&ID" diagram shown in figure 5.8. Before entering the gas in the apparatus a preliminary phase of pump and purge is required: for technical runs we consider sufficient a vacuum of the order of $\sim 10^{-3}$ mbar. In filling mode the argon gas is gradually introduced into the system from the bottle at room temperature. Then it enters the condenser - surrounded in green in figure - where it is cooled down by contact with the copper cold head. The custom made ReD cold head has a "comb structure", as can be seen in figure 5.9, to maximize the contact surface between metal and argon. The golden part couples the pulse tube with the cold head itself; it also contains a temperature sensor and a heater, in order to control the cooling power through a feedback mechanism. After this the gas passed into the dewar, surrounded in blue in figure, through a vertical bellow. Consequently, by circulating gas at an increasingly lower temperature, all the components are cooled until the beginning of the actual liquefaction phase. After the cooling of the TPC cryostat, liquid argon starts to accumulate and the level grows. This phase from the first gas insertion to a liquid level of $\sim$ 30 cm takes about 12 hours, taking into account the thermal load of the TPC, the SiPMs and all the cables.

Once the TPC dewar is filled with liquid argon the recirculation phase can start. The liquid argon boils and evaporates at the surface, the vapour is pushed by the recirculation pump - surrounded in magenta in figure - and passes through the getter, surrounded in orange in figure. After the purification it is inserted again in the condenser cell and re-liquefied. This process takes place at equilibrium, whereby the level of liquid argon remains almost constant. To monitor continuously the liquid level two Pt1000 RTDs are mounted at two different heights ($\sim$1.5 cm between them) and the liquid level is maintained in between. All the crucial thermodynamic parameters are monitored by the slow control software exploiting the Omicron system. Since the system is operates as a closed loop, with in the course of time the level of argon purity improves, consequently there is a greater lifetime of the drifted electrons. In addition to using the getter in the recirculation phase, it is essential to try to introduce the least possible amount of impurities in the system. For this Argon 6.0 is used and all the components of the apparatus placed inside the dewar have been previously cleaned in a dedicated ultra-sonic bath.

5.4 Beam and Si-telescope

The ReD experiment is located at LNS in order to produce the neutrons with the Tandem accelerator. As explained in section 4.2.1, we exploit the reaction $^7Li + p \rightarrow ^7 Be + n$, in

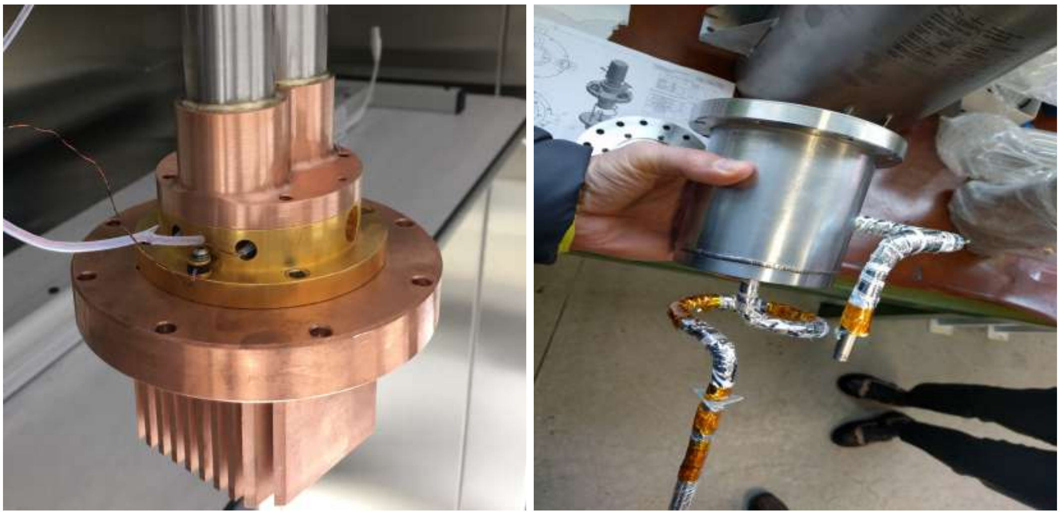

Fig. 5.9 A detailed view of the condenser: *on the left* you can see the copper cold head with its characteristic "comb structure" and *on the right* the cell. The argon gas enters from the side and exits liquefied from the bottom.

inverse kinematic to have a collimation of the neutrons. After the production of the ^{7}Li ions, explained in the following section 5.4.1, the beam is delivered in the 80° line where our apparatus is mounted. On the line there is a cylindrical scattering chamber containing CH_2 targets for the neutron production and three silicon detectors to tag the associated particles. Two of these detectors are assembled in a telescope configuration to perform particle identification through a ΔE-E measurement. The third one is placed in a different position to monitor indirectly the beam current. The Tandem is also the ideal accelerator to perform measurements at different energy values, as the preparation times of a beam and of energy variation are very rapid; this allows to have neutrons of different energies even during the same data taking campaign [100].

5.4.1 Tandem and scattering chamber

The Tandem is a type of electrostatic accelerator, which has two-step acceleration of ion particles with one high voltage terminal. A beam of negative charged particles, produced with a sputtering ion source, is injected from a relatively low voltage platform, that allows to reach a maximum injection energy of 450 keV towards the high voltage terminal, with a positive voltage, which at LNS can reach up to 14MV. Inside the terminal, the beam impinges on a thin metal foil (of the order of $\mu g/cm^2$), often carbon or beryllium, stripping electrons from the ions of the beam, so that they become cations. The charge transport system and the accelerator column must work in an environment saturated with high pressure SF6 insulating

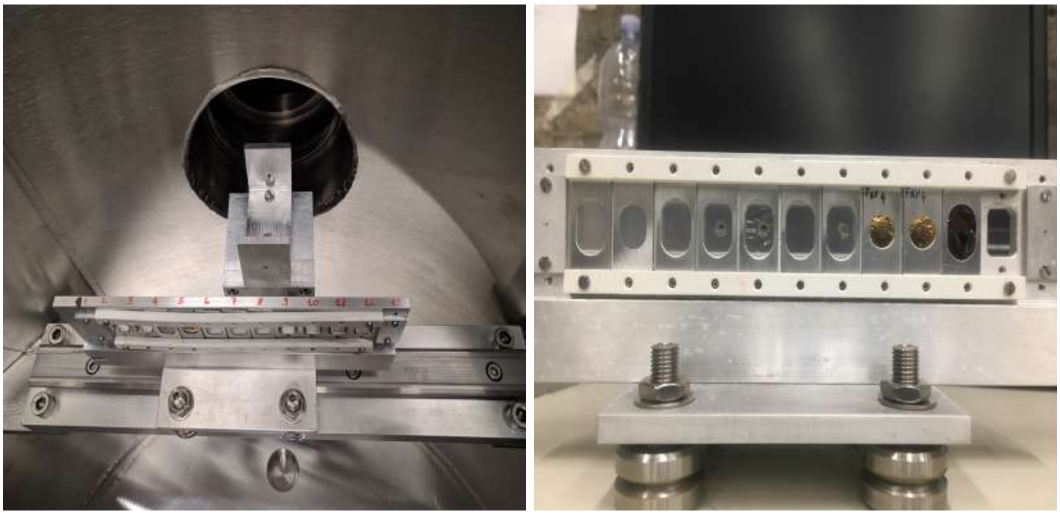

Fig. 5.10 *On the left:* the two-step collimator placed before the CH_2 target to have a more defined beam spot. *On the right:* the holder for the different targets which can be changed without opening the scattering chamber. From left to right CH_2 of different thicknesses, Au and C for calibrations.

gas, in order to prevent possible discharges due to high electrical potentials. For this reason, the Tandem is located inside an iron tank of about 300 cubic meters, capable of supporting a gas pressure higher than 9 atm.

The highly charged positive ions are accelerated again through a high energy accelerator tube down to the exit. As it is difficult to make anions of more than -1 charge state, then the energy of particles emerging from a tandem is $E = (q+1)V$, where V is the voltage of the terminal, and q is the positive charge of ions emerging from the stripper foil [101]. For a ^{7}Li beam, that has q=3, the maximum energy that could be reached is 56 MeV, but for ReD it is sufficient to stay between 18 MeV and 34 MeV. The maximum current ranges from 10 nA to 200 nA typically.

The continuous lithium beam is delivered on the 80° line, that as been entirely dedicated to ReD by the LNS Scientific Committee to allow a stable set up. Immediately after entering the scattering chamber the beam encounters a two step-collimator, show in figure 5.10 on the left, that has a 2 mm diameter hole followed by a 3 mm diameter one. Between the two is placed a metal shield, not shown in the picture, to avoid any possible spurious contribute due to interaction with the collimator it self. After the collimator there is a movable target holder, as it can be seen in figure 5.10 on the right, that can be displaced from outside without breaking the vacuum. Using this tool we can change the target thickness, put in place a new target if one becomes worn, use different materials to perform calibrations.

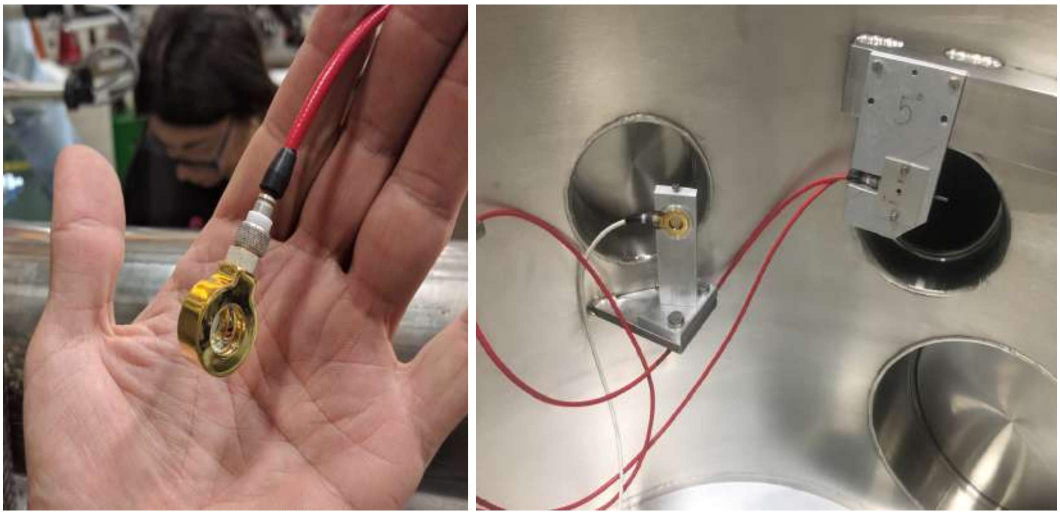

Fig. 5.11 Silicon telescopes in the scattering chamber

5.4.2 Silicon detectors

As the Tandem cannot be operated in pulsed mode, it is crucial to have a trigger signal. The detection of the charged associated particle, in out case the ^{7}Be will provide the start for a time-of-flight measurement of the scattered neutron. For this purpose within the scattering chamber, at 5° from the beam line and at 46.5 cm from the target, is placed the so-called Si-telescope. It consists of two circular silicon detectors -l ike the one in figure 5.11 on the left - of different thickness, placed one behind the other. The thin one that measures the ΔE, is the first encountered by the incoming particle, while the thick on is behind. In the ΔE-E telescope, the loss of energy and the total energy of the incident particle are measured and this technique is applicable when particles pass through the first detector and are stopped in the second one. The partition of energy between the two detectors is different for different particles, because of the different stopping powers, so it is possible to trace the charge or mass of the particles through the Bethe-Bloch relationship. During the first two runs, in June and July 2018, we used a 200 μm thick detector for the E measurement and a 20 μm one for the ΔE, both form the ORTEC Company. In September we decided to add a third detector, placed at 23° with respect to the beam line, in order to better detect the elastic scattering on Au and C to monitor the beam current. So the configuration adopted during September run, was the following:

- E measurement: 1000 μm detector;
- ΔE measurement: 20 μm detector;
- current monitoring: 200 μm detector.

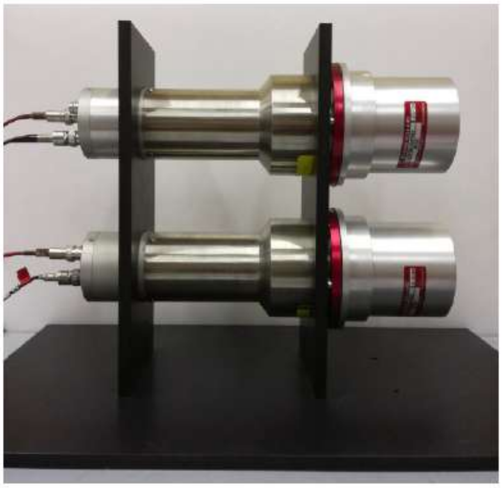

Fig. 5.12 Two of the nine neutron detectors used in the n-spectrometer. The 3"×3" cylindrical cell containing the liquid scintillator extends from the right to the red metal ring, then starts the PMT.

In front of the Si-telescope to protect the sensitive area, that is of 50 mm^2, from eventual radiation damage, we placed a collimator consisting in a a thin aluminum plate (2 mm thick) with a 3mm diameter hole.

Just outside the chamber there are three compact ORTEC-142 pre-amplifiers, on for each detector, that have two output signals: one with very fast rise time, to perform timing measurements and the other, slower, to have a better resolution on the energy. Through the same device we also provide the bias voltage to the silicon detectors. We send the fast signals to a fast amplification NIM module and then to a CAEN DAQ board, in order to generate the trigger signal; the slow signals on the contrary are sent to a different amplifier and do not take part to the trigger formation.

5.5 Neutron detectors

The neutron spectrometer - used to tag the scattered neutrons - consists of an array of nine liquid scintillator based detectors coupled with photomultiplier tubes (PMTs), mounted on a custom made structure to select the desired scattering angles. Each detector, produced by the SCIONIX Company, consists of a 3"×3" cylindrical cell containing the liquid scintillator, coupled with a 3" ETL 9821 photomultiplier (See figure 5.12)[102]. The organic scintillator mixture that is the commercial EJ-309, from Eljen Technology. The cocktail is often used to detect neutrons with energies of few MeV, especially because of the very good neutron–gamma discrimination capability [103, 91]. It also has a good scintillation yield

Fig. 5.13 *On the left:* the support structure to place the detectors at different φ_{LSci} angles. *On the right:* the LScis mounted on the "wheel".

of 12300 photons/MeV, a decay time of 3.5 ns and a maximum emission wavelength of 424 nm. The PMTs are fast enough to measure the time of flight with a precision of the order of nanoseconds and have a 30% quantum efficiency. For sake of simplicity in the following I will refer to the entire detector, meaning the scintillator cell and the PMT, with the abbreviation LSci. All the nine LScis have been tested preliminary in Rome, in particular the gain has been checked and equalized. To have more detailed information, also about the linearity of the response and the resolution, refer to [104].

As explained in section 4.2.1, eight of the nine neutron detectors need to be placed on a circumference that is the basis of a cone centered on the target-TPC direction and with the vertex in the center of the TPC liquid volume. The semi-opening angle, that corresponds to the neutron scattering angle θ_n, is 36.8°. The holding structure, the so-called "LScis wheel" would allow simultaneous detection of scattered neutrons corresponding to a fixed recoil energy, but the LScis placed at different φ_{LSci} can distinguish between different Ar recoils directions with respect to the electric field. Eight of the detectors are positioned in this configuration at 80 cm from the TPC center, while the ninth- is devoted to the low energy measurement (see section 4.2.1) and consequently is in a peculiar position. In particular it is not located on the described circumference, but in the lowest position of the central ring of the holding structure, at 97 cm from the TPC center. Finally between the target-TPC direction and the target-LSci$\emptyset$ there is a $\sim 1.7°$angle.

5.6 Slow control system

All the detectors described in the previous sections are operated remotely by means of a slow control system that allows the user simple operations, such as switching on and off an instrument, via a Graphical User Interface. Furthermore, slow control has the crucial function of monitoring the fundamental parameters of each component of the experiment, making them visible to the shifter and saving them on a database. From the hardware point of view, the system is based on a NI-PXIe-8840 controller with Intel Core i7, Windows 10 64 bit and a 8 GB/s bandwidth [105]. It also has 6 USB ports, 2 ethernet, 1 serial, 1 GPIB and 2 HDMI. All the instruments handled by the slow control are listed in table 5.2 with the respective communication protocol. All the software is written in Labview and each singular instrument is piloted by its stand alone application. A top monitoring application is used to collect and display the most relevant parameters of the detectors in a synoptic graphical user interface.

Instrument	Function	Communication
Criotec system	Cryogenics monitoring	Ethernet
Lakeshore 336	Temperature monitoring	GPIB
CAEN SY 5527 : A1539P	SiPMs bias voltage	Ethernet
CAEN N1470	TPC electric fields	USB
Keithley 2280S	Gas pocket bubbler	USB
CAEN N1471	Si detectors bias voltage	USB
CAEN SY 5527 : A7236	LSci power supply	Ethernet
Agilent 32250A	Laser trigger	Serial

Table 5.2 All the instruments controlled remotely with the Labview-based slow control system.

5.7 Data acquisition system

The data acquisition system (DAQ) is based on three CAEN V1730 Flash ADC boards, each with 16 channels. The boards have a 14-bit resolution, a $2V_{pp}$ input range and a 500 MHz sampling rate [106]. The total number of signal output channels is 42, of which 9 for the LSci, 28 for the SiPMs and 5 for the Si-detectors in the scattering chamber. When all the detectors were fully operating a data rate of 40 MB/s was achieved, limited by the obsolete disk which was mounted in the DAQ server. The DAQ software is a re-engineering of the PADME experiment code which allows you to select the data acquisition conditions through a graphical interface. Typically the main changes depend on the configuration of the TPC:

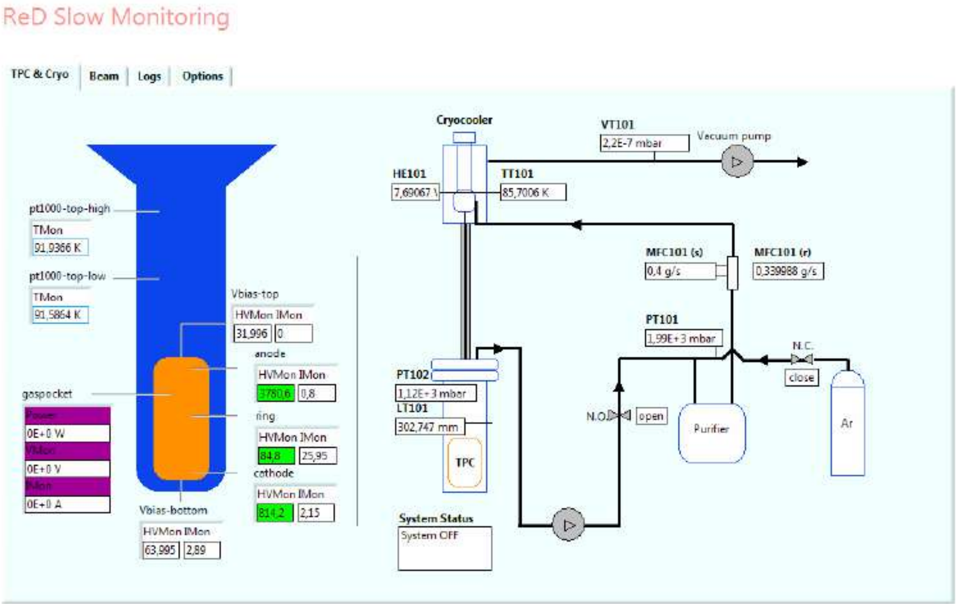

pt1000-top-high TMon 91,9366 K

pt1000-top-low TMon 91,5864 K

gaspocket Power 0E+0 W VMon 0E+0 V IMon 0E+0 A

Vbias-top HVMon 31,996 IMon 0

anode HVMon 3780,6 IMon 0,8

ring HVMon 84,8 IMon 25,95

cathode HVMon 814,2 IMon 2,15

Vbias-bottom HVMon 63,995 IMon 2,89

HE101 7,69067 \

TT101 85,7006 K

VT101 2,2E-7 mbar

MFC101 (s) 0,4 g/s

MFC101 (r) 0,339988 g/s

PT101 1,99E+3 mbar

PT102 1,12E+3 mbar

LT101 302,747 mm

N.O. open

N.C. close

System Status System OFF

Fig. 5.14 screen shot of the Graphical User Interface synoptic display which shows all the crucial parmetrs of the system.

when it is operated at null fields, avoiding the production of S2, the acquisition window is 20μs long of which 6μs of pre-trigger, when instead there is also the scintillation signal the window must be longer. It was decided to acquire standard S1+S2 events in a window of 100μs, with a pre-trigger of 10μs.

Digitized waveforms are recorded on the base of a hardware trigger generated by the coincidence of some channels above threshold. The propagation of the trigger to all the boards was performed passing through an external NIM module, that was also used to switch to an external trigger given by the laser during the TPC calibration runs. For the directionality measurement the best trigger condition would be the triple coincidence between the Si-telescope, the TPC and one of the eight LScis. Instead during the three technical runs performed in 2018 we tested two trigger schemes, based on a double coincidence within 200 ns: one looking for coincidences between the Si-telescope and any of the eight LSci, acquiring the SiPMs in slave mode, the other triggering on the coincidence between the Si-telescope and the TPC, acquiring the LScis in slave mode.

Finally a custom made reconstruction code, called "red-daq-light”, is used to generate root files form the binary raw waveforms and also to perform low level analysis, for example calibrating the standard runs with the single photo-electron response obtained with laser runs.

5.8 Alignment

As already widely discussed in section 4.2.1 for the ReD experiment it is crucial to position the various components of the apparatus according to a precise geometric construction. Since most of the system, TPC with cryogenics and scintillators wheel, is out of axis with respect to the lithium beam, it has not been possible to use the standard methods usually adopted at LNS. As a result we had to develop an custom procedure, which also took into account all the logistical limitations due to the limited spaces on the 80° line. Another difficulty encountered in designing alignment is due to the fact that during the mounting phase the TPC is closed inside the dewar, so it is crucial to report outside its position. The procedure I will describe does not include the placement of silicon detectors, which has been independently cured.

The procedure is exclusively mechanical, based on the positioning of different plates starting from the projection on the floor of the beam line and of the position of the target. The templates used have been laser cut to obtain the necessary precision. As I will discuss in the following the procedure is quite delicate, therefore, although on the dimensions of the templates the uncertainties are submillimetric, the final positioning of the objects is granted with an accuracy of the order of centimeter.

Let's briefly go though all the passages [107].

1. The preliminary step was to project the beam line on the floor, using LNS standard methods.
2. While the scattering chamber was still open, we mounted the first template (which is not shown in figure) across it, to identify the target position. From this template we lowered a plumb line, passing through one of the bottom flanges of the chamber, projecting the ^{7}Li interaction point on the floor. Then it was possible to remove the template and close the chamber.
3. We fixed to the floor with metal dowels the second template (orange in figure 5.15), placing the vertex on the target projection and the straight side along the beam line previously traced.
4. To check the vertical TPC position with respect to the top flange we simply used a meter and a bubble level.
5. The TPC position on the horizontal plane with respect to the dewar flange is fixed by mechanical constraints, but it is crucial to know it when the dewar is closed, in order to align the dewar itself with the rest of the apparatus. Since the TPC is hanged with four fiberglass rods, inserted in four holes on the internal face of the flange, by

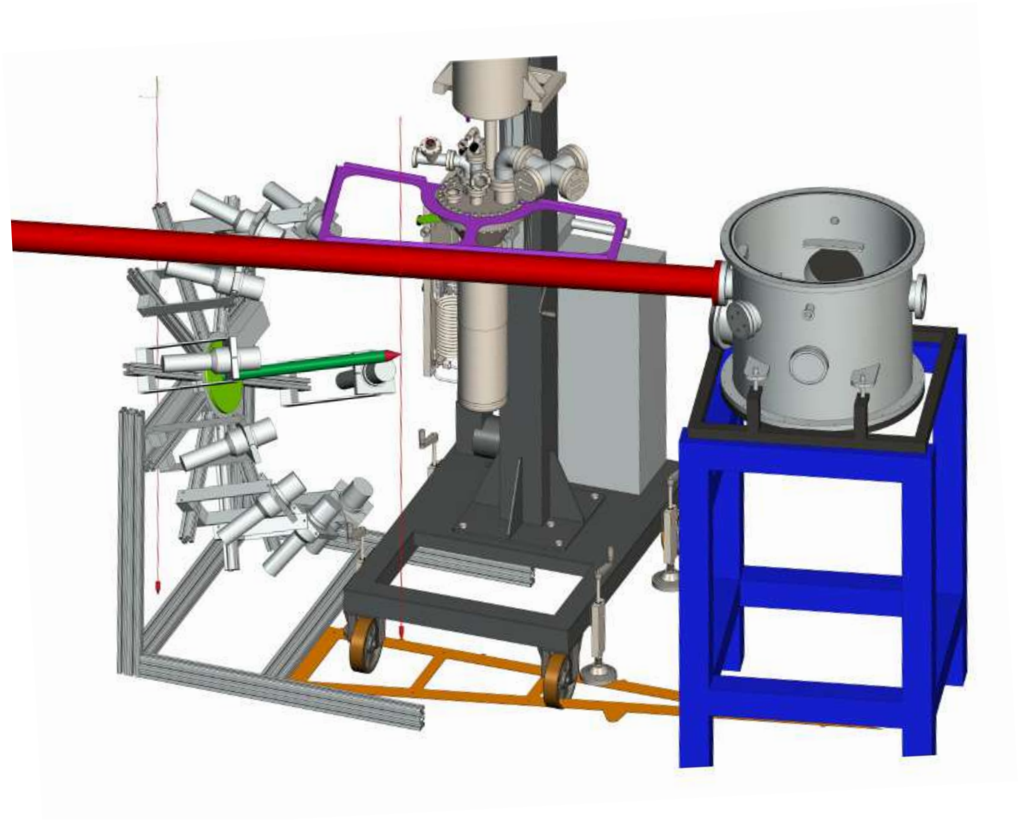

Fig. 5.15 Alignment procedure: final step

measuring the holes position we are able to know the TPC orientation. We reported on the external part of the dewar flange the holes angular position, in order to know the TPC position with respect to the cart.

6. When the dewar was closed and fixed to the pole we mounted the third template, the pink one in figure 5.15.
7. The trolley was positioned by aligning the pink template with the orange one using four precision plumb lines. Then it was fixed to the floor with metal dowels.
8. The TPC was brought to the correct height by adjusting the flange through the handling gear integrated in the Criotec system.
9. We cross-checked the LSci orientation on their support structure, where they were mounted using a protractor, exploiting a fourth template not shown in the picture. We fixed the crossbar of the base of the wheel at the proper distance.
10. The centering device (green in figure 5.15) is positioned on the structure of the PMT and it is fixed with clamps.
11. The entire LSci support was then positioned placing the crosspiece in contact with the base of the orange plate, as shown in the figure. A further check is performed dropping a plumb line from the pink template and passing exactly on the centering tool tip. The LSci wheel was fixed to the floor with metal dowels as the rest of the apparatus.
12. Any vertical tilt of the LSci structure was checked with a bubble level and the fourth template, which is made in such a way that when it is positioned on the lowest LSci its upper side must be horizontal.
13. The correct height of the PMT support was checked compared to the TPC by measuring the distance between the centering tool tip and the pink plate.

Chapter 6

ReD: preliminary results

During 2018, while the whole apparatus was under commissioning, several tests and calibrations were performed, at Laboratori Nazionali del Sud (LNS) in Catania and, for what concerns the TPC, also at Univeristà degli studi di Napoli Federico II, in Naples.
Before installing the setup on the beam line in Catania, we also performed many "first time tests" in Naples during April and May, since we had three brand new devices to test. In this phase of the experiment we assembled and integrated the cryogenic system, we operated the TPC for the first time, both in single and double phase, and we did a very preliminary characterization of the SiPMs, that had never been tested in liquid argon before. Even if not conclusive, all the tests had a positive outcome and this allowed us to move at LNS to proceed with the full commissioning.
We carried out three technical runs "on beam" at LNS: the first two between June and July and a third one at the end of September. The main purposes of these data-taking campaigns were to separately characterize the various detectors separately, to test the integration and the alignment of the system and to verify the ^{7}Li beam conditions. After the first run in June, that was devoted to preliminary checks on the apparatus, we operated the full system during the July measurement. Finally the September run was dedicated to the beam characterization, with special attention to its intensity and divergence.
After the third beam run, the TPC and the cryogenics were sent back to Naples to deepen the characterization of the detector, in particular to optimize the electric fields configuration to allow a detailed study on the ionization signal. The data-taking is still on-going at the moment of writing.
In this chapter I briefly summarize the first calibration results acquired both in Naples, during the TPC characterization campaigns, and in Catania, during the technical runs. All the results reported are preliminary, since the analysis is still on-going and there are many open questions.

6.1 TPC characterization

The characterization of the ReD TPC occurred in several phases of the experiment and led to various improvements and optimizations of the detector, currently still underway. In this session I will report the most significant results of the tests carried out until now, even if not conclusive.

During the data acquisition campaigns, the TPC was operated mainly in two different ways: in single phase at null electric fields and in double phase with standard fields (See Tab. 6.1)

SiPM over voltage	Phase	Bubbler power	Electric fields
7 V	single	-	NULL
7 V	double	$\sim$1 W	Drift 200 V/cm Extr. 2.8 kV/cm Elect. 4.2 kV/cm

Table 6.1 Reference settings for the two standard TPC configurations.

In addition to these configurations, we started studies on the photodetectors response varying the over voltage and we tested different electric fields combinations, in order to deeply understand the chamber behaviour.

To get a rough idea of the signals shape, in figure 6.1 you can see the raw waveform of a scintillation event acquired with the TPC in single phase during a calibration with an ^{241}Am source. The unit on the x axis is ADC samples, which need to be multiplied by two to have time in nanoseconds, since we acquire at 500 MHz. The top plots show the signal for the two tiles separately, the bottom one shows the sum of the two.

6.1.1 Single electron response

To calibrate the Single Electron Response (SER) of our SiPM tiles we used the Hamamatsu laser diode PLP-10, which emits pulses 50 ps long, with a wavelength of 403 nm. The light was inserted in the dewar through a bunch of optical fibers and then it was diffused by the acrylic windows. The spectrum in charge of each channel is fitted with an appropriate sum of independent gaussian distributions (see Fig.6.2). The peak values in ADC counts, which correspond to the number of photoelectrons, are then linearly fitted and the angular coefficient is what we consider as the value of SER. The SER values are used to normalize, channel by channel, the spectra obtained in physical runs. This procedure is repeated every few hours to check the stability of the detector, enabling an external trigger synchronized with the laser emission. Monitoring the SER values over long periods of time, of the order of few months, we observe a quite stable behaviour, except for some anomalous "jumps" in

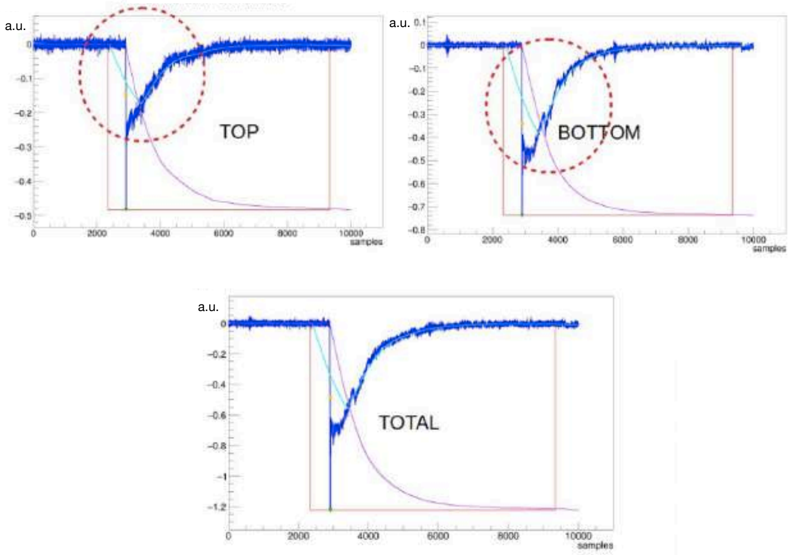

Fig. 6.1 Example waveform of a scintillation event in liquid (S1) acquired during an ^{241}Am calibration run. In the top left plot you can see the summed signal af all the top SiPMs, while on the right the bottom tile signal. The bottom plot shows the total raw waveform.

certain channels, as you can see in figure 6.3. The cause of these variations is currently under investigation and probably it is related to a noise component associated with laser runs.

6.1.2 S1: light yield and resolution

In order to characterize the scintillation signal, S1, we used an ^{241}Am source that undergoes α-decay emitting a 59.5 keV γ-ray. Fitting the americium peak we obtained the light yield of the chamber; looking separately to the top and bottom tile we also studied the response of the two different arrays. In Naples, after the re-evaporation of the TPB on the internal surface, we obtained 11.3 PE/keV for the whole TPC in single phase configuration with standard over voltage. Fitting separately the charge spectrum for top and bottom we obtain respectively 5.7 PE/keV and to 5.4 PE/keV. In figure 6.4 you can see the americium spectrum for the two tiles and the total one, the bottom resolution is slightly worse than the top, probably because of a noise issue related to the bottom FEB. This light yield value, obtained directly dividing the mean value of the ^{241}Am peak by the corresponding energy, does not take into account all the correlated noise components discussed in section 5.2. In order to have an estimation of the noise contribution we try to analyse our data following the Vinogradov's model (See Ref. [108] for all the details). From the SER deviations with respect to the expected Poisson distribution it is possible to evaluate the correlated noise, which is parametrized by a

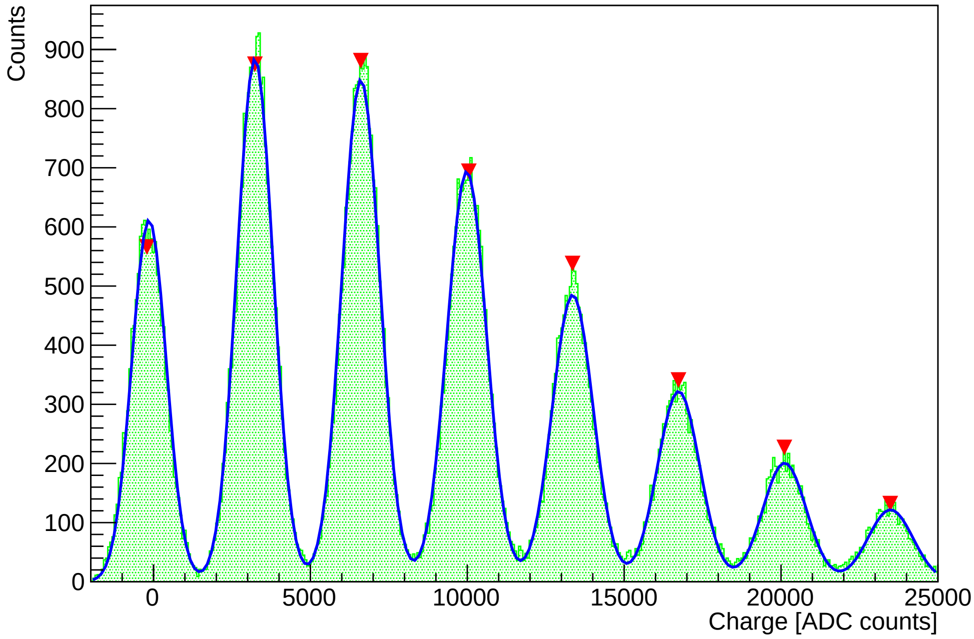

Fig. 6.2 Charge spectrum for one of the bottom tile channels, acquired during a laser run with the TPC in single phase at null fields. The blue line is the fit performed with independent gaussian distributions. The red triangles indicate the peak values used to perform the linear fit, in order to get the SER for the channel.

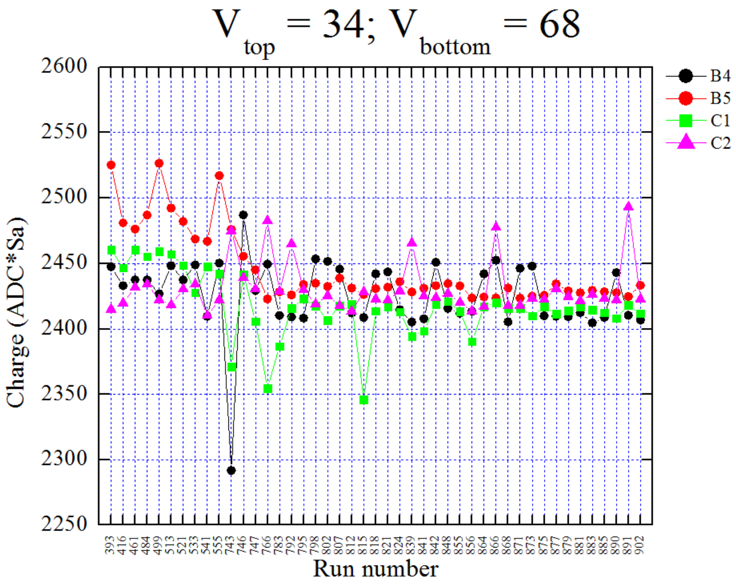

Fig. 6.3 Single electron response stability for four channels of the top tile. The value can be considered sufficiently stable, except for some peaks which may be due to some noise correlated with the laser.

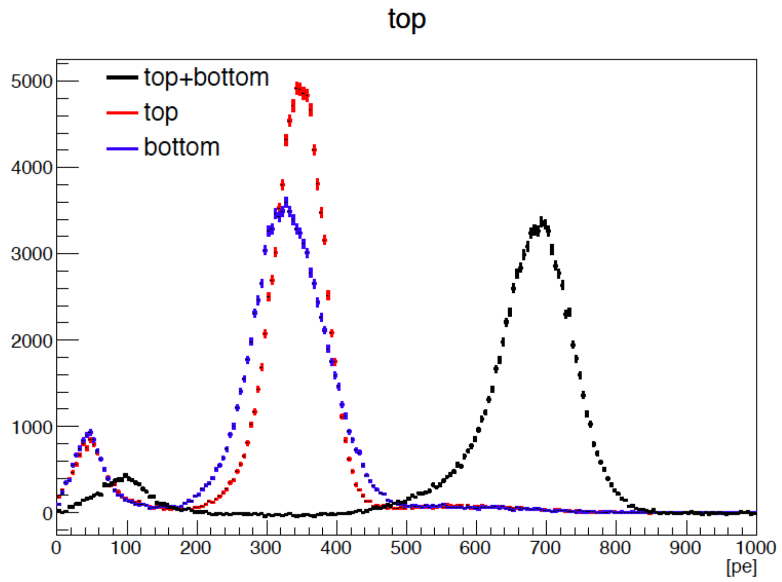

Fig. 6.4 Charge spectrum acquired during a calibration run with an ^{241}Am source, while the TPC was in single phase configuration. In black you can see the total charge response converted in photoelectrons, in red and blue the top and bottom separate signals.

coefficient of duplication, denoted as K_{dup}. This leads to the definition of the so-called net light yield, which is the LY extracted from the ^{241}Am peak, denoted as LY_{gross}, normalized by the number of effective PE per one real PE:

$$LY_{gross} = \frac{\mu_{Am}}{E_{Am}} \qquad LY_{net} = \frac{LY_{gross}}{1+K_{dup}} \tag{6.1}$$

Moreover it can be useful to introduce the so-called Fano factor, that can be related both to the ^{241}Am peak, the so-called effective Fano factor, and to the K_{dup}, as follows:

$$F_{eff} = \frac{\sigma^2_{Am}}{\mu_{Am}} \qquad F_{exp} = 1 + 2 \cdot K_{dup} \tag{6.2}$$

What we observed is that the effective Fano factor and the one expected form the SER obtained with laser calibration are not in agreement. Furthermore we performed a scan in over voltage in order to better characterize the LY and the resolution and we found out that increasing V$_{bias}$, we observe a clear amplification of the LY in the energy scale, but not on the resolution. These results, summarized in table, are under investigation, but could be related to an unexpected contribution of correlated noise. A possible explanation is that the Vinogradov theory could model correctly the afterpulsing, but not the cross talk, so the LY has an artificial increase due to the cross talk that we do not take into account. This seems to be confirmed by the fact that the cross talk grows linearly with the over voltage, but we are going to run a detailed electronic simulation of the devices in order to better clarify this point.

OV (V)	μ_{Am} (PE)	σ_{Am}	K_{dup}	LY$_{gross}$ (PE/keV)	LY$_{net}$ (PE/keV)	Resolution	F_{eff}	F_{eff}
5	505.75	37.93	0.19	8.50	7.14	7.50 %	2.90	1.38
6	559.30	40.83	0.27	9.40	7.40	7.30 %	3.10	1.54
7	672.35	49.75	0.40	11.30	8.07	7.40 %	3.70	1.80
8	773.50	56.47	0.55	13.00	8.39	7.30 %	4.20	2.10

Table 6.2 Preliminary analysis of the TPC light yield in single phase, based on the Vinogradov model.

6.1.3 Pulse Shape Discrimination

In order to understand the Pulse Shape Discrimination (PSD) performances of the TPC, we carried out a calibration campaign using a ^{252}Cf neutron source and we compared the data with a very simple model to optimize the separation between electron and nuclear recoils events.

Studying the single photoelectron raw waveform we found that SPAD recovery time is $\sim$ 0.5 μs which is comparable to the argon triplet time constant τ_t= 1.5μs (See Sec. 2.1.2). This should yield to a prompt signal which is defined as the integral of the scintillation light during the first $\sim$850 ns. From the ^{252}Cf events we obtain that the best value for the PSD parameter is the scintillation fraction occurred in the first 700 ns, so we define in analogy with equation 2.18:

$$PSD_{tpc} = f700 = \frac{\int_0^{700ns} S1dt}{\int_0^{t_{end}} S1dt} \tag{6.3}$$

Further studies are required for a complete PSD_{tpc} optimization, but as you can see from the plot in figure 6.5, the nuclear recoil events, induced by neutrons, and the electron recoil events are well distinguishable.

6.1.4 Drift time and e$^-$ lifetime

To evaluate the electron lifetime we analysed background events during double phase runs, which we assume to be uniformly distributed in all the TPC active volume. Figure 6.6 on the

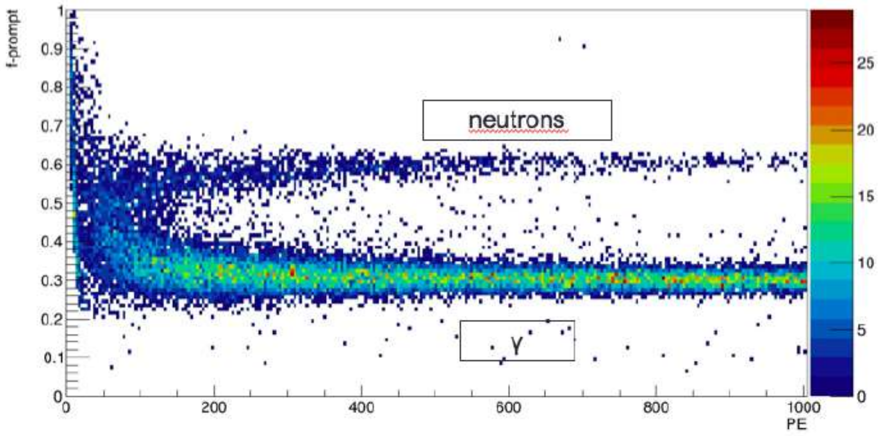

Fig. 6.5 Data taken during a TPC calibration with the ^{252}Cf source, to optimize the separation between nuclear and electron recoils. The PSD parameter, plotted on the vertical axis, is the scintillation fraction collected in the first 700 ns.

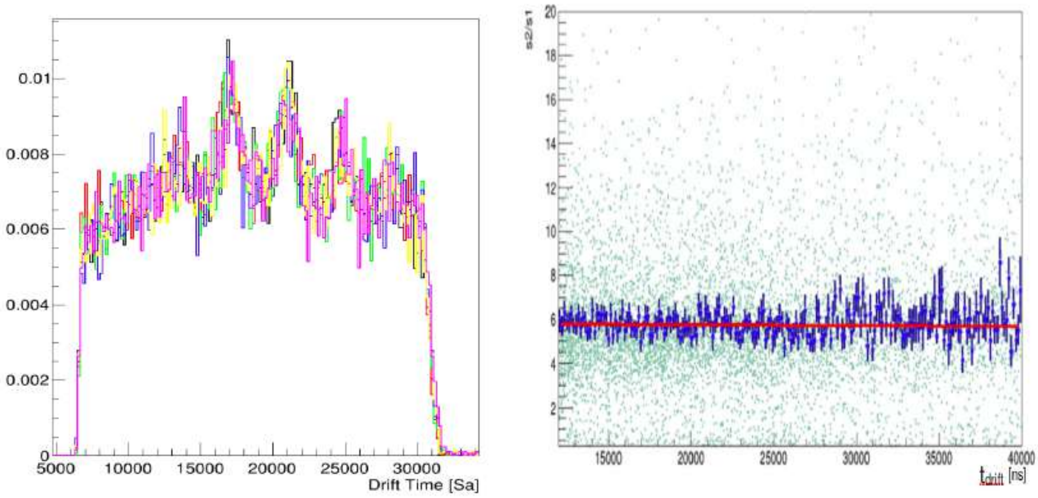

Fig. 6.6 Drift time measured in ADC samples

left shows the drift time distribution in ADC samples, which have to be multiplied by two to obtain time in nanoseconds. The different coloured lines in the plot correspond to different power values give to the bubbler that forms the gas pocket. As expected the distribution is flat, but the cut-off that indicates the maximum drift time is at $\approx 62\mu$s. This value, considering the TPC geometry, leads to a drift velocity v_{drift} = 0.8 mm/ μs, that is not compatible with v_{drift} = 0.93 mm/ μs that we would expect, also from the DarkSide-50 experience, having an electric filed of 200 V/cm.

In order to measure the electron lifetime we used S2/S1 mean ratio with respect to the drift time distribution, as can be seen in figure 6.6 on the right. Fitting the distribution with an exponential function, according to equation 2.15 we obtain a electron lifetime τ_l= 270 μs. This value, being much larger than the drift time, denotes a sufficiently good purity of the argon.

6.1.5 Hints on S2

The S2 signal characterization is just began at the moment of writing, so I will give some very preliminary hints on the first results obtained. As already stated before, the TPC was successfully operated in double phase and the S2 was observed. However we found a very low S2/S1 ratio compared to what we expected. Taking the DarkSide-50 value as a reference, since the standard electric field configuration is the same, we have to compare our ≈ 2.5 with ~ 30. This issue, together with the fact that the maximum drift field is longer than expected as highlighted in the previous section, could be explained by an actual electric field configuration different from the nominal, in particular the drift field seems to be $\sim$ 165 V/cm. Moreover we performed some run increasing the extraction and electroluminescence fields and we observed an improvement in the S2/S1 ratio. This fact would suggest that not all the drifted electrons are effectively extracted from the liquid.

These combined effects are not completely clear by now, but a we made a plausible hypothesis that could explain phenomena that we observe. Running a simulation of the electric fields for different liquid levels above the grid, it can be shown that a 1 mm thick extraction region (instead of the 3 mm thick quoted from the TPC design) is not sufficient to guarantee a uniform field. The absence of a defined extraction field would explain both the low S2/S1 ratio, as a fraction of the electrons is not ripped to the gas phase, and the lower drift field, because the leakage of the extraction field in the drift region would not be tuned. From the hardware point of view a 1 mm thick layer of liquid above the grid, which would mean a 1 cm thick gas pocket, could be caused by a tiny misalignment between the outlets of the gas in the TPC inner and outer walls. Anyway this needs to be checked, the S2 studies are on-going and we are confident that all the issues will be solved before the next run.

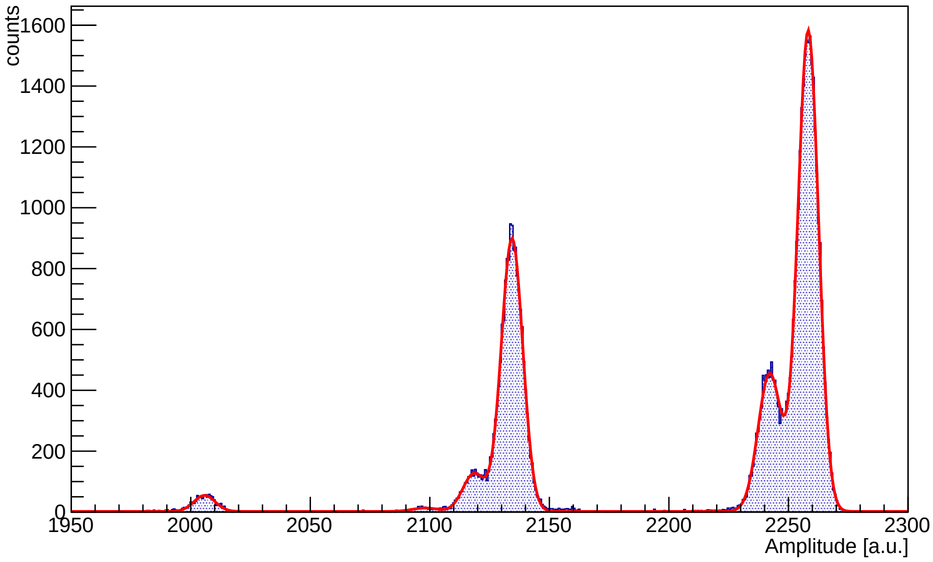

Fig. 6.7 Calibration of the 1000 μm thick Si-detector with the triple α-source. From left to right: ^{239}Pu, ^{241}Am and ^{244}Cm peaks. The peak values extracted from the fit (red line) have been used for the full energy calibration.

6.2 Silicon detectors and neutron detectors calibration

During the three data taking campaigns performed at LNS we characterized separately the silicon detectors and the neutron detectors. For a more in-depth analysis on the performance of LScis, based on previous measurements carried out in Rome, please refer to Ref.[104].

6.2.1 Silicon detectors

We performed an energy calibration of all the silicon detectors both with a low energy source and exploiting the ^{7}Li elastic scattering on an ^{197}Au target, at different beam energies. At low energy we used a triple α-source composed of ^{239}Pu, ^{241}Am and ^{244}Cm with emission lines between 5.1 MeV and 5.8 MeV. In figure 6.7 it can be seen the total spectrum for the 1000 μm detector, with superimposed the fit. This calibration, although it is not in the energy range of interest for the ReD measurements, was made to easily verify the status of the detectors in a preliminary phase. The measurement does not require to make the vacuum in the scattering chamber, nor to turn on the beam: in fact it is sufficient to place the sources in front of each detector inside the chamber. In this way it is also possible to optimize the grounding conditions of the pre-amplifiers to minimize electronic noise, avoiding having to repeat the beam line preparation procedure several times. We also exploited the Au target to

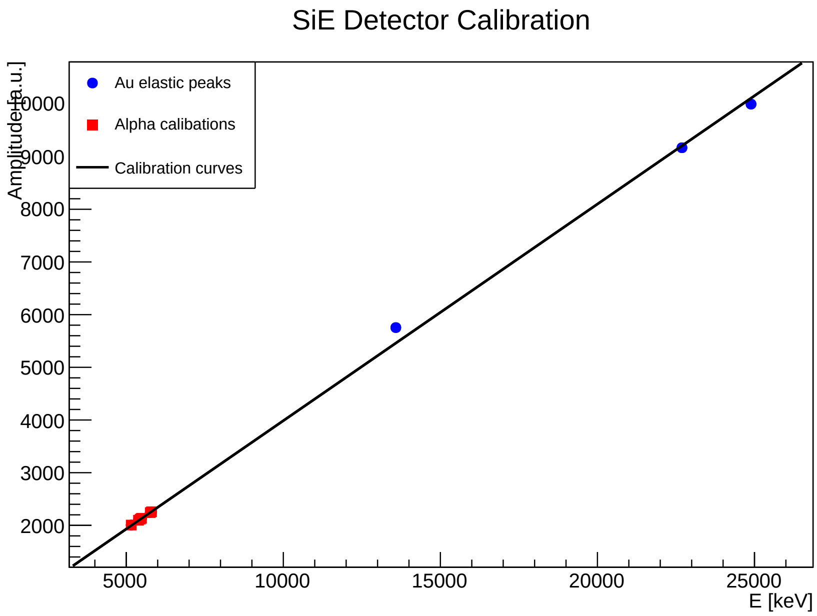

Fig. 6.8 Full calibration plot for the 1000 μm thick Si-detector. The low energy red points correspond to the peak values of the spectrum obtained with the α-source. The three blue points were obtained with the Au target and three different beam energies.

have a calibration at higher energy, in our region of interest, in particular we measured the ^{7}Li scattering peak at three beam energies: 18 MeV, 26 MeV and 28 MeV. In figure 6.8 you can see the full calibration again for the 1000 μm detector. The red points are obtained from the fit shown in figure 6.7, while the blue points correspond to the Rutherford scattering on Au. This procedure was replicated for all the three detectors, always using the slow signal coming from the pre-amplifier, which is better for energy measurements (see section 5.4). Finally we changed the target, selecting the CH_2 one, in order to test the beryllium tagging capability. In figure 6.9 it is shown a scatter plot of the E and ΔE signals which come from the two silicon detectors that form the telescope. This plot is obtained with no cuts and corresponds to a run acquired with very low trigger thresholds, to see all the different reaction products. Two main populations can be identified: the lower band corresponds to the scattered ^{7}Li, while the higher band with greater ΔE is the ^{7}Be. Looking to the ^{7}Be population two "blobs" can be seen, that correspond to the two allowed kinematics solutions for the ground state beryllium, while in between there are the ^{7}Be* events (see section 4.2.1 for the reaction details).

6.2.2 Neutron detectors

As far as the LSci are concerned, both studies on the timing and on the trigger efficiency have been made, as well as on the pulse shape discrimination. Using a ^{22}Na source, which emits

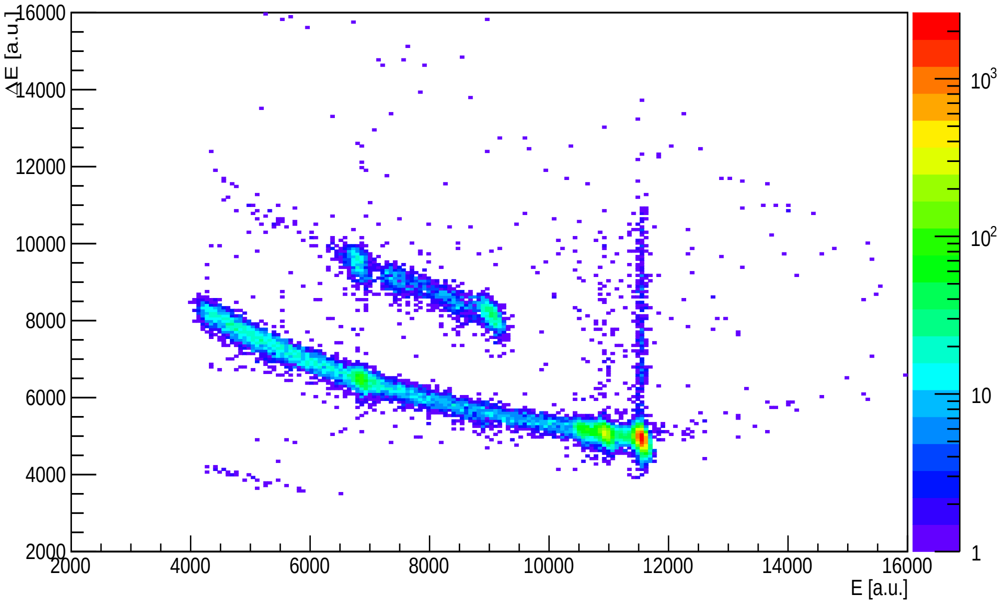

Fig. 6.9 Scatter plot of the E and ΔE signals. The lower band corresponds to the ^{7}Li scattered on the CH$_2$ target. The upper band, having a higher ΔE, is due to the ^{7}Be: the two spots at the end and at the beginning of the band are the two different kinematic solutions, while the events in the middle are the ^{7}Be* population. See Fig.6.13 to compare with the kinematics.

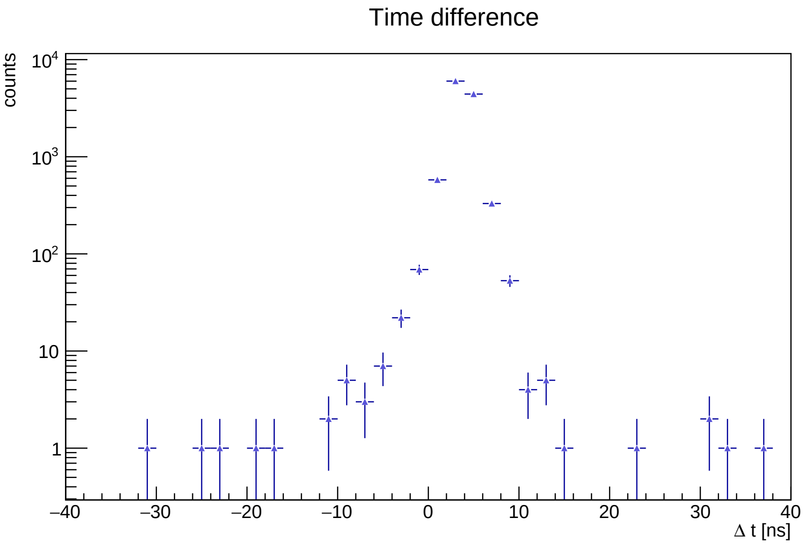

Fig. 6.10 Calibration plot to verify the timing between the pmts. ^{22}Na source placed between LSci 4 and LSci 5

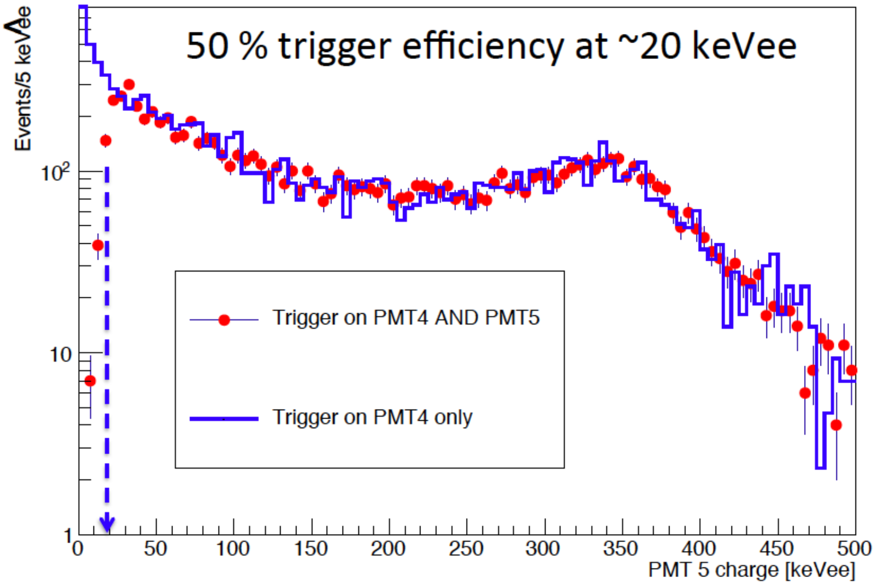

Fig. 6.11 Calibration plot to check the trigger efficiency with a ^{22}Na source placed between pmt 4 and pmt5.

two 511 keV gammas back to back, it is possible to measure the time resolution. In particular placing the source between two PMTs and plotting the time difference of the two signals (in figure 6.10 it is shown Δt for detectors 4 and 5) gives a time resolution of 1.2 ns, taking the RMS of the peak. This value is sufficient to measure the neutron time of flight. Also with the sodium source we were able to measure the trigger efficiency, that is $\sim$ 50 % at 20 keV$_{ee}$. To evaluate the pulse shape discrimination performances we used a ^{252} Cf neutrons source, placed closed to the central detectors, *i.e.* the so-called LSci0. The PSD parameter for LSci is defined as:

$$PSD_{LSci} = 1 - \frac{\int_0^{60ns} charge}{\int_0^{700ns} charge} \tag{6.4}$$

From the physical point of view, the scintillator has an opposite response to that of liquid argon, *i.e.* the neutrons produce a slower signal than β/γ events. Since the discrimination parameter (in analogy with [103]) is defined as one minus the charge fraction collected in the first 60 ns, also in the case of the LSci the upper band of the PSD plots represents the neutrons, as for the *f90*. In figure 6.12 are shown the nine scatter plots, one for each detector, of the PSD parameter with respect to the energy. The central plot is much more populated because it corresponds to LSci0, which was the closest to the source.

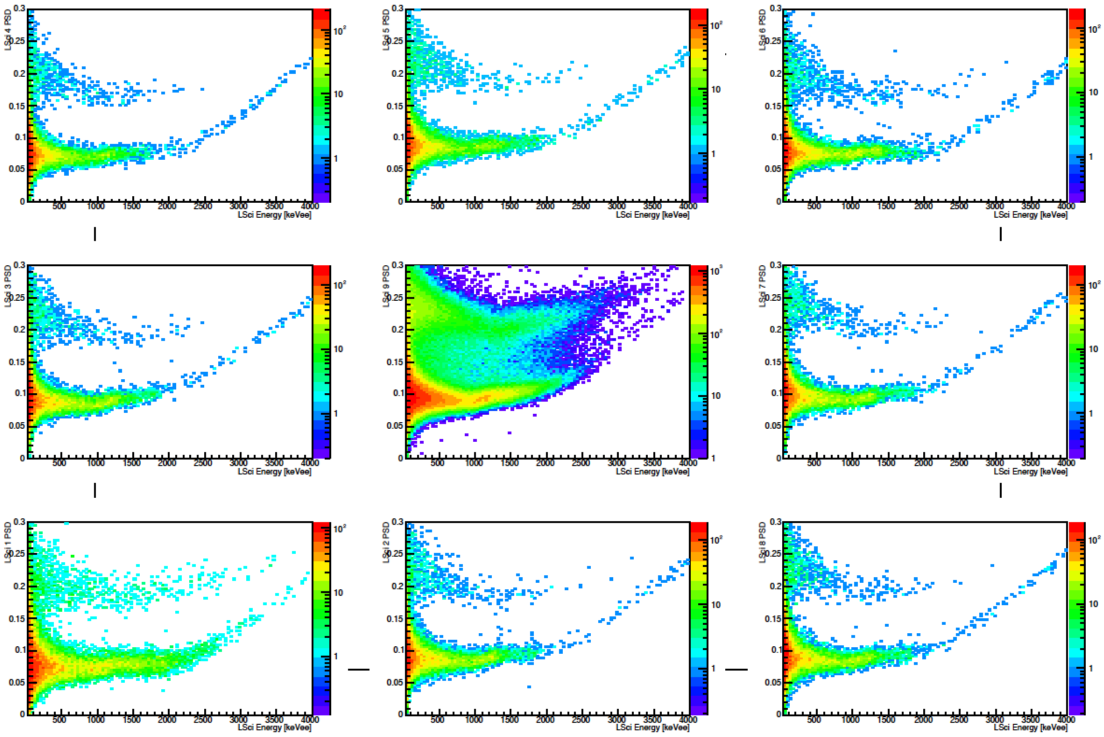

Fig. 6.12 Calibration plots for all the nine LScis obtained with a ^{252} Cf neutrons source. The PSD parameter is plotted as a function of the measured energy. The central canvas shows much more events just because the source was attached to the corresponding detector.

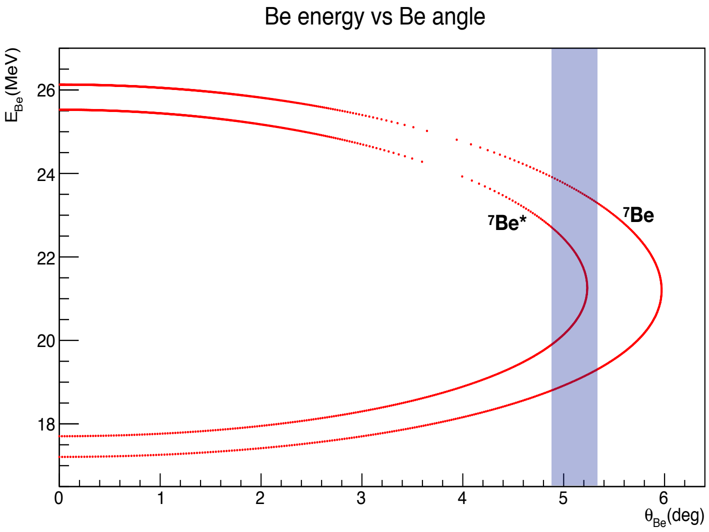

Fig. 6.13 Kinematics results for beam energy E_0 = 28 MeV, useful to select the correct ^{7}Be population in the Si-telescope events. The plot shows the ^{7}Be energy with respect to the angle of emission, the coloured band roughly highlights the angle selected in our geometry configuration.

6.3 All together

During the three campaigns performed at Laboratori Nazionali del Sud we operated the complete apparatus, looking for physical events in triple coincidence, *i.e.* seen from the Si-telescope, the TPC and the n-spectrometer. Since the system is complex and the detectors are very different with respect to each other, it has been necessary to make various measurements to optimize the conditions of data acquisition, both from a hardware point of view and from the trigger logic point of view. In particular in this section, I will focus on the measures carried out during the July run, because, as previously underlined, the June and September beam-times were dedicated to the tests and the debugging of the single parts of the setup.
As explained in section 5.7 two trigger logic configurations have been tested during July run: *"Si-telescope && any PMT"* or *"Si-telescope && TPC"*. The first configuration was considered the best choice, even if it has a higher fraction of accidentals because the single rate of the PMTs is of the order of kHz. In particular it allows to look for low energy recoils, acquired in slave mode, that would fail the TPC trigger. During these runs the trigger rate was between 0.1 and 0.7 Hz. The two Si-detectors E and ΔE were in AND with each other and then in AND with one of the eight PMTs, in a 200 ns window.

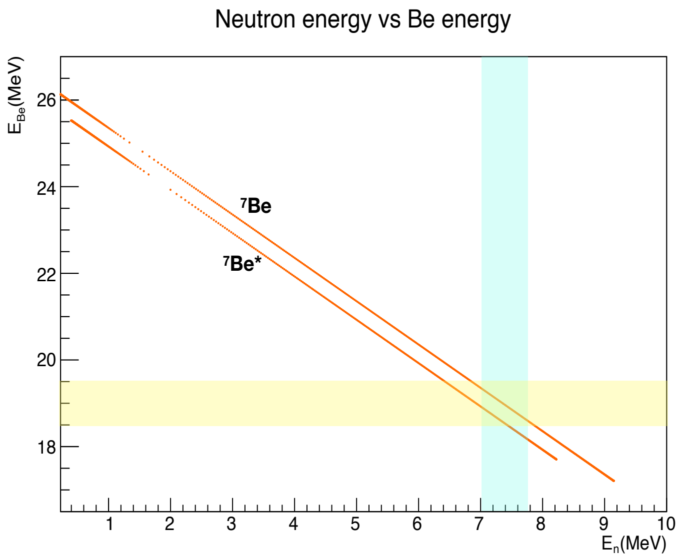

Fig. 6.14 Kinematics results for beam energy E_0 = 28 MeV, useful to select the correct ^{7}Be population in the Si-telescope events. The plot shows the neutron and ^{7}Be energies, since we want neutrons around 7.4 MeV we need to select the low energy ^{7}Be.

The preliminary results shown in the following correspond to $\sim$ 12.5 hours livetime and were collected with a beam energy E_0 = 28MeV, a varying beam current i_{beam} = (0.5$\div$ 12) nA and using the 244 μg/cm^2 CH_2 target. The TPC was operated in double phase with the standard configuration previously described (See Sec. 6.1). All these settings, as explained in detail in section 4.2.1, should give rise to nuclear recoil of $\sim$ 70 keV. In particular we are detecting reaction products at $\sim$5.15° with the telescope: as it can be seen in plot shown in figure 6.13 we select ^{7}Be with two different energies and we also detect the intermediate ^{7}Be*. These three typologies of events can be seen in the real data scatter plot, in figure 6.9. As stated before we want to tag neutrons at 22.3°, which have a 7.4 MeV energy, this additional requirement corresponds to select the low energy ^{7}Be, as highlighted in figure 6.14. This leads to perform a cut both in the E and in the ΔE signals, in order to select the correct beryllium "blob". Looking at the time difference between the Si-telescope and the neutron spectrometer signals for this kind of events, it can be clearly seen a peaked structure of physical coincidences, that emerges with respect to the flat distribution of the accidentals. In figure 6.15 you can distinguish two peaks which correspond to two different ranges of the PSD$_{LSci}$ parameter: the left peak is populated by β/γ events, with PSD$_{LSci}$ < 0.15 , vice versa the right peak corresponds to neutron events, with PSD$_{LSci}$ > 0.15. The time difference

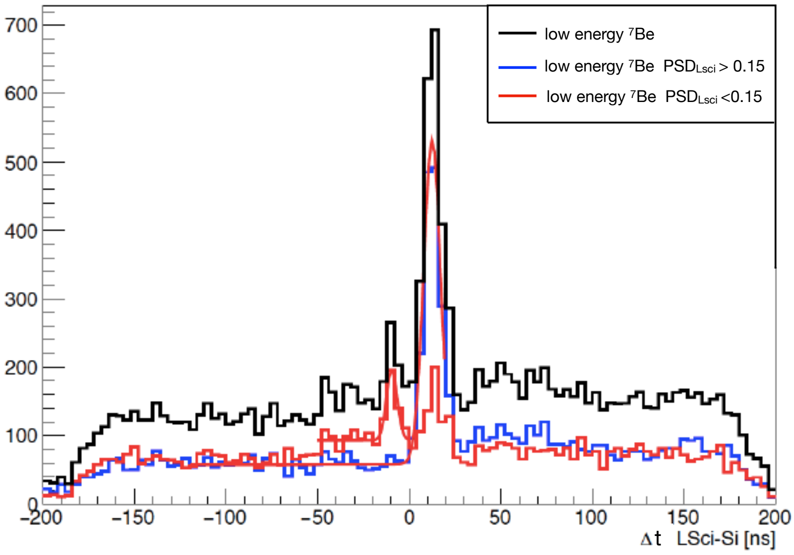

Fig. 6.15 Time difference between the signal in any of the eight LScis and the selected signal in Si-telescope. Two different peaks are present: the left one corresponds to events with $\mathrm{PSD}_{LSci} < 0.15$, vice versa the right one is mainly constituted by events with $\mathrm{PSD}_{LSci} > 0.15$

between the two peaks is about $\sim$ 20 ns that could be consistent with gammas due to the neutron inelastic scattering. In order to select good events in triple coincidence we have chosen - within the population of the neutron peak - those with at least 10 keV_{ee} of energy deposited in the scintillator. Regarding the cuts made on the TPC signals, we required that the corresponding event had two pulses and that the energy deposited was between 0 and 200 keV_{ee}. We also used the PSD_{tpc} parameter on the S1 signal, to consider only neutrons scattering in liquid argon, asking PSD_{tpc}>50. Finally we checked that the S1 was in time with respect to the Si-telescope signal.

Only 23 events, displayed in figure 6.16, survived the described selection procedure. The gaussian + exponential likelihood fit performed on the histogram gives a result consistent with the $\sim$ 70 keV expected nuclear recoil energy, assuming a nuclear quenching factor of $\sim$0.3. The main issue is that the collected data, normalized with the ^{7}Li beam current, yield to an event rate in the TPC a factor of 10 smaller than expected from Monte Carlo simulations and from the rough calculation shown in equation 4.14.

The reasons of this mismatch are currently under investigation, but we have already made some plausible hypothesis. One possible problem could be a wrong estimation of the beam current, which was measured with a Faraday cup 4 m away from the target. During the

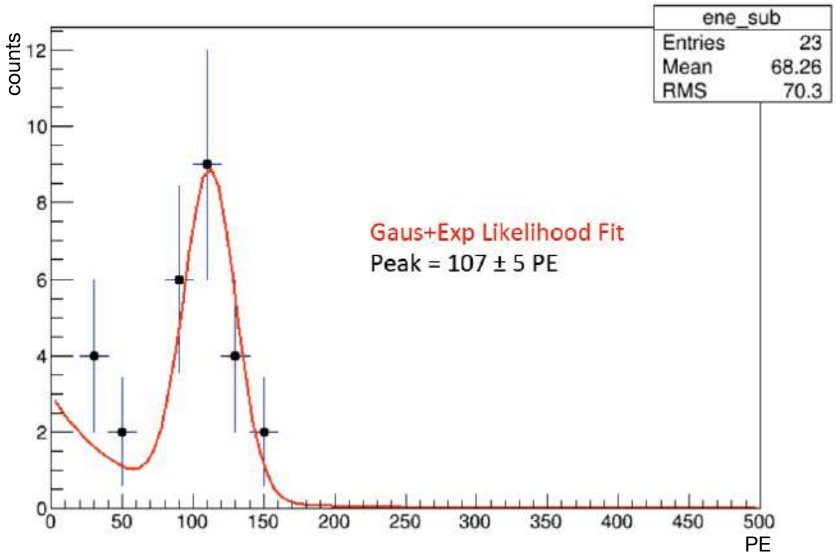

Fig. 6.16 Triple coincidence events surviving all the cuts described in the text. The peak, fitted with a gauss+exponential likelihood, is consistent with a $\sim$70 keV nuclear recoil energy, if we assume a quenching factor of $\sim$0.3 .

September beam-time, the 200 μm Si-detector was mounted at 23° with respect to the primary beam direction, in order to detect the ^{7}Li elastically-scattered by ^{12}C in the target (See Sec. 5.4). This third detector has been used to better understand the ^{7}Li beam and can be exploited to give a much more reliable on-line measurement of beam current. The second possible issue that could cause the observed lack of neutron events is a misalignment of the Si-telescope. The positioning of the detector is extremely delicate because of the strong dependency of the neutron angle with respect to the ^{7}Be one. One of the future upgrades for the ReD apparatus is going to be the insertion of a a precision handler to tune the telescope position on-line, without stopping the beam and opening the chamber.

Conclusions

The ReD project proposes the ambitious aim of measuring directional sensitivity for nuclear recoil events in the region of interest for direct search of dark matter, using a dual-phase argon Time Projection Chamber. This aspect is of crucial importance for the background rejection in the next generation detectors. They will achieve sensitivities comparable to the levels of the so-called "neutrino floor", so a directional signal could be the only signature to discriminate a dark matter event. In addition, within the extensive DarkSide program, ReD aims to measure low-energy nuclear recoils, in the range between 1.8 GeV/c^2 and 6 GeV/c^2, characterizing the ionization signal in detail. This could open the way for the exploration of a new, highly promising region of the parameter space. Finally, ReD is a tardy test bench for key DarkSide-20k technologies, in particular for signal readout using cryogenic SiPMs and for the innovative design of the TPC (See Chapter 4).

During this year a great amount of work has been done within the ReD project. We finalized the design of some of the parts, in particular the cryogenic system and the TPC. We tested for the first time our custom made SiPMs at cryogenic temperature and we also carried out the optimization of the 24 channels readout. We performed characterizations of all the components separately and finally assembled, aligned and operated the whole apparatus. I personally worked on many aspects of the ReD setup, following the commissioning phases step by step. (See Chapter 5).

At the same time as this intense commissioning phase, we have carried out several data-taking campaigns both at Università degli studi di Napoli Federico II, in Naples and at Laboratori Nazionali del Sud. in Catania. We successfully operated the TPC both in single and double phase, performing a a wide calibration campaign to study the TPC and SiPMs behaviour. We obtained a good light yield and we are able to exploit an efficient pulse shape discrimination. Further studies are needed on the S2 signal, but they are already on-going. All the different detectors have been calibrated and also operated together. We were able to acquire physical events in triple coincidence, which our ideal candidate for the directionality measurement. Some issues on the neutron rate have arisen, but we are already working to solve them, improving the alignment of the Si-telescope (See Chapter 6).

References

[1] A. H. Broeils, K. G. Begeman, and R. H. Sanders. Extended rotation curves of spiral galaxies: dark haloes and modified dynamics. *Monthly Notices of the Royal Astronomical Society*, 249(3):523–537, 04 1991.

[2] V. Belokurov, N. W. Evans, A. Moiseev, L. J. King, P. C. Hewett, M. Pettini, L. Wyrzykowski, R. G. McMahon, M. C. Smith, G. Gilmore, S. F. Sanchez, A. Udalski, S. Koposov, D. B. Zucker, and C. J. Walcher. The cosmic horseshoe: Discovery of an einstein ring around a giant luminous red galaxy. *The Astrophysical Journal*, 671(1):L9–L12, nov 2007.

[3] R. C. Reis, M. T. Reynolds, J. M. Miller, and D. J. Walton. Reflection from the strong gravity regime in a lensed quasar at redshift z = 0.658. *Nature*, 507:207–209, March 2014.

[4] P. A. R. Ade, N. Aghanim, C. Armitage-Caplan, M. Arnaud, M. Ashdown, F. Atrio-Barandela, J. Aumont, C. Baccigalupi, and A. J. Banday. Planck 2015 results. XIII. Cosmological parameters. *arXiv*, 02 2015.

[5] G. Bertone and T. M. P. Tait. A new era in the search for dark matter. *Nature*, 562(7725):51–56, 2018.

[6] Jonathan L Feng. Dark matter candidates from particle physics and methods of detection. *Annual Review of Astronomy and Astrophysics*, 48:495–545, 2010.

[7] M. Tanabashi, K. Hagiwara, K. Hikasa, et al. Review of particle physics. *Phys. Rev. D*, 98:030001, Aug 2018.

[8] A. W. Watson. *Transverse Position Reconstruction in a Liquid Argon Time Projection Chamber using Principal Component Analysis and Multi-Dimensional Fitting*. PhD thesis, Temple University, 2017.

[9] P. Agnes et al. First results from the DarkSide-50 dark matter experiment at Laboratori Nazionali del Gran Sasso. *Physics Letters B*, 743:456 – 466, 2015.

[10] P. Agnes et al. Results from the first use of low radioactivity argon in a dark matter search. *Phys. Rev. D*, 93:081101, Apr 2016.

[11] P. Agnes et al. Darkside-50 532-day dark matter search with low-radioactivity argon. *Phys. Rev. D*, 98:102006, Nov 2018.

[12] P. Agnes et al. Low-mass dark matter search with the darkside-50 experiment. *Phys. Rev. Lett.*, 121:081307, Aug 2018.

[13] M. Cadeddu, M. Lissia, P. Agnes, et al. Directional dark matter detection sensitivity of a two-phase liquid argon detector. *Journal of Cosmology and Astroparticle Physics*, 2019(01):014, 2019.

[14] H. Cao, T. Alexander, A. Aprahamian, et al. Measurement of scintillation and ionization yield and scintillation pulse shape from nuclear recoils in liquid argon. *Phys. Rev. D*, 91:092007, May 2015.

[15] E. Aprile, A. E. Bolotnikova, I. Bolozdynya A, and T. Doke. *Noble Gas Detectors*. WILEY-VCH Verlag, 1 edition, 2006.

[16] G. Bertone. *Particle Dark Matter : Observations, Models and Searches*. Cambridge University Press, 2010.

[17] V. C. Rubin and W. K. Ford, Jr. Rotation of the Andromeda Nebula from a Spectroscopic Survey of Emission Regions. *Astrophysical Journal*, 159:379, February 1970.

[18] V. C. Rubin. Dark matter in spiral galaxies. *Scientific American*, 248:96–106, June 1983.

[19] J. P. Ostriker and P. J. E. Peebles. A Numerical Study of the Stability of Flattened Galaxies: or, can Cold Galaxies Survive? *The Astrophysical Journal*, 186:467–480, December 1973.

[20] F. Zwicky. On the Masses of Nebulae and of Clusters of Nebulae. *Astrophysical Journal*, 86:217, October 1937.

[21] F. Zwicky. Republication of: The redshift of extragalactic nebulae. *General Relativity and Gravitation*, 41(1):207–224, 2009.

[22] Michael S. Turner and J. Anthony Tyson. Cosmology at the millennium. *Rev. Mod. Phys.*, 71:S145–S164, Mar 1999.

[23] Gianfranco Bertone and Dan Hooper. History of dark matter. *Rev. Mod. Phys.*, 90:045002, Oct 2018.

[24] E Pécontal, T Buchert, Ph Di Stefano, Y Copin, and K Freese. Review of observational evidence for dark matter in the universe and in upcoming searches for dark stars. *European Astronomical Society Publications Series*, 36:113–126, 2009.

[25] G. Bertone and D. Hooper. A History of Dark Matter. *arXiv*, 05 2016.

[26] Katherine Garrett and Gintaras Duda. Dark matter: A primer. *Advances in Astronomy*, 2011, 2011.

[27] M. Bartelmann and P. Schneider. Weak gravitational lensing. *Physics Reports*, 340(4–5):291 – 472, 2001.

[28] D. Clowe, M. Bradač, A. H. Gonzalez, M. Markevitch, S. W. Randall, C. Jones, and D. Zaritsky. A direct empirical proof of the existence of Dark Matter. *The Astrophysical Journal Letters*, 648(2):L109, 2006.

[29] M. Taoso, G. Bertone, and A. Masiero. Dark matter candidates: a ten-point test. *Journal of Cosmology and Astroparticle Physics*, 2008(03):022, 2008.

[30] Edward W. Kolb and Michael S. Turner. *The Early Universe*. Addison-Wesley Publishing Company, 1990.

[31] D. Boyanovsky, H.J. de Vega, and D.J. Schwarz. Phase transitions in the early and present universe. *Annual Review of Nuclear and Particle Science*, 56(1):441–500, 2006.

[32] P. A. R. Ade, N. Aghanim, C. Armitage-Caplan, M. Arnaud, M. Ashdown, F. Atrio-Barandela, J. Aumont, C. Baccigalupi, and A. J. Banday. Planck 2013 results. I. Overview of products and scientific results. *arXiv*, 03 2013.

[33] J. Silk. Cosmic black-body radiation and galaxy formation. *The Astrophysical Journal*, 151:459, February 1968.

[34] Gary Steigman. Primordial nucleosynthesis in the precision cosmology era. *Annual Review of Nuclear and Particle Science*, 57(1):463–491, 2007.

[35] WJG De Blok. The core-cusp problem. *Advances in Astronomy*, 2010, 2010.

[36] Michael Boylan-Kolchin, James S Bullock, and Manoj Kaplinghat. Too big to fail? the puzzling darkness of massive milky way subhaloes. *Monthly Notices of the Royal Astronomical Society: Letters*, 415(1):L40–L44, 2011.

[37] C. Alcock, R. A. Allsman, D. R. Alves, et al. The MACHO project: Microlensing results from 5.7 years of large magellanic cloud observations. *The Astrophysical Journal*, 542(1):281, 2000.

[38] Juan García-Bellido. Massive primordial black holes as dark matter and their detection with gravitational waves. *Journal of Physics: Conference Series*, 840(1):012032, 2017.

[39] Benjamin P Abbott, R Abbott, TD Abbott, F Acernese, K Ackley, C Adams, T Adams, P Addesso, RX Adhikari, VB Adya, et al. Gw170608: Observation of a 19 solar-mass binary black hole coalescence. *The Astrophysical Journal Letters*, 851(2):L35, 2017.

[40] K. N. Abazajian, M. A. Acero, S. K. Agarwalla, et al. Light sterile neutrinos: A white paper. *arXiv*, 04 2012.

[41] A. Boyarsky, O. Ruchayskiy, and M. Shaposhnikov. The role of sterile neutrinos in cosmology and astrophysics. *Annual Review of Nuclear and Particle Science*, 59, 11 2009.

[42] R. D. Peccei and H. R. Quinn. CP conservation in the presence of pseudoparticles. *Phys. Rev. Lett.*, 38:1440–1443, Jun 1977.

[43] Georg Raffelt. Axions in astrophysics and cosmology. *arXiv preprint hep-ph/9502358*, 1995.

[44] Lars Bergström. Dark matter evidence, particle physics candidates and detection methods. *Annalen der Physik*, 524(9-10):479–496, 2012.

[45] Jonathan L Feng and Jason Kumar. Dark-matter particles without weak-scale masses or weak interactions. *Physical review letters*, 101(23):231301, 2008.

[46] C Boehm and Pierre Fayet. Scalar dark matter candidates. *Nuclear Physics B*, 683(1-2):219–263, 2004.

[47] Tongyan Lin, Hai-Bo Yu, and Kathryn M Zurek. Symmetric and asymmetric light dark matter. *Physical Review D*, 85(6):063503, 2012.

[48] Simon Knapen, Tongyan Lin, and Kathryn M Zurek. Light dark matter: Models and constraints. *Physical Review D*, 96(11):115021, 2017.

[49] M. Milgrom. A modification of the Newtonian dynamics as a possible alternative to the hidden mass hypothesis. *Astrophysical Journal*, 270:365–370, July 1983.

[50] N. E. Mavromatos, M. Sakellariadou, and M. F. Yusaf. Can the relativistic field theory version of modified newtonian dynamics avoid dark matter on galactic scales? dynamics avoid dark matter on galactic scales? *Phys. Rev. D*, 79:081301, Apr 2009.

[51] B. P. Abbott, R. Abbott, T. D. Abbott, et al. Gw170817: Observation of gravitational waves from a binary neutron star inspiral. *Phys. Rev. Lett.*, 119:161101, Oct 2017.

[52] J.D. Lewin and P.F. Smith. Review of mathematics, numerical factors, and corrections for dark matter experiments based on elastic nuclear recoil. *Astroparticle Physics*, 6(1):87 – 112, 1996.

[53] E. Aprile, J. Aalbers, F. Agostini, et al. XENON100 dark matter results from a combination of 477 live days. *Phys. Rev. D*, 94:122001, Dec 2016.

[54] E. Aprile, J. Aalbers, F. Agostini, et al. First dark matter search results from the xenon1t experiment. *Phys. Rev. Lett.*, 119:181301, Oct 2017.

[55] D. S. Akerib, H. M. Araújo, X. Bai, et al. Improved limits on scattering of weakly interacting massive particles from reanalysis of 2013 LUX data. *Phys. Rev. Lett.*, 116:161301, Apr 2016.

[56] B Lehnert. Deap-3600 recent dark matter results. *arXiv preprint arXiv:1812.04764*, 2018.

[57] H Uchida, K Abe, K Hieda, K Hiraide, S Hirano, K Ichimura, Y Kishimoto, K Kobayashi, S Moriyama, K Nakagawa, et al. Search for inelastic wimp nucleus scattering on 129xe in data from the xmass-i experiment. *Progress of Theoretical and Experimental Physics*, 2014(6):063C01, 2014.

[58] R Bernabei, P Belli, A Di Marco, F Montecchia, A d'Angelo, A. Incicchitti, F Cappella, V Caracciolo, R Cerulli, C J Dai, H L He, H H Kuang, X H Ma, X D Sheng, R G Wang, and Z P Ye. Recent analyses on the DAMA/LIBRA-phase1 data. *Journal of Physics: Conference Series*, 718(4):042013, 2016.

[59] R Bernabei, P Belli, A Bussolotti, F Cappella, V Caracciolo, R Cerulli, CJ Dai, A d'Angelo, A Di Marco, HL He, et al. First model independent results from dama/libra-phase2. *arXiv preprint arXiv:1805.10486*, 2018.

[60] F Froborg and SABRE Collaboration. Sabre: Wimp modulation detection in the northern and southern hemisphere. *Journal of Physics: Conference Series*, 718(4):042021, 2016.

[61] J. Lindhard, V. Nielsen, M. Scharff, and P. V. Thomsen. Integral equations governing radiation effects. (notes on atomic collisions, iii). *Kgl. Danske Videnskab., Selskab. Mat. Fys. Medd.*, Vol: 33: No. 10, Jan 1963.

[62] G. Jaffé. Zur Theorie der Ionisation in Kolonnen. *Annalen der Physik*, 347(12):303–344, 1913.

[63] L. Onsager. Initial recombination of ions. *Phys. Rev.*, 54:554–557, Oct 1938.

[64] J. Thomas and D. A. Imel. Recombination of electron-ion pairs in liquid argon and liquid xenon. *Phys. Rev. A*, 36:614–616, Jul 1987.

[65] A. Hitachi, T. Takahashi, N. Funayama, K. Masuda, J. Kikuchi, and T. Doke. Effect of ionization density on the time dependence of luminescence from liquid argon and xenon. *Phys. Rev. B*, 27:5279–5285, May 1983.

[66] A.I. Bolozdynya. Two-phase emission detectors and their applications. *Nuclear Instruments and Methods in Physics Research Section A: Accelerators, Spectrometers, Detectors and Associated Equipment*, 422(1):314 – 320, 1999.

[67] I. M. Obodovskii E. M. Gushchin, A. A. Kruglov. Emission of hot electrons from liquid and solid argon and xenon. *Journal of Experimental and Theoretical Physics*, 55(5):860, 1982.

[68] P. Agnes et al. The veto system of the DarkSide-50 experiment. *Journal of Instrumentation*, 11(03):P03016, 2016.

[69] S. Westerdale. *A Study of Nuclear Recoil Backgrounds in Dark Matter Detector*. PhD thesis, Princeton University, 2016.

[70] F. Acerbi C. E. Aalseth, S. Abdelhakim et al. Report to the xlx lngs scientific committee. DocDB-3097, https://darkside-docdb.fnal.gov/cgi-bin/private/RetrieveFile?docid=3097&filename=Report-to-XLX-LNGS-SC-Oct-2018%20Sep%2025%202018.pdf&version=1, September 2018.

[71] Global Argon Dark Matter Collaboration. Future Dark Matter Searches with Low-Radioactivity Argon. European Strategy on Particle Physics, December 2018.

[72] B Abi, R Acciarri, MA Acero, M Adamowski, C Adams, D Adams, P Adamson, M Adinolfi, Z Ahmad, CH Albright, et al. The dune far detector interim design report volume 1: Physics, technology and strategies. *arXiv preprint arXiv:1807.10334*, 2018. https://arxiv.org/pdf/1807.10334.pdf.

[73] C. E. Aalseth et al. Darkside-20k: A 20 tonne two-phase lar tpc for direct dark matter detection at lngs. *The European Physical Journal Plus*, 133(3):131, 2018.

[74] Daniel Z. Freedman. Coherent Neutrino Nucleus Scattering as a Probe of the Weak Neutral Current. *Phys. Rev.*, D9:1389–1392, 1974.

[75] D. Akimov, J.B. Albert, P. An, C. Awe, P.S. Barbeau, B. Becker, V. Belov, A. Brown, et al. Observation of coherent elastic neutrino-nucleus scattering. *Science*, page eaao0990, 2017.

[76] J. Billard, E. Figueroa-Feliciano, and L. Strigari. Implication of neutrino backgrounds on the reach of next generation dark matter direct detection experiments. *Physical Review D*, 89(2):023524, 2014.

[77] F. Mayet, Anne M. Green, J.B.R. Battat, J. Billard, N. Bozorgnia, G.B. Gelmini, P. Gondolo, et al. A review of the discovery reach of directional dark matter detection. *Physics Reports*, 627:1–49, 2016.

[78] M. Cadeddu. *DarkSide-20k sensitivity, directional dark matter detection and the role of coherent elastic neutrino-nucleus scattering background*. PhD thesis, Univeristà degli Studi di Cagliari, 2017.

[79] D R Nygren. Columnar recombination: a tool for nuclear recoil directional sensitivity in a xenon-based direct detection wimp search. *Journal of Physics: Conference Series*, 460(1):012006, 2013.

[80] V. Cataudella, A. de Candia, G. De Filippis, et al. Directional modulation of electron-ion pairs recombination in liquid argon. *Journal of Instrumentation*, 12(12):P12002, 2017.

[81] ReD Collaboration. REcoil Directionality (RED) Project. Recoil directionality proposal to CSN5 2015, 2015.

[82] R Acciarri, C Adams, J Asaadi, et al. A study of electron recombination using highly ionizing particles in the argoneut liquid argon tpc. *Journal of Instrumentation*, 8(08):P08005, 2013.

[83] T. Alexander, H. O. Back, H. Cao, et al. Observation of the dependence on drift field of scintillation from nuclear recoils in liquid argon. *Phys. Rev. D*, 88:092006, Nov 2013.

[84] M. Drosg. Monoenergetic neutron production by two body reactions in the energy range from 0.0001 to 500 MeV. Tech. rep., Institute of Experimental Physics, University of Vienna, 1999.

[85] M. Drosg. The 1H(7Li,n)7Be Reaction as a Neutron Source in the MeV Range. Tech. rep., Los Alamos National Laboratory, May 1981.

[86] M. Lebois, J.N. Wilson, P. Halipré, et al. Development of a kinematically focused neutron source with the p(^{7}li,n)^{7}be inverse reaction. *Nuclear Instruments and Methods in Physics Research Section A: Accelerators, Spectrometers, Detectors and Associated Equipment*, 735:145 – 151, 2014.

[87] Horst Liskien and Arno Paulsen. Neutron production cross sections and energies for the reactions ^{7}Li(p,n)^{7}Be and ^{7}Li(p,n)^{7}Be*. *Atomic Data and Nuclear Data Tables*, 15(1):57 – 84, 1975.

[88] S.A. Elbakr, I.J. Van Heerden, W.J. McDonald, and G.C. Neilson. Measurements of neutron angular distributions from the 7li(p, n)7be reaction. *Nuclear Instruments and Methods*, 105(3):519 – 523, 1972.

[89] I. Albuquerque, M. Ave, and A. Nasir Sosa. Prospects to measure ionization yield of nuclear recoils in the 1-10 kev range with red. DocDB-3000, https://darkside-docdb.fnal.gov/cgi-bin/private/ShowDocument, November 2018.

[90] Evaluated nuclear data file (endf). https://www.nndc.bnl.gov/exfor/endf00.jsp, February 2018.

[91] F. Pino, L. Stevanato, D Cester, G. Nebbia, L. Sajo-Bohus, and G. Viesti. The light output and the detection efficiency of the liquid scintillator ej-309. *Applied Radiation and Isotopes*, 89:79 – 84, 2014.

[92] 3m™enhanced specular reflector films, 2017. https://multimedia.3m.com/mws/media/1245089O/3m-enhanced-specular-reflector-films-3m-esr-tech-data-sheet.pdf.

[93] F. Acerbi, S. Davini, A. Ferri, et al. Cryogenic characterization of fbk hd near-uv sensitive sipms. *IEEE Transactions on Electron Devices*, 64(2):521–526, Feb 2017.

[94] M. D'Incecco, C. Galbiati, G. K. Giovanetti, et al. Development of a novel single-channel, 24 cm 2, sipm-based, cryogenic photodetector. *IEEE Transactions on Nuclear Science*, 65(1):591–596, 2018.

[95] C. Savarese. *A novel light detector for DarkSide-20k*. PhD thesis, Gran Sasso Science Institute, 2017.

[96] A. Mandarano. *New generation, SiPM-based, Liquid Argon TPCs from the kg to the multi-ton scale*. PhD thesis, Gran Sasso Science Institute, 2017.

[97] M. D'Incecco, C. Galbiati, G. K. Giovanetti, et al. Development of a very low-noise cryogenic preamplifier for large-area sipm devices. *IEEE Transactions on Nuclear Science*, 65(4):1005–1011, 2018.

[98] CRYOMECH. *Cryorefrigerator Specification Sheet: PT90 with CP2850*, August 2013. Data Sheet http://www.cryomech.com/specificationsheet/PT90_ss.pdf.

[99] Sigma Technologies. *SAES Getters: PS4-MT3*, May 2012. Data Sheet http://www.saespuregas.com/Library/documents/s110-243_rev__528.pdf.

[100] Tandem, 2016. INFN-LNS https://www.lns.infn.it/it/acceleratori/tandem.html.

[101] C. Dionisi. Elementi di acceleratori di particelle. Appunti per il corso di Fisica Nucleare e Subnucleare I, A.A. 2004/2005.

[102] SCIONIX Holland. *EJ-309 liquid scintillation detector*, April 2012. Data Sheet https://scionix.nl/standard/#tab-id-3.

[103] L. Stevanato, D. Cester, G. Nebbia, and G. Viesti. Neutron detection in a high gamma-ray background with ej-301 and ej-309 liquid scintillators. *Nuclear Instruments and Methods in Physics Research Section A: Accelerators, Spectrometers, Detectors and Associated Equipment*, 690:96 – 101, 2012.

[104] V. Di Cicco. Studio e calibrazione dello spettrometro per neutroni dell'esperimento red per lo studio di scattering di neutroni su argon liquido. Tesi di Laurea Magistrale, Università degli Studi di Roma "La Sapienza", 2017.

[105] National Instruments. *INSTALLATION GUIDE NI PXIe-8840* , September 2015. User Manual http://www.ni.com/pdf/manuals/374237b.pdf.

[106] CAEN. *V1730/VX1730 and V1725/VX1725 16/8-channel 14-bit 500/250 MS/s Waveform Digitizer*, June 2016. User Manual UM2792.

[107] R. Cereseto and B. Bottino. Red alignment procedure: a step by step guide. DocDB-3163, https://darkside-docdb.fnal.gov/cgi-bin/private/ShowDocument?docid=3163, May 2018.

[108] Sergey Vinogradov, T Vinogradova, V Shubin, Dmitry Shushakov, and Konstantin Sitarsky. Probability distribution and noise factor of solid state photomultiplier signals with cross-talk and afterpulsing. pages 1496 – 1500, 12 2009.